

Numerical study of an unstable premixed laminar flame and numerical Luenberger observers

Louise da Costa Ramos

▶ **To cite this version:**

Louise da Costa Ramos. Numerical study of an unstable premixed laminar flame and numerical Luenberger observers. Automatic Control Engineering. Université Paris sciences et lettres, 2021. English. ⟨NNT : 2021UPSLM024⟩. ⟨tel-03417236⟩

HAL Id: tel-03417236

https://pastel.hal.science/tel-03417236v1

Submitted on 5 Nov 2021

HAL is a multi-disciplinary open access archive for the deposit and dissemination of scientific research documents, whether they are published or not. The documents may come from teaching and research institutions in France or abroad, or from public or private research centers.

L'archive ouverte pluridisciplinaire **HAL**, est destinée au dépôt et à la diffusion de documents scientifiques de niveau recherche, publiés ou non, émanant des établissements d'enseignement et de recherche français ou étrangers, des laboratoires publics ou privés.



HAL Authorization

PSL UNIVERSITÉ PARIS

THÈSE DE DOCTORAT
DE L'UNIVERSITÉ PSL

Préparée à MINES ParisTech

Etude numérique d'une flamme laminaire prémélangée instable et observateurs de Luenberger numériques

Numerical study of an unstable premixed laminar flame and numerical Luenberger observers

Soutenue par

Louise DA COSTA RAMOS

Le 23 septembre 2021

Ecole doctorale n° 621

Ingénierie des Systèmes, Matériaux, Mécanique, Énergétique (ISMME)

Spécialité

Mathématique et automatique

Composition du jury :

Vincent, ANDRIEU Directeur de recherche, Université de Lyon	*Président*
Mohamed, MASMOUDI Professeur, Université Paul Sabatier	*Rapporteur*
Thamy Cristina, HAYASHI Associate professor, UFRGS	*Examinateur*
Cedric, MEHL Ingénieur de recherche, IFPEn	*Examinateur*
Pierre, ROUCHON Professeur, MINES ParisTech CAS	*Directeur de thèse*
Florent, DI MEGLIO Maître assistant, MINES ParisTech CAS	*Examinateur*
Luís Fernando, FIGUEIRA DA SILVA Directeur de recherche, Institut Pprime	*Examinateur*
Valéry, MORGENTHALER Ingénieur de recherche, ANSYS France	*Examinateur*

MINES ParisTech | PSL

MINES PARISTECH

DOCTORAL THESIS

Numerical study of an unstable premixed laminar flame and numerical Luenberger observers

Author:
Louise DA COSTA RAMOS

Président:
Vincent ANDRIEU
Supervisors:
Florent DI MEGLIO
Pierre ROUCHON
Luís Fernando FIGUEIRA DA SILVA
Valéry MORGENTHALER

This project has received funding from the European Union's Horizon 2020 research and innovation programme under grant Agreement Nº 766264.

The consortium included Pontifícia Universidade Católica do Rio de Janeiro (PUC-Rio), MINES ParisTech and an industrial partner Ansys Fr.







"Il faut bien que je supporte deux ou trois chenilles si je veux connaître les papillons."

Le Petit Prince

To my parents, sisters and
brother, family,
and me.

Abstract

Louise DA COSTA RAMOS

Numerical study of an unstable premixed laminar flame and numerical Luenberger observers

La combustion et les instabilités thermo-acoustiques sont des phénomènes centraux dans le développement de turbines. Ces instabilités peuvent endommager, voire mener à la destruction de ces machines. Leur construction repose donc sur la simulation numérique dynamique (CFD), afin de prévenir et d'éviter les régimes de fonctionnement potentiellement instables. La modélisation de ces systèmes complexes est toutefois lourde en calculs, puisqu'elle nécessite la résolution d'un grand nombre d'équations nonlinéaires couplées, à paramètres distribués, et présentant une grande variété d'échelles spatiales et temporelles. Ce manuscrit est dédié à la modélisation d'une Flamme Conique Inversée (ICF) pauvre, prémélangée, laminaire et axisymétrique, à l'aide de CFD et de méthodes d'apprentissage artificiel. La flamme présente des instabilités auto-entretenues et, malgré sa relative simplicité, est porteuses d'enseignements sur la modélisation de systèmes plus complexes.

Un modèle CFD est d'abord présenté, qui servira de bases aux développements futurs. Il est constitué d'équations de conservation, couplées à un modèle de cinétique chimique méthane / air (DRM19). Ce dernier permet l'étude d'une grande variété d'échelles temporelles et spatiales de la flamme. La recherche d'un état d'équilibre du modèle couplé se révèle infructueuse, la solution stationnaire calculée numériquement présentant systématiquement des oscillations résiduelles.

Le comportement dynamique de la flamme est ensuite analysé, en particulier (1) l'impact du gradient de température sur l'adaptation de maillage, (2) le comportement dynamique autonome de la flamme, (3) sa réponse dynamique à un forçage et (4) la fonction de transfert de la flamme. Le premier point révèle un compromis entre le temps de calcul et la précision de la solution. L'analyse du comportement dynamique permet la caractérisation détaillée du comportement du front de flamme à différentes échelles.

Ensuite, un Modèle d'Ordre Réduit (ROM) est mis au point afin de permettre le calcul efficace de certains champs à l'équilibre, pour différentes valeurs du débit volumique d'entrée. Le ROM prédit les champs de vitesses axiale et radiale, ainsi que de température. Construit par interpolation entre différents points de fonctionnement, il prédit ces champs avec une précision relative inférieure à 3%.

Enfin, une méthode permettant la synthèse numérique d'observateurs pour les systèmes dynamiques non-linéaires et présentée. Elle s'appuie sur la théorie des observateurs nonlinéaires de Luenberger, qui consiste à trouver un changement de coordonnées vers un système dynamique linéaire stable. Sous de faibles hypothèses d'observabilité, l'existence de cette transformation est garantie, et celle-ci peut être calculée en utilisant des outils de régression non-linéaire. Deux approches sont présentées pour les systèmes autonomes et non-autonomes, et sont aussi discutées plusieurs stratégies d'échantillonnage de l'espace d'état.

Combustion and thermo-acoustic instabilities are major topics of interest in the development of combustion engines since such instabilities can cause damage or even failure of these machines. For this reason, the design of combustion engines

highly relies on computational fluid dynamic models (CFD). However, the modeling of such complex systems involves a high computational burden since it involves computing the solution to a large number of nonlinear coupled partial differential equations over different time and spatial scales. This manuscript is devoted to modeling a laminar, axisymmetric, lean premixed inverted conical flame, anchored at a central bluff-body, in an unconfined burner configuration, with CFD and machine learning (ML). This flame feature self-excited instabilities and, despite its relatively simple configuration, gives insight into more complex flame configurations, such as in aeronautical engines combustion chambers.

First, a CFD model used as the basis for further developments is described, consisting of the species mass, momentum, and energy transport equations, coupled with a skeletal methane/air chemical kinetic mechanism. This kinetic mechanism enables to capture of a plethora of time and length scales linked to the flame. This model is first used to investigate the characteristics of the steady-state of the studied flame, showing that it does not present a static convergence behavior and, rather, oscillates over a pseudo-steady state point.

Second, the dynamic behavior of the flame is analyzed, characterizing the following points: (1) the impact of the temperature gradient threshold for the mesh adaption process, (2) the flame natural dynamic response, (3) the forced flame dynamic response, and (4) the flame transfer function. The analysis of the impact of the adaption threshold on the model reveals a trade-off between the model accuracy and computational burden, which can be adjusted by changing the temperature gradient threshold. The flame response analysis gives a detailed characterization of the flame front behavior in its different scales, both in time and space.

Third, a reduced-order model is designed to efficiently compute the averaged flame properties field at steady-state. The volume flow rate of the combustible mixture is the variable parameter, and the fields of the axial and radial velocity components and the temperature fields are the predicted outputs. The results present great agreement with the original CFD results, presenting an average relative error smaller than 3 %. The extension of this work to other combustion processes is a perspective of this work, willing to model all the flame properties available from the CFD models.

Last, a method to numerically design observers for nonlinear systems is presented. The method relies on the theory of nonlinear Luenberger observers, which maps the nonlinear dynamics of a system of interest to a linear stable system, for which observer design is easy. Relying on mild assumptions of observability and results guaranteeing the existence of such mappings, a methodology is proposed to approximate them by performing a nonlinear regression on sample data that is simply generated by solving the system and observer dynamics. Two approaches are detailed for autonomous and excited systems, where the first one is based on general hypotheses, whereas the second relies on stronger assumptions. Validation is developed over different systems, for which several issues related to state-space sampling are discussed.

Acknowledgements

I would like to extend my gratitude to my advisors Florent Di Meglio, Luís Fernando Figueira da Silva and Valéry Morgenthaler, for their support and teachings through these three years of work. I am greatly indebted to the profound belief and the confidence they entrusted on me and the freedom I had to develop this work. Having three supervisors seem frightening at first sight, but this collaboration turned out to be amazingly pleasant and fluid, and each of them had an important role in the development of this work. The learning process was a challenge and cannot be overstated, and I deeply appreciate their patience and consideration for it. This work and manuscript would not have been possible without their guidance and the uplifting conversations and the ethic of working with an intellectual rigor that they have instilled in me. My working experience has been extremely pleasureful and I will dearly miss it being the routine. I would not miss a chance of collaborating with each of them again.

I would like to express my gratitude to the Ansys Digital Twin group and to Ansys France itself, which received and accommodate me with kindness and support for my PhD. The work environment was comfortable and flexible, and the daily life was simply amazing, in addition to my colleges there, which also helped me to be at ease and comfortable during this time. I would also like to give a special thanks to Michel, Juliette, Romain, Sophie, Clementine, Karim, Malek and Felipe for the long conversations and coffee breaks. My sincere thanks to Jeroen and Christelle, which gave me a remarkable support on the development of this work and with whom I had numerous work discussions and collaborative ideas. I look forward to continue the work we have started together.

I am also grateful to being par of the Centre Automatique et Systèmes (CAS) of MINES ParisTech. My sincere thanks to all the members of CAS. My special thanks to Pauline Bernard, Mona and Nils which I had the pleasure of collaborating and I look forward to give continuity to it in the academia and the entrepreneurial world respectively. Also, my kind regards and thanks all of to my European MAGISTER colleagues.

To my friends and family, that gave me the support through out all of this three years work, my deepest gratitude, and I'd also like to say that this achievement is not just mine, but ours. I'd like to say special thanks do Paul, which was at my side at all long and late nights of work, and to my friends Janaina, Sueny, Karla, Anne Caroline and Sarah, which I had the honor to meet during my PhD, and which were by my side giving me support and being my family this past three years.

I would also like to express my deepest appreciation to the defense committee that comprised of Vincent Andrieu, Mohamed Masmoudi, Thamy Cristina Hayachi and Cedric Mehl. I am grateful for all the enthusiastic discussions whit the committee, which helped to make the best of this work.

Mes plus sincères remerciements à tous ceux qui ont fait partie de ce parcours.

Louise da Costa Ramos
Paris, France.

Contents

Abstract **vii**

Acknowledgements **ix**

I Computational Fluid Dynamic Modeling **7**

1 Inverted Conical Flame **9**
1.1 Introduction . . . 9
1.2 1D Flame Model . . . 11
1.2.1 Skeletal chemical kinetic flame model . . . 11
1.2.2 Preliminary model: definition of flame scales . . . 12
1.3 Computational Fluid Dynamics Model . . . 13
1.3.1 Governing equations . . . 14
1.3.2 Equations of state and constitutive relations . . . 15
1.3.3 Domain, boundary conditions and mesh . . . 15
1.4 Numerical Methodology . . . 17
1.4.1 Transient finite volume method . . . 17
1.4.2 Solver methodology . . . 19
1.4.3 Steady-state model . . . 21
1.4.4 Mesh adaption methodology . . . 21
1.4.5 Numerical ignition . . . 22
1.5 Outputs of interest . . . 23
1.5.1 Properties measurement probes . . . 24
1.5.2 Flame surface area . . . 24
1.6 Inverted Conical Flame Steady-State Model . . . 25
1.6.1 Laminar Flame Structure . . . 26
1.6.2 Averaged Laminar Flame Structure . . . 29
1.7 Synthesis . . . 30

2 Unsteady Inverted Conical Flame and Thermo-acoustic Coupling **31**
2.1 Introduction . . . 31
2.2 Mesh Adaption Influence . . . 33
2.3 Flame dynamics . . . 37
2.3.1 Flame Transfer Function (FTF) . . . 37
2.3.2 Computation of the Flame Transfer Function . . . 37
2.4 Results and Discussion . . . 39
2.4.1 Unforced ICF . . . 39
2.4.2 Forced flame analysis . . . 44
2.5 Synthesis . . . 51

II Machine Learning **55**

3 Steady Reduced Order Model **57**
3.1 Introduction . . . 57
3.2 Numerical Methodology . . . 58
3.2.1 Reduced Order Model . . . 58
3.2.2 ICF training data . . . 60
3.3 Results and Discussion . . . 60
3.3.1 Learning and Validation dataset generation . . . 60
3.3.2 ROM Analysis . . . 61
3.4 Synthesis . . . 65

4 Luenberger Observers **67**
4.1 Introduction . . . 67
4.1.1 Context . . . 68
4.1.2 Problem Statement . . . 69
4.2 Methodology . . . 70
4.2.1 Learning Procedure: Autonomous Systems . . . 70
4.2.2 Learning Procedure: system with an excitation . . . 72
4.3 Neural Networks . . . 74
4.3.1 Proposed Neural Network Methodology . . . 75
4.4 Numerical simulation . . . 77
4.4.1 Autonomous System . . . 77
4.4.2 Non-autonomous System: Van der Pol . . . 81
4.4.3 Non-autonomous System: Adding an input to (4.20) . . . 82
4.4.4 Non-autonomous System: laminar flames . . . 84
4.5 Synthesis . . . 89

5 Conclusions and Perspectives **91**

A ICF Flame Front Complete Response Cycles **93**

B FTF Gain and Phase for the Mesh Adaption Different Refinement Thresholds **103**

Bibliography **105**

List of Figures

1.1 Representative view of OH mass fraction for the unsteady inverted conical flame. Mean velocity of $v_d = 2.05\ m/s$ and metane/air equivalence ratio $\phi = 0.92$, $T_\infty = 300\ K$ and $p = 1\ atm$ [36]. 10
1.2 Simplified representative scheme of a detailed kinetic model for methane combustion [45]. 11
1.3 Fields of mass fraction of CH_2 and OH, and temperature (K) obtained for the 1D freely propagating laminar premixed methane/air flame, with equivalence ratio of $\phi = 0.92$, $T_\infty = 300\ K$ and $p = 1\ atm$ [36]. . . 13
1.4 Zoom on the fields of mass fraction of CH_2 and OH, and temperature (K) obtained for the 1D freely propagating laminar premixed methane/air flame, with equivalence ratio of $\phi = 0.92$, $T_\infty = 300\ K$ and $p = 1\ atm$ [36]. 13
1.5 Representation of the axisymetric computational domain with corresponding boundary conditions and dimensions labels. The boundary conditions setups and measures are given at Tabs. 1.1 and 1.2 respectively. 16
1.6 Axisymmetric computational domain blocks division. M_1: is the block where the flame is encountered; M_2, M_3: are the blocks where the air and burned gases flow. 18
1.7 Flow chart representation for Fluent solution process. 20
1.8 Representation of the mesh adaptation due to temperature gradient (obtained using Fluent). Left: base mesh with a size of 100 μm; center: mesh already adapted after the flame is developed; right: zoom on the adapted mesh. 22
1.9 Representation of the computation initialization patches. 23
1.10 Data extraction points in the flame region and outline of fluctuation flame surface. 24
1.11 Comparison of the instantaneous flame front identified with the CH_2 mass fraction (left) and with the binary field ι (right). 26
1.12 Structure of the laminar premixed inverted conical flame, with a volume flow rate of $\dot{\forall}_d = 180.3\ cm^3/s$ and a methane/air equivalence ratio of $\phi = 0.92$ [36]. 27
1.13 Comparison of the flame front structure between Fluent and its average: fields of velocity components and temperature, for two different fuel/air mixture flow rates. Fluent steady field on the left and ensemble average on the right side, for $\dot{\forall}_3 = 180\ cm^3/s$. [36] 29
1.14 Experimental steady inverted conical flame, with equivalent ratio $\phi = 0.92$ and nominal volume flow rate $\dot{\forall}_d = 180\ cm^3/s$ [9]. 30

2.1 Resonant coupling mechanisms through which flow velocity oscillations lead to combustion heat release oscillations [71]. 33

2.2 Mesh adaption region for different refinement temperature gradient threshold values. . . . 34
2.3 Instantaneous of the flame front for different mesh refinement temperature gradient threshold values. . . . 35
2.4 Flame surface area fluctuations results for each of the cases presented in Table 2.1, i.e., different mesh refinement thresholds. . . . 36
2.5 Spectrum of the heat release response for a mono-frequent excitation at $f = 100\ Hz$. . . . 38
2.6 Unforced flame front position at different equally spaced (by 100 μs) instants in time. . . . 40
2.7 Unforced ICF surface area response history and frequency behavior. . . . 41
2.8 Spectogram of the ICF surface area fluctuation, for the final 1 s of simulation. . . . 42
2.9 Complete pressure history frequency analysis for the data extracted at point O (—), presented in Table 1.3. . . . 42
2.10 Unforced ICF pressure history frequency analysis and signal reconstruction. The depicted results are relative to the data extracted at point O (—), presented in Table 1.3. . . . 43
2.11 Unforced ICF temporal fluctuations obtained at 4 different positions, points G (—), I (▭▭), M (⊙—⊙) and O (- · -), given in Table 1.3. . . . 44
2.12 Flame front surface at different, equally spaced instants (by 2.5 ms), for different forcing frequencies. Each row presents a different forcing frequency, in the following order: 50, 75, 100, 125, 150, 172 and 200 Hz, corresponding to Strouhal numbers of 0.48, 0.71, 0.95, 1.19, 1.43, 1.63 and 1.9. . . . 46
2.13 Flame surface area fluctuation due to four different incoming forcing frequencies, underscoring the flame different responses. . . . 48
2.14 Harmonic response of the flame surface area fluctuation for different forcing frequencies (f). . . . 49
2.15 Dependency of the RMS of the inlet velocity fluctuation, RMS and mean of the flame surface area fluctuation with the forcing frequency (f). . . . 50
2.16 Gain and phase difference between velocity and flame surface area fluctuation of the ICF as a function of the incoming forcing frequency. The results for experiment [10] and CFD are compared. Also, the values for the gain and phase at 100 Hz for different mesh adaption temperature gradients are given for the following gradients; 10 K/m (▫), 25 K/m (○), 50 K/m (◁) and 100 K/m (△). . . . 51

3.1 Flowchart representing the learning methodology for steady ROMs. . . . 59
3.2 ICF training samples for the fields of velocity components and temperature, for three different fuel/air mixture flow rates. The colormap is defined as black an light blue at minimum values, respectively, i.e., $v_y \in [-1, 6]\ m/s$, $v_r \in [-2, 3]\ m/s$ and $T \in [298, 2200]\ K$. . . . 61
3.3 Comparison between the Fluent averaged results with ROM prediction for the averaged steady ICF, for a fuel inlet volume flow rate of $\dot{\forall}_5 = 198.4\ cm^3/s$. The colormap is defined as black an light blue at minimum values, respectively, i.e., $v_y \in [-1, 6]\ m/s$, $v_r \in [-2, 3]\ m/s$ and $T \in [298, 2200]\ K$. . . . 63

3.4 Comparison of the contour of the flame temperature for the ensemble averaged steady Fluent result (red) and the StaticROM (yellow) prediction for the ICF case 5, with a volume flow rate of $\dot{\forall}_5 = 198.4$ cm^3/s. [36] 64

4.1 Neural network simplified flow chart. 74
4.2 Neuron representation. 74
4.3 Impact of the size of the compact: Comparison of the autonomous system (Equation (4.20)) solutions for an observer defined in $\mathbb{R}^3$, with a different range for the Gaussian distributed initial conditions. The prediction test is over 100 equally distributed initial condition $(x_{1,0}, x_{2,0}) \in [-10, 10]$. 79
4.4 Transformation $\mathcal{T}$. 80
4.5 Solution for the autonomous system (eq. (4.20)) with an observer z defined in $\mathbb{R}^3$, with regular partition used for choosing the 20 initial conditions $(x_{1,0}, x_{2,0}) \in (-10, 10)$. 81
4.6 Solution for the autonomous system (Equation (4.20)) with an observer z defined in $\mathbb{R}^3$, with regular partition used for choosing the 100 initial conditions $(x_{1,0}, x_{2,0}) \in (-10, 10)$. 82
4.7 Evolution of the true and estimated states over time of the autonomous system (Equation (4.20)) for an observer defined in $\mathbb{R}^3$, with different eigenvalues. 83
4.8 Evolution of the true and predicted states, showing the impact of the number of states of the observer on the performance of the design for the Van der Pol oscillator. 84
4.9 Training trajectories and estimation error for the artificially excited nonlinear oscillator. 84
4.10 Comparison and error of the prediction for trajectory with initial condition $(x_1, x_2) = (1, 0)$ and input $u(t) = 0$. 85
4.11 Kornilov flame training samples [106]. 86
4.12 Dynamic ROM scheme. 87
4.13 Comparison of the prediction for the trajectories with $u(t) = 0.4 \cdot sin(2\pi 100t) + 0.8 \cdot sin(2\pi 150t)$. 88
4.14 Comparison of the prediction for the trajectories with a linear chirp forcing. 89

A.1 Forcing of 50 Hz with adaptation 50 K/m. 94
A.2 Forcing of 75 Hz with adaptation 50 K/m. 95
A.3 Forcing of 100 Hz with adaptation 50 K/m. 96
A.4 Forcing of 125 Hz with adaptation 50 K/m. 97
A.5 Forcing of 150 Hz with adaptation 50 K/m. 98
A.6 Forcing of 172 Hz with adaptation 50 K/m. 99
A.7 Forcing of 200 Hz with adaptation 50 K/m. 100
A.8 Forcing of 250 Hz with adaptation 50 K/m. 101

B.1 RMS values of the flame surface area fluctuation $[m^2]$ and the corresponding FDF gain as a function of the temperature gradient refinement threshold. 104

List of Tables

1.1 Boundary conditions of the CFD model. 17
1.2 Dimensions L_i, characteristic of the CFD domain, in $[mm]$. 17
1.3 Point name and corresponding (z^*, r^*) non dimensional coordinates of each point shown on Figure 1.10. These are no dimensional axial and radial coordinates, such that $z^* = z/D$ and $r^* = r/D$, where $D_b = 22$ mm is the $mixture - inlet$ tube outlet diameter. 25

2.1 Mesh adaption temperature gradients thresholds influence. 34

3.1 Fuel/air mixture parameters setup for the Fluent modeling of the Inverted Conical Flame. The values given represent the mean value at the burner outlet. 60
3.2 RMS errors of the SVD and ROM Euclidean norm errors of the learning using 4 modes, for each of the developed models. 64

List of Abbreviations

CFD	**C**omputational **F**luid **D**ynamics
RANS	**R**eynolds-**A**veraged **N**avier **S**tokes
ML	**M**achine **L**earning
MLP	**M**ulti-**L**ayer **P**erceptron
kNN	**k**-**N**earest **N**eighbors
ROM	**R**educed **O**rder **M**odels
LSTM	**L**ong **S**hort-**T**erm **M**emory
ICF	**I**nverted **C**onical **F**lames
GRI	**G**as **R**esearch **I**nstitute
DRM	**D**eveloped **R**educed **M**echanisms
URF	**U**nder **R**elaxation **F**actor
1D	**1** **D**imension
2D	**2** **D**imensional
ISAT	**I**n-**S**itu **A**daptive **T**abulation
TCI	**T**urbulent **C**hemestry **I**nteraction
PRESTO!	**PRE**ssure **ST**aggering **O**ption
FTF	**F**lame **T**ransfer **F**unction
GARS	**G**enetic **A**ggregation **R**esponse **S**urface
FDF	**F**lame **D**iscribing **F**unction
LES	**L**arge **E**ddy **S**imulation
FFT	**F**ast **F**ourier **T**ransform
DFT	**D**iscrete **F**ourier **T**ransform
CFL	**C**ourant **F**reidrichs **L**ewy
NARX	**N**onlinear **A**uto**R**egressive E**X**ogenous models
POD	**P**roper **O**rder **D**ecomposition
SVD	**S**ingular **V**alue **D**ecomposition
RMS	**R**oot-**M**ean-**S**quare deviation
ODE	**O**rdinary **D**ifferential **E**quation
PDE	**P**artial **D**ifferential **E**quation
NN	**N**eural **N**etwork
ESR	**E**arly **S**tage **R**esearcher

List of Symbols

Diameter of burner outlet	D_b	mm
Diameter of central cylindrical rod	d	mm
Equivalence Ratio	ϕ	[-]
Ambient Temperature	T_∞	K
Pressure	p	atm
Laminar flame front speed	S_L	$\mathrm{cm\,s^{-1}}$
Flame adiabatic temperature	T_{ad}	K
Froude number	Fr	[-]
Gravity acceleration	g	$\mathrm{m\,s^{-2}}$
Flame length	L	m
Mixture density	ρ	$\mathrm{kg\,m^{-3}}$
Flow velocity vector	$\vec{v}$	$\mathrm{m\,s^{-1}}$
Mass diffusion coefficient of the species i	D_i	$\mathrm{m^2\,s^{-1}}$
Time	t	s
Mass fraction of the species i	Y_i	[-]
Rate of reaction i	$\dot{\omega}_i$	$\mathrm{kg\,m^{-3}\,s^{-1}}$
Stoichiometric coefficients of species $\mathcal{M}_j$ in reaction i	$a_{j,i}$	[-]
Molar concentration of species $\mathcal{M}_j$	$[X_j]$	$\mathrm{mol\,L^{-1}}$
Arrhenius rate constant of species i	K_i	[-]
Frequency factor of species i	$A_{0,i}$	[-]
Temperature exponent of species i	β_i	[-]
Activation energy of species i	$E_{a,i}$	$\mathrm{cal\,mol^{-1}}$
Universal gas constant	R	$\mathrm{cal/mol - /K}$
Diffusive mass flux of species i	j_i	$\mathrm{mol\,cm^{-1}\,s^{-1}}$
Viscous stress tensor	τ	$\mathrm{kg\,m^{-1}\,s^{-2}}$
Dynamic viscosity	μ	Pa s
Volumetric viscosity	η	Pa s
Identity tensor	I	[-]
Thermal diffusion coefficient	α	[-]
Enthalpy	h	J
Enthalpy of the species i	h_i	J
Molecular mass of the species i	M_i	$\mathrm{g\,mol^{-1}}$
Specific heat at constant pressure of the mixture	C_p	$\mathrm{J\,kg^{-1}\,K^{-1}}$
Standard temperature where the enthalpy is define	T_{std}	K
Enthalpy of formation at the standard state of species i	h_i^0	J
Time step	Δt	s
Scalar flow property	φ	[-]
Surface area vector	$\vec{A}$	$\mathrm{m^2}$
Diffusion coefficient of the variable	Γ_φ	[-]
Source of φ per unit of volume	S_φ	[-]
Face index	fc	[-]
Number of faces enclosing a cell	N_{faces}	[-]

Cell volume	V	m
Temperature gradient refinement threshold	ΔT_{refine}	$\mathrm{K\,m^{-1}}$
Temperature gradient coarsening threshold	ΔT_{coarse}	$\mathrm{K\,m^{-1}}$
Mesh characteristic size	Δx	m
Axial and radial coordinates	(z, r)	m
CH_2 mass fraction	Y_{CH_2}	[-]
Maximum CH_2 mass fraction	$Y_{CH_2}^{max}$	[-]
Machine zero value	ϵ	[-]
Volume flow rate	$\dot{\forall}$	$\mathrm{cm\,s^{-1}}$
Nominal mixture velocity	v_d	$\mathrm{m\,s^{-1}}$
Nominal volume flow rate	$\dot{\forall}_d$	$\mathrm{cm\,s^{-1}}$
Mixture subscript	mix	[-]
Air subscript	air	[-]
Root-mean-squared subscript	rms	[-]
Frequency	f	Hz
Velocity fluctuation	v'	$\mathrm{m\,s^{-1}}$
Velocity fluctuation amplitude	v_a	$\mathrm{m\,s^{-1}}$
Flame Transfer Function	$\mathcal{F}$	[-]
Heat release rate	$\dot{Q}$	J
Angular frequency	ω	$\mathrm{rad\,s^{-1}}$
Flame surface area	A	m
FTF phase	γ	[-]
FTF gain	G	[-]
Strouhal number	S_{td}	[-]
System state	x	[-]
System measured output	y	[-]
Observer state	z	[-]
Input of interest	u	[-]
Compact set of interest	$\mathcal{X}$	[-]
Open bounded set	$\mathcal{O}$	[-]
Dimension of parameter j	d_j	[-]
Hurwitz matriz	D	[-]
Hurwitz matriz eigenvalues	$(\lambda_1, ..., \lambda_{d_z})$	[-]
Transpose subscript	T	[-]
Observer transformation	$\mathcal{T}$	[-]
Observer pseudo-inverse transformation	$\mathcal{T}^*$	[-]
Initial condition subscript	0	[-]
Minimum value subscript	min	[-]
Set of zero measure of the observer	S	[-]
NN weighs	Θ	[-]
NN number of layers	N_L	[-]
NN layer subscript	k	[-]
NN number of neurons of layer k	l_k	[-]
NN training output set	Y	[-]
Error of layer k	$\delta^{(k)}$	[-]
NN number of training data	m	[-]
NN bias factor	a_0	[-]
Simulation end time	t_f	s

Introduction

Combustion is a chemical reaction process present in almost all social sectors, throughout the world, independent of the socioeconomic situation of the country. This process has a major part in the worldwide economy, since combustion is still the main source of energy [1], being responsible for more than 80% of the energy primary conversion. Hydrocarbon combustion involves a series of chemical reactions, where carbon is oxidized to carbon dioxide, and hydrogen is oxidized to water. This process is present in several practical systems, for example, domestic stoves, car engines or aircraft gas turbines and as heating source for buildings. Therefore, combustion processes are associated to a high impact on the industrial sectors of power generation and transport. Furthermore, glass, mining, chemical and steel mill industries are the main users of the combustion of biogas and hydrocarbons in their manufacturing processes.

However, the combustion process has an associated harm, which is the environmental pollution. Some of the substances produced by the combustion can cause harm to the human and environment. For instance, the carbon monoxide (CO) is highly toxic for animals and humans, and soot is one of the major air pollutants [1]. Moreover, the production of the carbon dioxide (CO_2) by combustion process contributes to global warming, being responsible for the observed increase of the levels of the substance in the atmosphere.

In the context of this thesis, the combustion process involved in aeronautical engines combustion chambers is the major topic of interest. These engines are essential for the aviation industry, however, there are several combustion and reactive effects that decrease their efficiency. The soot formation inside of engines, for example, creates deposits within the combustor, leading to a decreased efficiency or even harming the integrity [2]. In these engines, the combustion and acoustic coupling is a major issue since the interactions of the reactions with flow perturbations lead to thermo-acoustic instabilities that may damage the engines, causing even failures.

Moreover, in the past years, the emission regulations for these engines have been steadily tightened, making it even more difficult to avoid thermo-acoustic instabilities. Thereby, the design of combustion engines heavily relies on computational models, enabling the optimization of combustors and forecasting instabilities. However, research dedicated to understanding thermo-acoustic instabilities over the last decades [3]–[6] have shown that the high sensitivity of this phenomenon with respect to several poorly known combustion parameters hamper their prediction and control.

The high uncertainty involved in predicting and controlling thermo-acoustics is addressed by the MAGISTER ITN Project, applying methods originally developed in computer sciences to the multi-disciplinary engineering problem. The project is composed of several early-stage researchers (ESR's) working at the intersection of combustion engineering and Machine Learning. This thesis has been conducted as part of this project.

This manuscript focuses on the modeling, characterization and control of combustion instabilities, through computational approaches. More precisely, in a first

part, an unconfined laminar lean premixed flame is modeled and simulated, enabling characterization of its combustion instabilities. In a second part, a Reduced Order Model (ROM) of a few steady-state of its properties is constructed. Finally a novel method for designing state observers for nonlinear dynamical systems is proposed and applied to a dynamic ROM of a simpler flame.

Lean premixed flames are vastly studied because of their unstable behavior, which typifies those of complex combustion chambers. For instance, the dynamical behavior of laminar conical premixed flames due to incoming perturbations has been characterized with a transfer function, relating the incoming velocity excitation and heat release fluctuations [7]. A comparison between the transfer function obtained with experimental data and a first order analytical model shows good agreement for low frequency only. The response of a conical laminar rich premixed flame has been also characterized by a flame transfer function, experimentally and on a flame model [8]. The flame dynamics are based on the level set approach, which cannot account for the complexity of the behavior, but highlight the main features when the model takes in account the phase shift between the mean flow and the flame front [8]. This manuscript studies a laminar premixed Inverted Conical Flames (ICF). It is not only susceptible to thermo-acoustic instabilities, but also presents a self-sustained unstable behavior. Experiments on such flames, anchored on a bluff-body, have shown that the flame is self-excited under certain conditions. Studies also shown that there is a strong influence of the shear layer dynamics on the flame response [9], [10]. Moreover, the flame instabilities are mainly seen at the vicinity of tip of the ICF, such that this flame region is of major importance for the heat release and transfer function computations [9], [10]. This is an important point, which justifies the use of a detailed chemical model in our study, as detailed later.

There are few attempts to construct detailed computational models of the ICF in the literature. Low-order models are proposed in [11] and unsteady 2D numerical simulations with a skeletal C1 chemical mechanism are derived in [12]. The modeling the ICF relying on the widespread G-equation framework, combined with a convective velocity model, has shown that the heat-release is proportional to the flame tip movement [11]. However, the flame response leads to static gain values exceeding the expected unity [11]. Besides, the unsteady 2D model with detailed chemistry and species transport, with coupled heat transfer to the bluff-body has been used to analyze the dynamics of the flame leading edge in an ICF [12]. The study applies a Cartesian structured grid, with the coarsest level of 196 µm and one additional levels of grid refinement [12]. Such choice relies on the analysis in which it is shown that a fine grid resolution of 100 µm can capture the lean premixed flame flow properties and the major species behavior, however, the minor species are not perfectly captured [12], [13]. Results have shown that the motion is mainly due to the advection of appropriate ignition conditions because of the excitement of the wake recirculating flow. The impact of varying the bluff-body material, equivalence ratio and inlet velocity is studied [12]. In this work, we propose a detailed model of the flame with a focus on quantitatively reproducing its self-sustained instabilities.

Combustion instabilities, which are a major topic of interest on the design of aircraft combustors, are thus present in several reactive systems. However, different mechaniscms may lead to this undesirable behavior. Studies have shown that annular combustors tend to present significant instabilities linked to the natural acoustic modes of the system, usually coupling with azimuthal modes, with a spinning or a

standing structure [14], [15]. Moreover, studies carried on laminar premixed flames have shown that, when a tube is coupled with a flame, the dynamic behavior of the flame is governed by the natural resonance of the tube [4].

On the other hand, fewer studies have been developed on self-excited instabilities. The study of the behavior of self-excited round jet diffusion flames has shown that hydrodynamic instabilities are caused by the action of buoyancy [16]. When the flame is under forcing, is has been shown that the absolute self-sustained frequency remains robust, even under high frequency forcing. However, to the best of the authors knowledge, no studies regarding self-excited laminar premixed flames (i.e. in the absence of acoustic coupling) and their response due to external excitation were yet developed.

Machine learning (ML) methods have also been recently applied to the modeling and analysis of combustion systems. Surveys on the use of Machine Learning methods for combustion modeling and analysis can be found in [17], [18]. The literature focuses on both qualitative and quantitative and applications. Contributions mainly rely on Neural networks [19] to classify stable and unstable regimes [20] or assess combustion performance [21] and emission intensity [19]. On other hand, there is an abundant literature on Reduced Order Models (ROM) focusing on modeling the whole combustion process or only its dominant features. More specifically, Galerking methods [22], [23] and physics-based reduction [24] are used to analytically decrease the complexity of high-fidelity models. Data-driven methods have also emerged based on simulation data, either relying on POD [25], Bayesian methods [26] or Deep Learning and Neural Networks [27]. Also, expansion in modal or basis functions [28] have been applied to design ROMs from experimental data. Moreover, the combustion representative data used for learning process often includes time-series of physical quantities of interest [5], [29], 3D fields [30] or images [31].

Objective: In this work, the detailed modeling of lean premixed inverted conical flames is proposed, using a skeletal chemical kinetic mechanism. The main goal of this work is to accurately model the ICF, its different time and space scales, its self-excited behavior and characterize its dynamic response due to incoming fluctuations. Our method consists in, first, developing a CFD model of such flames, enabling the detailed characterization of the flame dynamics. Second, the characterization of the flame behavior due to external forcing is developed is terms of flame transfer function. It is, however, challenging to achieve an accurate model of the ICF under acceptable computational burden, and for that a mesh adaptation tool is applied, and its impact on the simulation results is discussed. Third, a reduced order model is applied to predict the steady-state equilibrium profiles of various properties of the ICF, based on averaged CFD data. Finally, a novel approach to designing state observers for nonlinear dynamical systems is presented. The approach relies on the nonlinear Luenberger approach [32]–[35], which consists in designing a change of coordinates from the original system dynamics to a stable linear filter having the measurement as an input. We propose to numerically compute the associated mappings, rather than find its closed-form analytical expression. The approach is illustrated on a ROM describing the heat release dynamics of a simple flame.

Publications

The work developed on this thesis has resulted in the following publications:

Journals.

- **L. C. Ramos**, L. F. Figueira da Silva, F. Di Meglio, V. Morgenthaler, "Modeling of Pulsating Inverted Conical Flames: a Numerical: Instability Analysis", in *Combustion Theory and Modeling*, 2020. (Submitted: Under Review)

Conferences.

- **L. C. Ramos**, F. Di Meglio, V. Morgenthaler, L. F. Figueira da Silva, P. Bernard, "Numerical design of Luenberger observers for nonlinear systems", in *2020 IEEE Conference on Decision and Control (CDC)*, IEEE, 2020, pp. 5435-5442, doi: 10.1109/CDC42340.2020.9304163.
- **L. C. Ramos**, L. F. Figueira da Silva, F. Di Meglio, V. Morgenthaler, "Reduced order model of laminar premixed inverted conical fames", in *2020 AIAA Scitech 2020 Forum*, AIAA SciTech, 2020, p. 0411, doi: https://doi.org/10.2514/6.2020-0416.
- Junqueira, N., L. F. Figueira da Silva, **L. C. Ramos**, "Reduced order models applied to laminar diffusion flames", in *18th Brazilian Congress of Thermal Sciences and Engineering*, ENCIT, 2020, doi: 10.26678/ABCM.ENCIT2020.CIT20-0196.
- Junqueira, N., L. F. Figueira da Silva, **L. C. Ramos**, "The influence of the learning data on the reduced order model of laminar non-premixed flames", in *26 International Congress of Mechanical Engineering*, COBEM, 2021. (Paper Draft Submitted)

Outline

The chapters of this thesis is organized as follows.

Part I focuses on the description of the studied steady and dynamic flame.

Chapter 1 introduces the CFD modelling of a laminar axisymmetric lean premixed inverted conical flame, both for the steady state equilibrium and dynamic behavior. The necessary equations and discretization method are presented first, followed by the geometry, boundaries conditions and chemical kinetic mechanism used for the combustion. The software and setup used for the simulations are also given. Finally, results of the steady state simulations of the flame are analyzed and discussed. Part of the content presented in this chapter appeared in [36].

Chapter 2 first presents the impact of varying the mesh adaption temperature gradient on the dynamic of an ICF, under a forcing of 100 *Hz*. Second, the analysis of the ICF natural behavior is given, showing the benefits of using skeletal chemical kinetic mechanism to the combustion process, and the power and disadvantages of using CFD for such detailed and complex models. In this chapter, the flame is shown to be self-excited under the chosen setup, with a

strong dynamic oscillating response. Then, the detailed impact of forcing the flame with different excitations is given, followed by the characterization of the flame transfer function. Part of the content presented in this chapter has been submitted to publication in [37].

Part II focuses on the use of machine learning techniques for model reduction and obsevrer design purposes.

Chapter 3 Presents the development of a ROM of the steady state equilibrium of ICF. Steady ROM, from Twin Builder (Ansys), is used to develop a simplified model of the ICF based on averaged CFD data, presented in Chapter 1. The reduced models have the fuel/air mixture inlet velocity as input, and the fields of the velocity components and temperature obtained with Fluent as output.

Chapter 4 presents a numerical observer design for nonlinear systems. The approach consists in the approximation of the Luenberger observer mappings with a neural network used as nonlinear regression. Two methodologies are proposed; one for autonomous systems and one for excited systems, and both are presented in detail. The two methodologies are then applied to different test cases, and the results are presented and discussed. Part of the content presented in this chapter is being published in [38].

Part I

Computational Fluid Dynamic Modeling

Chapter 1

Inverted Conical Flame

Dans ce chapitre, une introduction sur la combustion, les flammes coniques inversées et la simulation numérique dynamique est donnée, suivie de la description mathématique du modèle CFD de la ICF. Le modèle s'appuie sur des principes physiques, tels que la conservation de la masse et de la quantité de mouvement, les équations de transport de l'énergie et des réactifs, pour un écoulement laminaire axisymétrique sur un brûleur Bunsen. Il intègre des conditions aux limites, des conditions initiales et un allumage numérique, liés à la modélisation de la combustion, ainsi que l'utilisation d'un outil d'adaptation du maillage. Comme illustré dans la Section 1.4.3, le modèle stable est capable de prédire le comportement global d'un système réactif aussi complexe que l'ICF, et sert de base aux Chapitres 2 et 3.

This Chapter describes the inverted conical flames under study in this manuscript, as well as the CFD model used to compute its steady-state properties and dynamic behavior. The model relies on first principles, such as mass and momentum conservation, energy and reactive transport equations, for a axisymmetrical laminar flow on a Bunsen burner. It incorporate boundary conditions, initial conditions and numerical ignition, linked to the modeling of combustion. As illustrated in Section 1.4.3, the model is capable of predicting the overall steady-state behavior of the complex reactive system that is the ICF, and serves as a basis for Chapters 2 and 3.

1.1 Introduction

The design of industrial systems involving combustion heavily relies on Computational Fluid Dynamics (CFD) simulations, enabling to predict and avoid instabilities. In cases where these may arise, three-dimensional, unsteady simulations which involve dozens of chemical species are often necessary to provide an adequate system characterization [39]–[41]. Even with an ever increasing computational power, performing a large number of such detailed simulations remains unfeasible in the design phase of novel combustors. As a consequence, instability identification could occur late in the design phase, thus leading to expensive reviews.

Lean premixed flames exhibit unstable behaviors in low emission systems [10], [42], hence these instability are reflected into more complex combustion systems, such as turbulent flames. To understand the physics of flame response to incoming velocity/pressure perturbations, several studies have been performed, both in combustors and laboratory flames [43]. Accordingly, investigations on flame instabilities carried on complex combustors [3], [44], show that mechanisms involving fluel/air equivalence ratio fluctuations are triggered by pressure oscillations at the injector exhaust, vortical/flame roll up, and that these interactions with hydrodynamic instability modes might be driving sources of unsteady motion [36], [44].

Nevertheless, laminar premixed inverted conical flames, which are anchored on a central bluff-body, feature such instability phenomena with a rather simple flow

field framework. Accordingly, there exists several studies on these flames, either based on laboratory [9], [10], or on CFD models [36]. Thereby, the inverted conical flame is also representative of more complex situations, such as aircraft gas combustors, enabling the further understanding of the combustion process in rather simpler system.

Therefore, in this chapter a laminar axisymmetric premixed inverted conical flame (ICF) is modeled and analyzed on a burner which has cylindrical rod on its center. In Figure 1.1 this flame position is represented by the computed instantaneous mass fraction field of OH, enabling the verification of the flame anchoring point on the central rod, and the overall inverted conical shape. Classically, the premixed flame front separates the fuel/air mixture from the combustion products.

More specifically, the experiment studied an unconfined configuration [9] which typifies more complex situations where thermo-acoustic instabilities are driven by the flame interaction with a convective vorticity mode. This ICF exhibits self-sustained oscillations for certain operating conditions, involving the sudden annihilation of flame surface area, caused by a strong interaction between the flame and vortices created at the shear layer that develops at the burner outer edge. The experimental transfer functions between the flow velocity and heat release fluctuations are dependent on the velocity perturbation amplitude and frequency, and the time delay is determined by the convection of the large scale vortices.

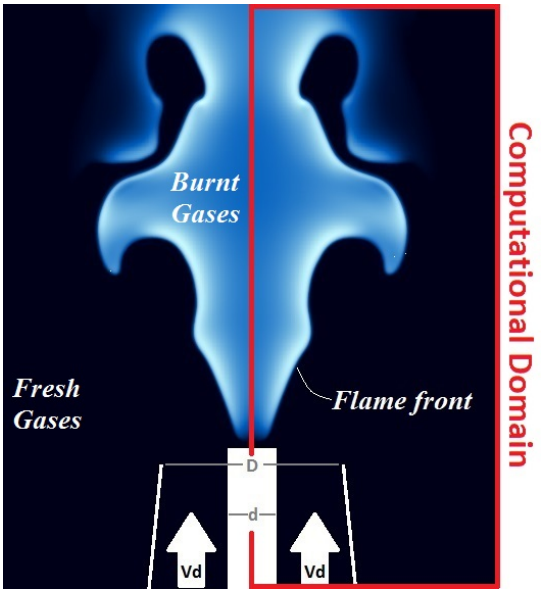


FIGURE 1.1: Representative view of OH mass fraction for the unsteady inverted conical flame. Mean velocity of $v_d = 2.05\ m/s$ and metane/air equivalence ratio $\phi = 0.92$, $T_\infty = 300\ K$ and $p = 1\ atm$ [36].

The flame modeled here is based on the experimental study by [9], where a burner outlet diameter of $D_b = 22\ mm$ is used, represented on Figure 1.5, fed with a lean methane-air mixture, with equivalence ratio $\phi = 0.92$. The flame is anchored by a central cylindrical rod with a diameter of $d = 6\ mm$, and it is 2 mm higher than the burner outlet. All the model main equations, numerical methodology, domain and measures and other features used for the developing computational model are discussed in Sections 1.3 and 1.4. A discussion and analysis of the steady model simulation results are presented in Section 1.6.

1.2 1D Flame Model

In this section the chemical kinetic mechanism used to describe the combustion process is presented. It is followed by the presentation of a preliminary 1D Chemkin model used to define important parameters that are necessary to properly create the a base combustion model.

1.2.1 Skeletal chemical kinetic flame model

To model the combustion process of premixed methane/air, the chemical kinetic process is described by a skeletal model. Different from global kinetic models, the skeletal chemical model also includes the production of intermediate species, before the major species formation. Skeletal kinetic models can follow different paths between the oxidation steps, such that the analytic understanding of those becomes extremely complex. Figure 1.2 presents an example of steps used to describe the combustion process for methane or ethylene [45].

In Figure 1.2, the paths of the leftmost vertical group are the ones that do not have substances with two carbon atoms (C_2), important for reactions in high pressure or rich combustion. The chemistry involving C_2 is initiated through the recombination of CH_3 with other species. It is worth to note that, in this scheme, the initial step needs a high activation energy to remove the hydrogen from the molecules.

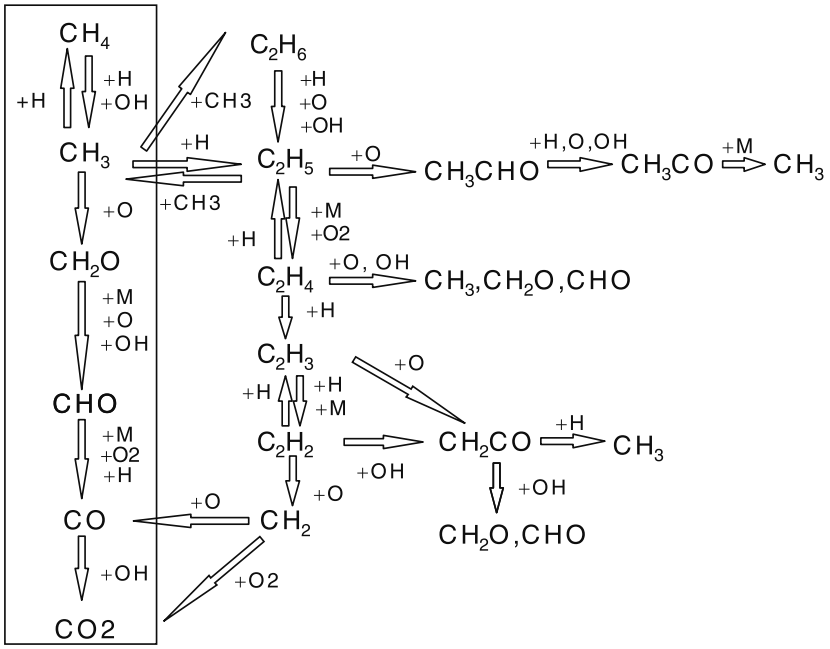


FIGURE 1.2: Simplified representative scheme of a detailed kinetic model for methane combustion [45].

The skeletal model used is the DRM19, which is a reduced GRI-Mech 1.2 kinetic model. It is developed by truncation of the original GRI-Mech, with the objective of developing a smallest set of reactions [46]. The GRI-Mech 1.2 model is composed of 32 species and 177 reactions, which yields a large computational cost. Because of

this, a reduced model is used in this work. The DRM19 skeletal kinetic model is composed of 19 (plus N_2) species and 84 reactions [46]. Previous assessment of skeletal model accuracy in the context of combustion supports this choice [47]. The use of such a detailed model enables the analysis of a variety of chemical species during the combustion process, and the DRM19 reproduces closely the main combustion characteristics predicted with the original GRI-Mech, with a lower computational cost.

One may note that, since a lean premixed flame is modeled, it does not present soot formation and thermal radiation is neglected. The radiation medium emission relies on CO_2 and H_2O at the burnt gases only, which is significantly smaller than the convective heat transfer contribution. As a consequence, the flame may also be considered transparent regarding the absorption process.

1.2.2 Preliminary model: definition of flame scales

In order to develop a computational model of premixed laminar flames, it is necessary to define the flame associated scales, which must be known beforehand, such as the laminar flame front speed and the thickness for the specific modeled flame. Accordingly, the software CHEMKIN-Pro, which enables the modeling of kinetic mechanism used on combustion, is applied to create a one dimensional model of a steady premixed methane-air flame, with an skeletal kinetic chemical model for the combustion (DRM19 kinetic model [46]).

The main features obtained as solution are: (1) fluid domain spanning from -2 to 5 cm, (2) an adaptive grid control based on the solution curvature and gradient threshold of 0.7 and 0.2 respectively, and (3) the laminar flame front speed $S_L = 40$ cm/s. The minimum mesh size found is 5.6 μm. This simple CHEMKIN-Pro model using the DRM19 kinetic model enables the analysis of diverse flame properties and its different scales. For the sake of brevity, only three properties are discussed here; OH and CH_2 mass fraction, and temperature. These three properties are used to characterize the large difference between the scales of each flame property, both in terms of magnitude and characteristic length. Indeed, the OH mass fraction is often used for experimental flame measurements, and CH_2 is a good indicator of the flame front position and thickness. In order to examine these properties, the fields of the mass fraction of CH_2, OH and the temperature are depicted in Figures 1.3 and 1.4.

Figure 1.3 shows that CH_2 and OH are absent upstream to 0 cm, where the temperature is 300 K. The temperature then increases up to approximately 800 K and gives rise to the combustion, such that significant amounts of CH_2 and OH are seen because of the combustion process has started. The position of the flame front is highlighted by the increase in CH_2 and OH mass fraction. The CH_2 is consumed immediately downstream and its mass fraction decreases to zero, indicating thermodynamic equilibrium. The OH mass fraction, however, presents a maximum at the flame front, then gradually tends to an equilibrium concentration as $x \to 5$ cm. The temperature increases along the flame until it reaches the adiabatic flame temperature $T_{ad} = 2,200$ K.

A focus on the flame front location is depicted on Figure 1.4. It emphasizes the large difference between the different flame properties length and time scales, such as temperature and mass fraction of OH. Indeed, the length scales varies from 300 μm to 40 mm until equilibrium is achieved. Also, the mass fraction profiles indicates that the flame reaction zone thickness is around 120 μm, based on the OH and CH_2 gradients. Also, it may be inferred that the smaller mesh size required to obtain

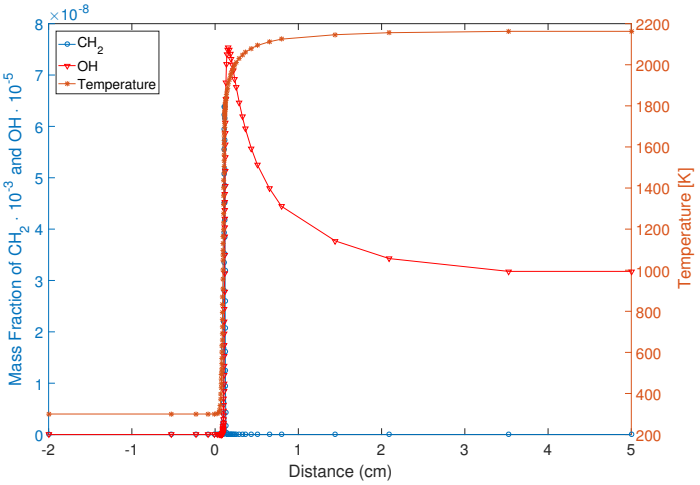


FIGURE 1.3: Fields of mass fraction of CH_2 and OH, and temperature (K) obtained for the 1D freely propagating laminar premixed methane/air flame, with equivalence ratio of $\phi = 0.92$, $T_\infty = 300\ K$ and $p = 1\ atm$ [36].

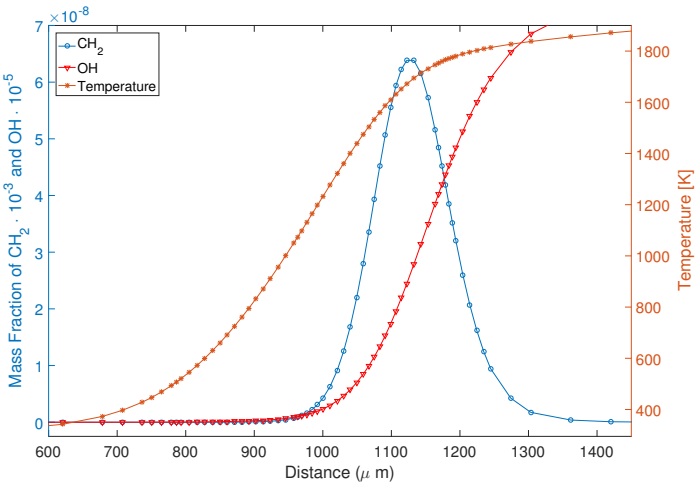


FIGURE 1.4: Zoom on the fields of mass fraction of CH_2 and OH, and temperature (K) obtained for the 1D freely propagating laminar premixed methane/air flame, with equivalence ratio of $\phi = 0.92$, $T_\infty = 300\ K$ and $p = 1\ atm$ [36].

a well resolved gradient and curvature of the laminar premixed flame properties is of the order 5 μm, which is $\approx$ 25 times smaller than the flame reaction thickness.

1.3 Computational Fluid Dynamics Model

In this section, equations describing the Fluent software solver used to model the combustion process of the burner is described, followed by the domain, boundaries and mesh used for the CFD model.

1.3.1 Governing equations

The model consists of the conservation laws of mass, momentum and energy of all species in an axisymmetric 2D reference frame. In the combustion process no mass is created or destroyed, which yields the following total mass conservation law [45]

$$\frac{\partial \rho}{\partial t} + \nabla \cdot (\rho \vec{v}) = 0, \tag{1.1}$$

where ρ is the mixture density and $\vec{v}$ is the flow velocity vector ant t represents the time.

In this work, the chemical kinetic process is described by a skeletal model, as presented in Section 1.2.1, composed by a total of I species. The species mass transport equation, then, is solved accounting for the multi-species diffusion coefficients, the Soret diffusion effects, but neglecting the barodiffusion effects since the flame is nearly isobaric. This way, the mass balance of each one of the I substances is defined by [45]

$$\frac{\partial \rho Y_i}{\partial t} + \nabla \cdot (\rho \vec{v} Y_i) = \nabla \cdot (\rho D_i \nabla Y_i) + \dot{\omega}_i \quad i = (1, \cdots, I), \tag{1.2}$$

where D_i is the mass diffusion coefficient of the species i in relation to the gas mixture, $\dot{\omega}_i$ the mass production rate of the species i due to the chemical reactions and Y_i is the mass fraction of each species.

Assuming the chemical expression of a general elementary reaction is

$$\sum_j a_{j,i} \mathcal{M}_j \rightarrow products, \tag{1.3}$$

where $a_{j,i}$ are the stoichiometric coefficients of species $\mathcal{M}_j$ in reaction i. The corresponding rate of reaction is expressed as

$$\dot{\omega}_i = \pi_i [X_j]^{aj}, \tag{1.4}$$

where $[X_j]$ are the molar concentration of species $\mathcal{M}_j$. The constant of proportionality K_i, also called the Arrhenius rate constant, is of he following form [45]

$$K_i = A_{0,i} T^{\beta_i} \exp\left(\frac{E_{a,i}}{RT}\right), \tag{1.5}$$

where $A_{0,i}$ is the frequency factor, β_i temperature exponent, E_a its the activation energy, and $R = 1.987\ cal/mol - k$ is the universal gas constant.

In Equation (1.2), the Fick's law of diffusion accounts for the rate equation for mass diffusion [48], as

$$\vec{j_i} = -\rho D_i \nabla Y_i, \tag{1.6}$$

where j_i is defined as the diffusive mass flux of species i.

The conservation of momentum reads

$$\frac{\partial \rho \vec{v}}{\partial t} + \nabla \cdot (\rho \vec{v} * \vec{v}) = -\nabla p + \nabla * \tau + \rho \vec{g}, \tag{1.7}$$

where p is pressure, $\vec{g}$ is the vector of gravity acceleration and τ is the viscous stress tensor, i.e.

$$\tau = -\left(\frac{2}{3}\mu - \eta\right)\nabla\cdot\vec{v}I + \mu\left(\nabla\vec{v} + \nabla(\vec{v}^T)\right), \tag{1.8}$$

where μ is the dynamic viscosity which is discussed bellow, η volumetric viscosity and I the identity tensor. The energy transport equation accounts for the non unity Lewis number effects, but thermal radiation is neglected since the modeled flame is a lean premixed flame, which does not presents soot formation. The energy equation [45] reads

$$\frac{\partial\rho h}{\partial t} + \nabla\left(\rho\vec{v}h\right) = \nabla\cdot\left(\rho\alpha\nabla h\right) + \sum_i\left\{\nabla\cdot\left[\left(h_i\right)\left(\rho D_i - \alpha\right)\right]\nabla Y_i\right\} + \frac{\partial p}{\partial t} + \vec{v}\cdot\nabla p, \tag{1.9}$$

where α is the thermal diffusion coefficient of the mixture, h is the enthalpy, h_i is the enthalpy of the chemical species i and D_i is the mass diffusion coefficient of the species i with respect to the gas mixture.

1.3.2 Equations of state and constitutive relations

All gas are assumed to satisfy the ideal gases law as follows

$$p = \rho RT\sum_i\left(\frac{Y_i}{M_i}\right), \tag{1.10}$$

where M_i is the molecular mass of the species i and R the universal gas constant. The temperature can then be determined with the heat state equation, as follows

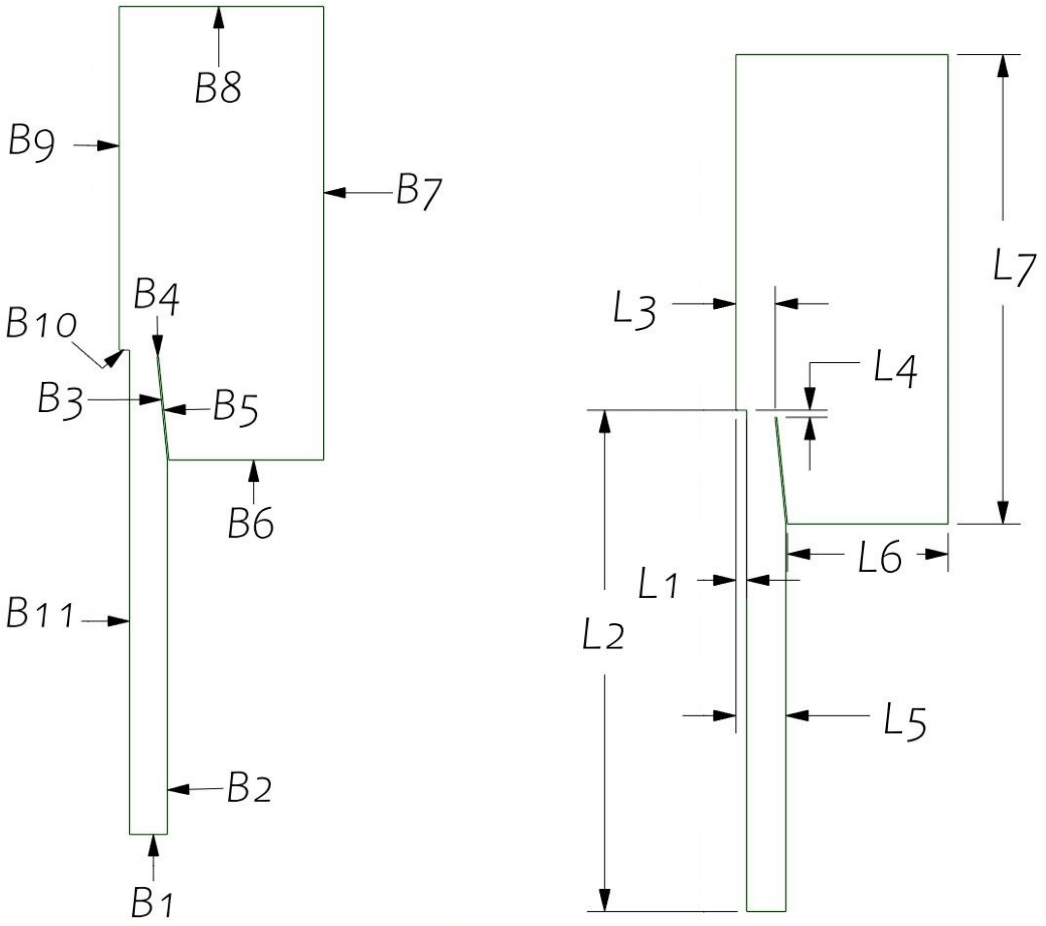
$$h = \int_{T_{std}}^{T} C_p dT + \sum_i Y_i h_i^0, \tag{1.11}$$

with $C_p = \sum_{i=1}^{I} Y_i C_{p,i}$ the specific heat at constant pressure of the mixture, T_{std} the standard temperature where the enthalpy is defined (usually $T_{std} = 25^oC$), and h_i^0 is the enthalpy of formation at the standard state. The specific heat of the mixture at constant pressure $\left(C_{p,i}\right)$ is obtained with the JANAF database [49]. The mixture properties, such as the viscosity (η) and and the diffusion coefficient (D_i) are computed base on the pure substance properties, such that a polynomial fitting in function of physical parameters, e.g., temperature and pressure, is applied to compute the properties for each mixture. For more information about computations, the reader must refer to [50].

1.3.3 Domain, boundary conditions and mesh

Since the flame is axisymmetric, the spatial domain here is composed of a 2D slice. The system has eleven boundaries, where six are walls, two inlets, one outlet, one axis and one slip boundary, as presented on Figure 1.5. The physical assumptions for each of these boundaries are presented in Tab. 1.1.

One may note that the boundary B_7 is an open to the environment, but it represented here as slip, adiabatic non catalytic wall. Also, the *axis* (boundary B_9) represents the symmetry of the system. All the other walls (B_5, B_{10} and B_{10}) are no-slip adiabatic non catalytic walls. Moreover, the two inlets represent the inlet of the fuel air mixture (B_1) and of air (B_6). The first one, where the premixed gases enters, is represented by the velocity inlet boundary B_1, whereas at the second one, the velocity inlet boundary B_6, air enters with a small constant velocity of $v_{air} = 0.3\ m/s$.



(A) Boundaries references.

(B) Dimensions used to specify the computational domain.

FIGURE 1.5: Representation of the axisymetric computational domain with corresponding boundary conditions and dimensions labels. The boundary conditions setups and measures are given at Tabs. 1.1 and 1.2 respectively.

This air flux is imposed such that the air flow in the domain moves downstream. One may note that the value ($v_{air} = 0.3\ m/s$) is chosen based on the Froude number

$$Fr = v_{air}/\sqrt{g\bar{L}}, \tag{1.12}$$

where g is the acceleration due to gravity and L is the flame length. Considering $\bar{L} = 10\ mm$ leads to a $Fr = 0.96$. The Froude number might be less or equal one ($Fr \leq 1$) to allow for neglecting outer convective effects. Imposing a positive air velocity helps the simulation convergence, whereas using a zero air velocity was found to leads to backward flow at the outlet boundary.

The domain dimensions, represented on Figure 1.5b, are given in Tab. 1.2. It is worth to note that the length L_7 controls the extension of the domain, which needs to be large enough to ensure that the flow is developed when reaching the outlet boundary. In addition, the L_6 distance between the flame and the lateral boundary (L_7) must be large enough so that the flame does not interfere with the wall, since the model approximates a non confined flame.

Finally, three distinct regions are defined with different mesh properties. The

TABLE 1.1: Boundary conditions of the CFD model.

Setup	Boundary (B_i)
Velocity Inlet	B_1, B_6
Pressure Outlet	B_8
No-slip Wall	B_2, B_5, B_{10}, B_{11}
Slip Wall	B_3, B_4, B_7
Axis	B_9

TABLE 1.2: Dimensions L_i, characteristic of the CFD domain, in $[mm]$.

Label (L_i)	L_1	L_2	L_3	L_4	L_5	L_6	L_7
Measures $[mm]$	3	141	11	2	14	135.5	650

internal region (M_1) includes the fuel/air inlet tube and the flame region. The two external regions (M_2 and M_3), account for the air flow and the dilution of the burned gases in air. These have initial mesh sizes of 1 mm and 5 mm, respectively: such coarse values ease the computational burden.

In (M_1), it is necessary to account for the boundary layers along the bluff-body and the burner walls and, also, the reactions that arise at the flame. Then, the initial mesh size is chosen to be smaller then 100 μm, which is of the order of the flame front thickness and ensures the existence of at least a mesh node inside of the reactive region. A mesh adaptation tool, briefly described in Section 1.4.4, is then used to compute a grid that ensures a proper resolution of the flame front in M1, consistently with the results of Section 1.2.2.

1.4 Numerical Methodology

The model described in the previous section is numerically solved with a finite volume method using Ansys Fluent. First, the finite volume formulation is given, followed by the physical solver methodology. Then, the necessary changes to develop a steady model are presented, followed by the mesh adaption methodology.

1.4.1 Transient finite volume method

To model the transient ICF, a temporal discretization is applied, involving the integration of all terms in the differential equations, over a variable time step Δt. This way, the general discretized form is obtained from the generic conservation equation of transport of a scalar quantity φ;

$$\int_V \frac{\partial \rho \varphi}{\partial t} dV + \oint \rho \varphi \vec{v} \cdot d\vec{A} = \oint \Gamma_\varphi \nabla_\varphi \cdot d\vec{A} + \int_V S_\varphi dV, \tag{1.13}$$

where ρ is the density, $\frac{\partial \rho \varphi}{\partial t}$ is the conservative form of transient derivative of transported variable, $\vec{v}$ is the velocity vector, $\vec{A}$ is the surface area vector. The Γ_φ is diffusion coefficient of the variable φ, ∇_φ is the gradient of φ and S_φ is the source of φ per unit volume. This formulation is then applied for each cell, in this case, of a 2D axisymmetric domain, such that the discretization of Equation (1.13) on a given cell yields the following equation

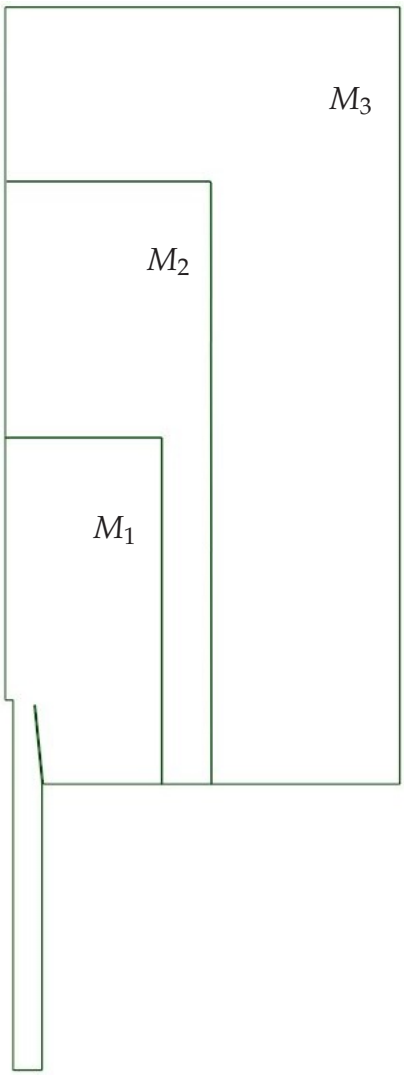


FIGURE 1.6: Axisymmetric computational domain blocks division. M_1: is the block where the flame is encountered; M_2, M_3: are the blocks where the air and burned gases flow.

$$\frac{\partial \rho \varphi}{\partial t} V + \sum_{fc}^{N_{faces}} \varphi_{fc} \rho_{fc} \vec{v}_{fc} \vec{A}_{fc} = \sum_{fc}^{N_{faces}} \Gamma_\varphi \nabla_{\varphi fc} \cdot \vec{A} + S_\varphi V, \tag{1.14}$$

where N_{faces} is the number of faces enclosing cell, fc is the face index and $\rho_f \vec{v}_f \vec{A}_f$ is the mass flux through the face. More precisely, to compute the time dependent $\frac{\partial \rho \varphi}{\partial t}$, an implicit second order transient scheme is applied with a constant time step, as following

$$\frac{\partial \varphi}{\partial t} = \frac{3\varphi^{(n+1)} - 4\varphi^n + \varphi^{(n-1)}}{2\Delta t}. \tag{1.15}$$

Since the simulation time step is constant and equal to 100 μs, the flow Courant number is only used to stabilize the convergence behavior, and its maximum value is 0.41. The relaxation factor for momentum and pressure is 0.75, and it defines the explicit relaxation of variables between sub-iterations for momentum and pressure [51]. The density, body forces, species and energy equation under relaxation

factor (URF) is 1, and for species all URFs are set together, which means that the same under-relaxation factors are used for all the species.

1.4.2 Solver methodology

In this work a pressure based solver is used, employing an projection algorithm where the constraint of mass conservation of the velocity field is found by solving a pressure or pressure correction equation. The pressure equation is derived from the continuity and the momentum equations, such that the velocity field, corrected by the pressure, satisfies the continuity [52]. A coupled algorithm is used to solve the governing equations (i.e., velocity $\vec{v}$, pressure p, etc.) simultaneously, and the solution cycle is carried out iteratively until a threshold of numerical convergence is reached. The pressure based coupled solution scheme is given on Figure 1.7. The steps of the solver are

1. Update the fluid chemical properties, e.g., viscosity, density and specific heat, based on the current solution.
2. Solve the momentum (i.e., velocity, mass flux, etc) and pressure correction based continuity equations using the updated properties.
3. Correct the faces pressure, velocity components and mass fluxes with the pressure correction obtained at the previous step.
4. Sequentially, solve the energy, species and additional equations, with the current solution variable values.
5. Check if convergence is achieved.

This process iterates until the convergence criterion is achieved. In this case, two convergence criteria are used; first, the simulation has converged if the residual off each equation is less than or equal to 10^{-3}, and second, if the loop achieves 20 iterations. Such values are the default values from Fluent transient models [51].

Moreover, the mixing and transport of chemical species are computed by solving the conservation equations describing convection, diffusion, and reaction sources for each component species, as shown in Section 1.3.1. Simultaneously, multiple chemical reactions are modeled, such that the reactions occur in the fluid phase, described by volumetric reactions, and are solved with the stiff chemistry solver [51], [53], at step 4 of the process. One may note that here an mesh adaption tool is also used during the simulation, being applied for a specific period, as explained in Section 1.4.4. The modeling of stiff chemistry systems, such as flames with finite-rate kinetics, approximates the reaction rate ($\dot{\omega}^*$) in the species transport equation (1.2) as;

$$\dot{\omega}_i^* = \frac{1}{\Delta t}\int_0^{\Delta t} \dot{\omega}_i dt, \tag{1.16}$$

where Δt is the time-step. It is worth to note that as $\Delta t \to 0$, the approximation becomes exact but the stiff numeric will cause the pressure-based solver to diverge [52]. On the other hand, as Δt tends to infinity, the approximated reaction rate tends to zero and, while the numerical stiffness is alleviated, there is no reaction.

In addition, to compute the chemical species properties, which depends on the flow dynamic states, the In-Situ Adaptive Tabulation (ISAT) table is applied to integrate the stiff chemistry (Equation (1.16)) during the simulation [51]. ISAT is a

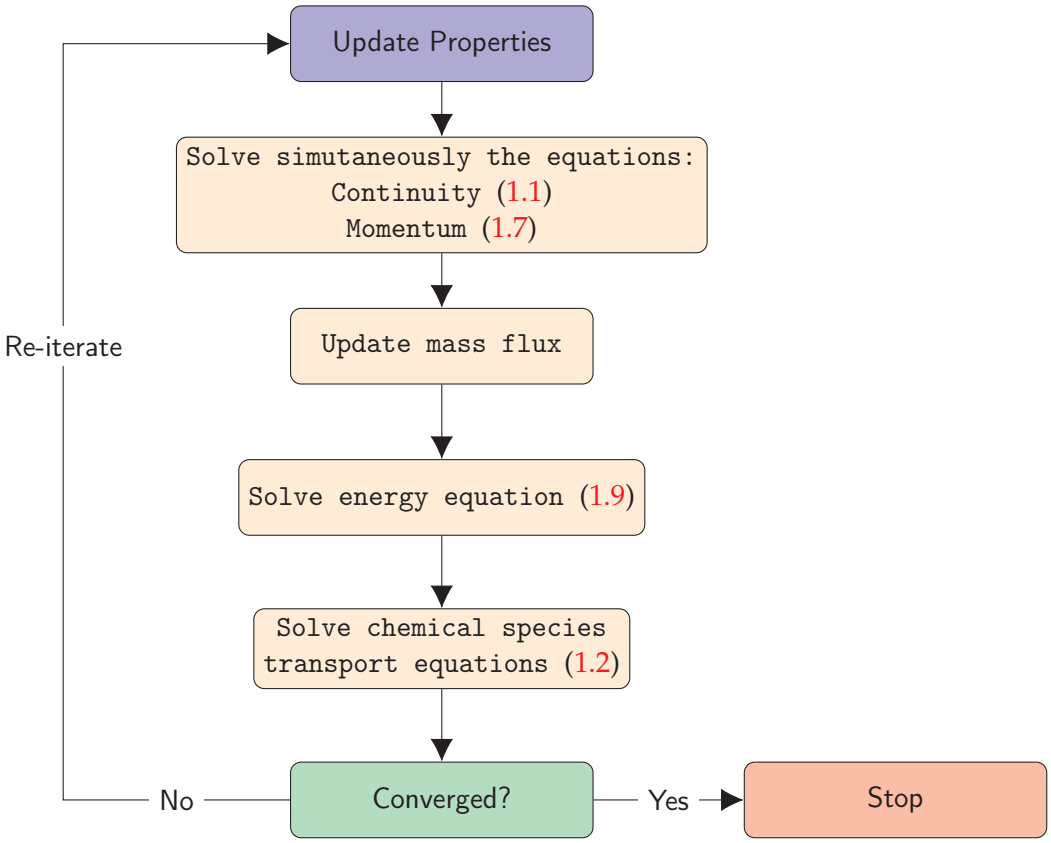


FIGURE 1.7: Flow chart representation for Fluent solution process.

method to tabulate the accessed composition space region on the fly, with error control, i.e., adaptive tabulation. This method accelerates the simulation in two to three orders of magnitude. ANSYS Fluent employs ISAT table to dynamically tabulate the chemical properties, mapping the species properties in such table and accelerating the time to solution [54]. In this work, the stiff integration parameters are the absolute and relative error tolerance of 1^{-10} and 1^{-5}, respectively, while the ISAT parameters are the error tolerance of 1^{-5}, maximum storage of 400 *Mb* and zero verbosity, all set based on [51], [55], [56]. In addition, no Turbulence Chemistry Interaction (TCI) is used, such that only the Arrhenius rate (1.5) is computed and turbulence-chemistry interaction is neglected, and diffusion energy source and thermal diffusion (Soret effects) are assumed.

To solve the equations, the flow properties gradient is necessary to discretize convection and diffusion terms in the conservation equations, and here the spatial discretization scheme used is least square cell based [51], [52]. The pressure interpolation applied is the PRESTO! scheme (PREssure STaggering Option), which uses the discrete continuity balance for a staggered control volume about the face to compute the face pressure. Such procedure is similar to the staggered-grid schemes used with structured meshes [57]. The pressure-velocity coupling scheme used here is COUPLE, which solves momentum and pressure-based continuity equations together [51]. The full implicit coupling is achieved through an implicit discretization of pressure gradient terms in the momentum equations, and an implicit discretization of the face mass flux. For momentum, species and energy, the second order upwind scheme is applied for spatial discretization, which gives a second-order accuracy and the quantities at cell faces are computed with multidimensional linear reconstruction approach [58]. In this approach, second-order accuracy is achieved

at cell faces through a Taylor series expansion of the cell-centered solution about the cell centroid. The second order upwind then gives the value at the face (φ_f) as;

$$\varphi_f = \phi + \nabla\varphi \cdot \vec{r}, \tag{1.17}$$

where φ and $\nabla\varphi$ are the cell-centered value and its gradient at the upstream cell for a flow property, and $\vec{r}$ is the displacement vector from the upstream cell centroid to the face centroid, as presented by [51], [52]. This formulation requires the determination of the gradient in each cell, as discussed in Section 1.4.1.

1.4.3 Steady-state model

When performing a steady-state calculation, the governing equations (Section 1.3.1) for the pressure-based solver do not contain time-dependent terms. Moreover, the general dicretized form given at equation (1.14) then, loses its time dependent term ($\frac{\partial\rho\varphi}{\partial t}$), as shown in Equation (1.18), describing then the control volume based discretization of the steady-state transport equation.

$$\sum_{f}^{N_{faces}} \varphi_f \rho_f \vec{v}_f \vec{A}_f = \sum_{f}^{N_{faces}} \Gamma_\varphi \nabla_{\varphi f} \cdot \vec{A} + S_\varphi V, \tag{1.18}$$

The same transient process and parameters for the CFL number and relaxations are are applied for the steady state simulations.

1.4.4 Mesh adaption methodology

Mesh adaption is a tool that enables continuous or batch refinement and/or coarsening of the mesh characteristic size based on the properties of the current numerical solution [59]. In this work, the mesh adaption tool is applied to decrease the characteristic mesh size at the regions where a small size is needed, i.e., the combustion region, which is discussed in Section 1.2.2. More precisely, here the mesh adaption is controlled by the gradient of temperature, such that, in the regions where the temperature gradient is higher than a threshold value $\Delta T_{refine}\ (K/m)$, the mesh is refined, and at the regions of the mesh where the temperature gradient is lower than a second threshold $\Delta T_{coarse}\ (K/m)$, the mesh is coarsened [51]. The value of the thresholds is determined through a trial-and-error procedure, trading-off accuracy with computational burden. This point is further illustrated in Section 2.2, at the light of transient simulations.

To visualize the impact of the mesh adaption, Figure 1.8 shows a representation of the mesh changes in the region M_1 due to the adaption using a temperature gradient threshold of $\Delta T_{refine} = 10\ K/m$ and $\Delta T_{coarse} = 300\ K/m$. On the left side, the figure shows the base mesh, with a characteristic mesh size of 100 μm and, in the center, a representation of an adapted mesh after the flame is developed. On the right, a zoom on the adapted mesh is represented. A comparison between Figures 1.1 and 1.8, shows that the mesh is refined in the flame front region, where the temperature gradient is high and the combustion process occurs. The initial regular mesh, on the left of Figure 1.8, is composed of 509,473 cells, whereas the mesh, at the last instant of the simulation, presents 2,427,310 cells.

The mesh adaption can be applied to either steady state or transient simulation. In the first case, this approach enables the mesh to refine and vary with the flame position before a permanent state is achieved, such as between when the flame is ignited and when it is completely developed and converged to its equilibrium state.

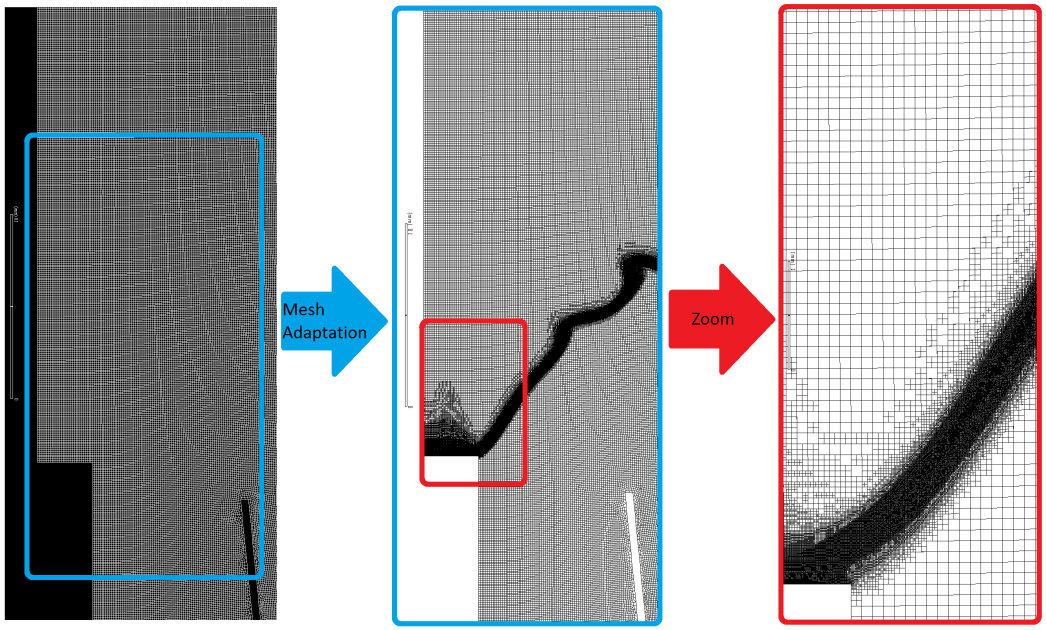


FIGURE 1.8: Representation of the mesh adaptation due to temperature gradient (obtained using Fluent). Left: base mesh with a size of 100 μm; center: mesh already adapted after the flame is developed; right: zoom on the adapted mesh.

For the steady simulation, the mesh adaption is set to adapt the mesh at every 25^{th} step. For the transient simulation, the mesh adaption process is every 5 time steps. For all cases, the maximum level of refinement is 12, which means that the mesh characteristic size (Δx) can be divided $\Delta x/2^{12}$.

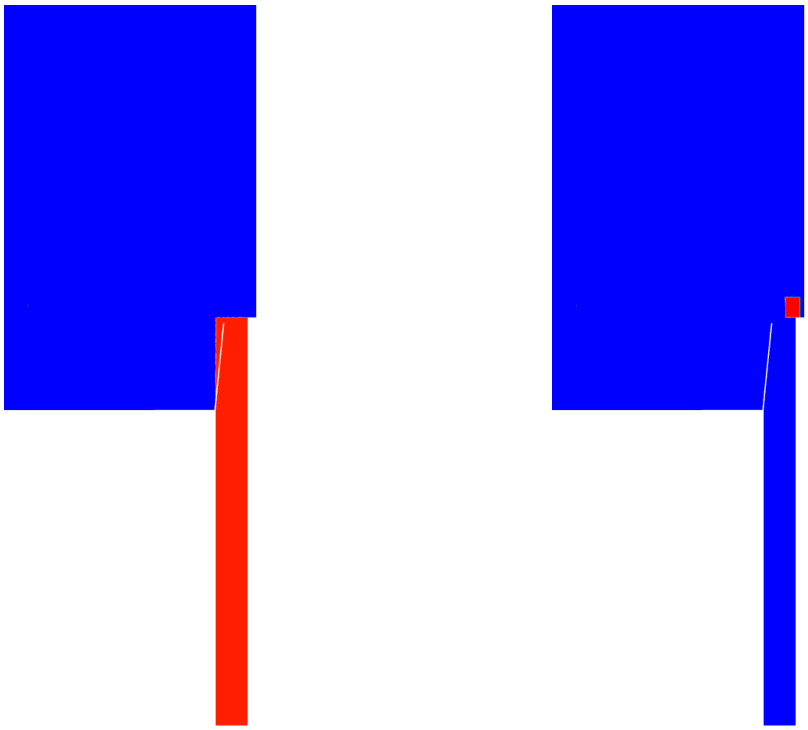
1.4.5 Numerical ignition

The computation of the steady-state of the ICF constitutes a nonconvex, nonlinear optimization, and therefore requires a proper initialization procedure. To avoid local optima, where no combustion happen, an appropriate initial guess is constructed, relying on physical considerations. This process is referred to as 'ignition' and follows the following steps:

- Define appropriate initial conditions for species concentrations by filling the burner with premixed methane/air fuel and the rest of the domain with air.
- Inquire the flame at the burner outlet by imposing a high temperature in a small region of the domain.

The first step is done by initializing the domain by patches, such that the first patch is defined by the rectangle region inside the mixture feed tube, with lateral and radial measures equal to 141 mm and 11 mm, respectively, corresponding to the red region on Figure 1.9a. The second patch is initialized only with air, which corresponds to the blue region on Figure 1.9a. Then, the corresponding steady equilibrium is computed, for the purpose of an isotherm computation, where no flame is present, such that the field of species concentrations converge to reasonable values.

The next step is to ignite the flame. This is done by increasing the temperature on the region where the premixture. The high temperature which is imposed there



(A) Premixed fuel and air patch for the purpose of an isotherm computation.

(B) Ignition patch for the purpose of a flame computation.

FIGURE 1.9: Representation of the computation initialization patches.

is chosen based on the preliminary analysis presented in Section 1.2.2, where it is shown that the reactive process starts around a temperature of 1200 K. Then, a patch with lateral and radial measures 8 and 5 mm, respectively, placed tangential to the top of the centralized rod, and with a distance of 1.5 mm from the axis is created, and the 1200 K temperature is imposed on it. Such setup is represented on Figure 1.9b, where the temperature of 1200 K corresponds to the red region, and the blue region corresponds to the ambient temperature.

Ignition is developed with a mesh adaption refinement threshold of 10 K/m, which was was chosen by trial and error. Higher thresholds have shown to be inefficient to the flame ignition, not being enough to stabilize the flame anchored at the centralized rod, causing then, the flame blow-off. The ignition process is performed only once, on a Linux-64 SuSE, at ANSYS cluster, Intel(R) Xeon(R) E5-2660 v3, using 108 nodes on 9 machines, taking about 1 month for the flame to be completely developed, and once the flame is developed and stabilized on the bluff body, this instant and its respective properties profiles are used as initial conditions for other ICF simulations.

1.5 Outputs of interest

To better understand and analyze the CFD results, this section presents the definition of important variables and properties that are crucial for the comprehension of

this work. First, the definition of the probe points used to extract data from the simulation is given, then, the flame surface area definition for the CFD model of the ICF is given.

1.5.1 Properties measurement probes

To study the evolution of some of the computed reactive flow properties, twenty analysis points are set in the flame fluctuation region. These points span four horizontal lines along the flame height (z =constant), each containing five points, as shown on Figure 1.10. These points coordinates are empirically chosen such that, at any time and for any shape of the ICF, there is at least one measurement in each of the following important regions: the fresh gases, the reactive region or flame front and the burned gases. In Figure 1.10, the placement of the points of data extraction are superimposed on the flame front, each labeled from A to T. The coordinates of these points in the normalized (z, r) plane are presented in Tab. 1.3.

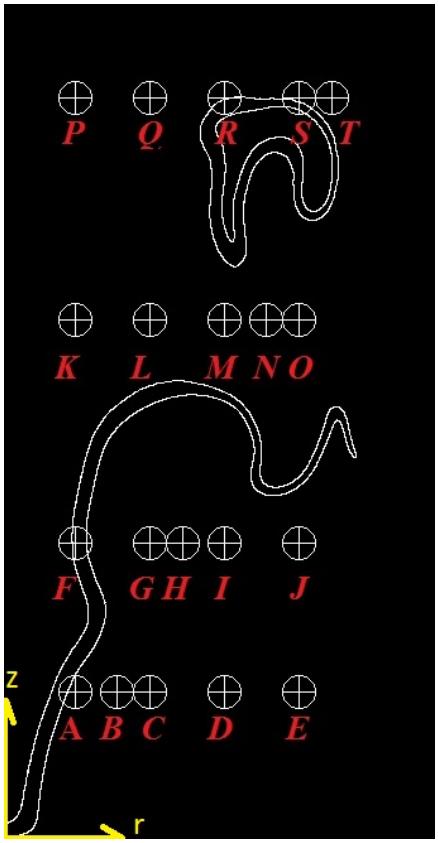


FIGURE 1.10: Data extraction points in the flame region and outline of fluctuation flame surface.

These points are used as measurement probes, to analyze various flame properties and its transient behavior. It is worth to note that the flame position and dynamics, as well as the mesh adaption during simulation do not interfere on the probes position, which are fixed on the geometry.

1.5.2 Flame surface area

The flame surface area is obtained from the CFD species results, enabling the characterization of the flame front position and dynamic behavior. It should be noted that

TABLE 1.3: Point name and corresponding (z^*, r^*) non dimensional coordinates of each point shown on Figure 1.10. These are no dimensional axial and radial coordinates, such that $z^* = z/D$ and $r^* = r/D$, where $D_b = 22\ mm$ is the $mixture - inlet$ tube outlet diameter.

A	B	C	D	E
(0.41, 0.20)	(0.41, 0.32)	(0.41, 0.41)	(0.41, 0.61)	(0.41, 0.82)
F	G	H	I	J
(0.82, 0.20)	(0.82, 0.41)	(0.82, 0.50)	(0.82, 0.61)	(0.82, 0.82)
K	L	M	N	O
(1.43, 0.20)	(1.43, 0.41)	(1.43, 0.61)	(1.43, 0.73)	(1.43, 0.82)
P	Q	R	S	T
(2.05, 0.20)	(2.05, 0.41)	(2.05, 0.61)	(2.05, 0.82)	(2.05, 0.91)

a flame surface area is not unambiguously defined from the reactive flow properties. Indeed, the experimental results available consider that the OH^* chemiluminescence represents the reaction rate and thus the flame surface area. Here, to compute the flame surface area, it is necessary to, first, chose which of the modeled flame properties better approximates the flame front. For the ICF model computed with a DRM19 kinetic model, the CH_2 mass fraction is assumed to yield a fair representation of the flame front shape and thickness, since it is a substance produced and consumed in the reactive region, as show in section 1.2.2. Thus, to define the flame surface from the CH_2 mass fraction field (Y_{CH_2}), a binary variable ι is defined, such that $\iota = 1$ denotes the flame front location. At each location x and time t, $\iota(x,t)$ is defined as follows

$$\varsigma(x,t) = Y_{CH_2}(x,t) - \frac{Y_{CH_2}^{max}}{\sigma}, \qquad \iota(x,t) = \frac{1}{2}\left(\frac{\varsigma(x,t)}{(|\varsigma| + \epsilon)} + 1\right), \tag{1.19}$$

Here, $\epsilon = 10^{-16}$ is the machine zero, $Y_{CH_2}^{max} = 6.25 \times 10^{-7}$ is the computed maximum CH_2 mass fraction and σ controls the resultant thickness of the flame front. In this case, $\sigma = 10$ is used to obtain the necessary flame thickness of 120 μm. The result of this transformation is depicted on Figure 1.11. Different choices of the parameters defining ι in Equation (1.19) have been explored. The choice of parameters for Equation (1.19), such as $Y_{CH_2}^{max}$, is finally made enabling the binary flame surface area to achieve a flame front thickness approximately of 120 μm, the same value encountered at section 1.2.2.

The isosurface of each of the $\iota(x,t)$ fields is then extracted, to obtain the flame surface. For that, a search for every cell of the computational domain which has a value of $\iota = 1$ is done, and the values found characterize the borders of the flame front. Then, the surface coordinates are integrated radially and axially to compute the area of the flame surface, and this value is further used to approximate the flame front surface area (A). One may note that, since a two dimensional model is used, the isoline $\iota = 1$ is obtained.

1.6 Inverted Conical Flame Steady-State Model

In this section, the analysis of the steady ICF model is developed. The aim is to model the averaged converged state of the flame, and characterize its structure by means of flame properties, and the model boundary values are set in agreement with [9]. Two methods are used to characterize the laminar flame; the first one is based

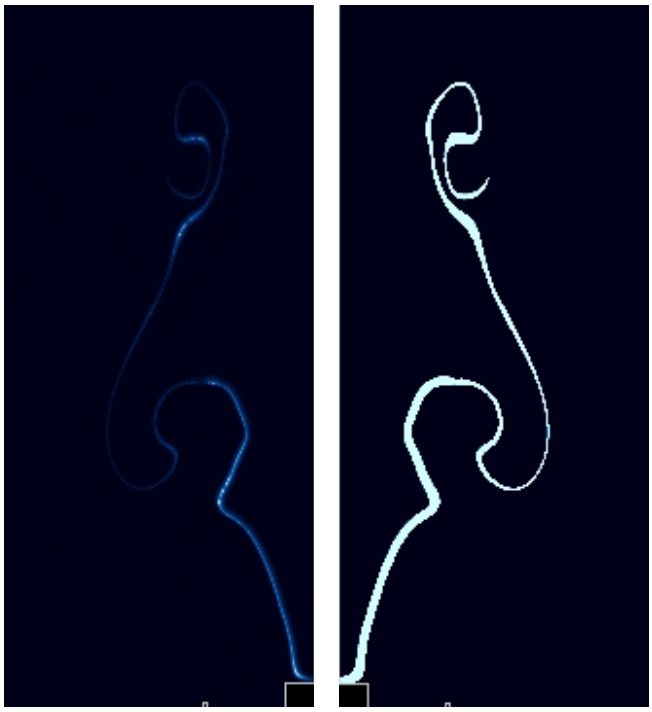


FIGURE 1.11: Comparison of the instantaneous flame front identified with the CH_2 mass fraction (left) and with the binary field ι (right).

on the properties results given by the steady model (section 1.6.1), and the second one is based on the properties averaged values over a number of iterations (section 1.6.2).

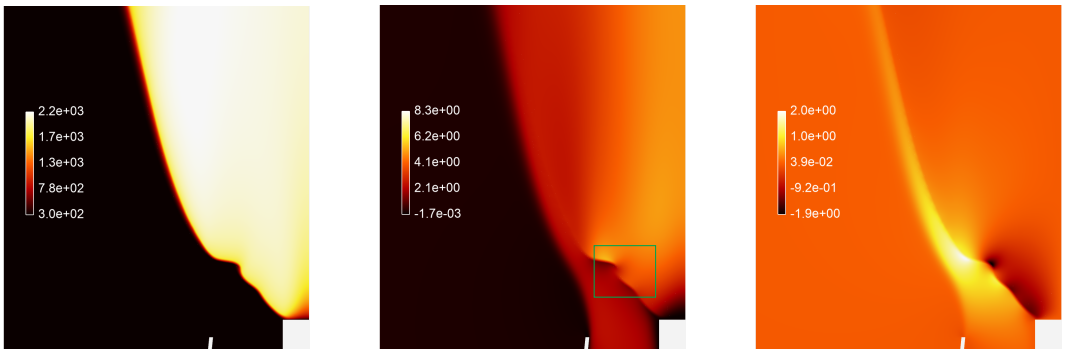
The steady simulation result presented here follow the methodology explained in sections 1.3.1 and 1.4.3. In order to capture the flame in detail, the adaption refinement threshold gradient chosen is of 10 K/m, being adapted at every 25 iterations.

The simulation takes about 30 to 40 days to complete on a Linux-64 SuSE, at ANSYS cluster, Intel(R) Xeon(R) E5-2660 v3, using 108 nodes on 9 machines, with the ignition of the flame.

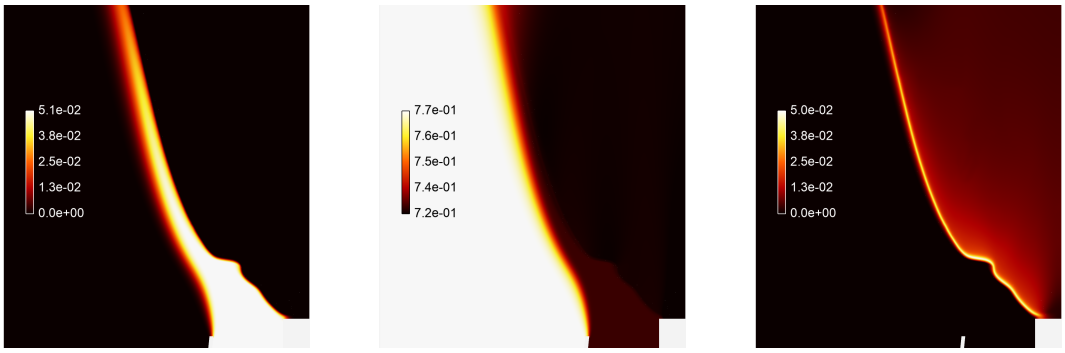
1.6.1 Laminar Flame Structure

In order to discuss the ICF structure, the steady axisymmetric laminar premixed ICF is modeled with a constant volume flow rate of $\dot{\forall}_3 = 180.3\ cm^3/s$, such that $v_d = 2.05\ m/s$, and a methane/air equivalence ratio of $\phi = 0.92$. Under such reactive mixture flow conditions, experimental results shown that a classical premixed laminar flame is anchored at the central rod tip [9]. This flame exhibits an inverted conical shape and gradually consumes the fuel-air mixture. Upon encountering the external air, combustion is depleted. Figure 1.12 presents the model results of a variety of the flame properties, e.g., temperature, axial and radial velocity components and several species mass fractions. The first three figures (Figures 1.12a, 1.12b and 1.12c) exhibit the temperature and velocity components fields, whereas the remaining (Figures 1.12d, 1.12e, 1.12f, 1.12g, 1.12h and 1.12i) show the mass fraction fields of selected chemical species described by the DRM19 kinetic model. These species

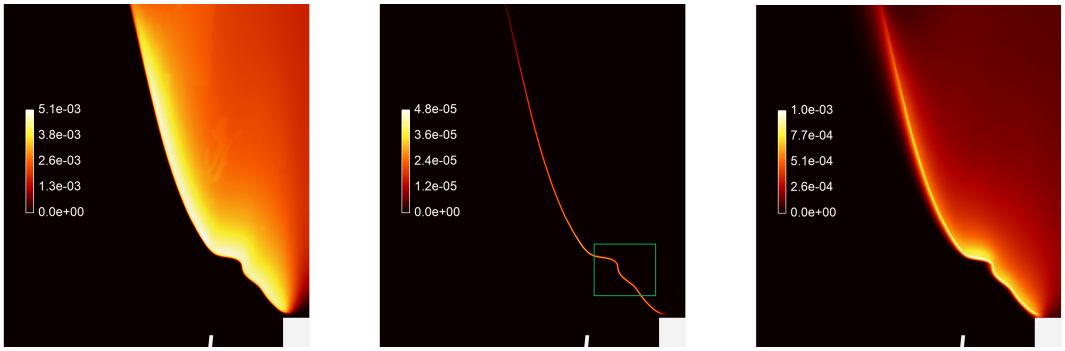
are shown in order to highlight the overall flame structure and, in particular, the multiple length scales that arise within the studied premixed flame.



(A) Temperature (K). (B) Axial Velocity component (m/s). (C) Radial Velocity component (m/s).



(D) CH_4 mass fraction. (E) N_2 mass fraction. (F) CO mass fraction.



(G) OH mass fraction. (H) CH_2 mass fraction. (I) H_2 mass fraction.

FIGURE 1.12: Structure of the laminar premixed inverted conical flame, with a volume flow rate of $\dot{\forall}_d = 180.3\ cm^3/s$ and a methane/air equivalence ratio of $\phi = 0.92$ [36].

The shape of the flame front, when characterized by the temperature, which is anchored at the centered bluff body, exhibits an open form, with a distinct conical shape as depicted on Figure 1.12a. At figure, the maximum temperature of $2,200\ K$, is consistent with the flame adiabatic temperature ($T_{ad} = 2,200\ K$) determined in section 1.2.2. One may note that the temperature at the top of the rod is constant and equal to the ambient temperature ($T_\infty = 300\ K$). This value is chosen because, after a study of the impact of varying the boundary condition at the top of the rod, using different temperature values, it was concluded that the heating of the rod, caused by the flame, does not affect the flame anchor point nor its angle with respect to the incoming flow.

Figures 1.12b and 1.12c underscore the inverted conical shape of the flame, since the axial component of the velocity varies along the flame front, being approximately $v_z = 2.05\ m/s$ upstream the flame front. Due to thermal expansion, it increases immediately downstream the flame front, and the radial component increases in the region immediately upstream the flame front.

Concerning the mass fraction of CH_4, on Figure 1.12d, since there is ambient air flowing in the external region of the mixture feed tube, at the side of the flame that is farther away from the symmetry axis, the fuel air mixture is progressively diluted by the ambient air, whereas it is consumed by the combustion reactions when it is closer to the symmetry axis. Figure 1.12e gives the field of N_2 mass fraction, which is present in the air and in the air-fuel mixture, with a mass fractions of $Y_{N_2}^{air} = 0.7899$ and $Y_{N_2}^{mix} = 0.7203$. respectively. Also, farther away from the symmetry axis of the burner, the N_2 mass fraction is the same of the air stream ($Y_{N_2}^{air} = 0.7899$), and as it gets closer to the flame front, the mass fraction decreases due to the presence of CH_4. In the burned gases region, the air-fuel mixture has a mass fraction of N_2 equal to $Y_{N_2}^{mix} = 0.7203$. Downstream the flame front, the N_2 present in the fuel/air mixture is diluted by the burned gases, such that its mass fraction decreases. Moreover, Figure 1.12f exhibits the CO mass fraction, which underscores the shape and the position of the flame front, and gives an approximation of the flame thickness. Indeed, this substance is produced as the reactive region of the flame develops, and decreases downstream the flame front, gradually tending to the equilibrium mass fraction of $Y_{CO} = 0.0038$. One may note that the field of CO gives just an approximation of the flame front thickness, since this substance is not completely produced and consumed the combustion region, mixing and reacting with other burned gases downstream the flame, which gives a thickness measurement larger than other representations.

Figure 1.12g depicts the field of OH mass fraction, which is produced in the reaction region and thus, is also a possible identifier for the position and shape of the flame front. Figure 1.12h shows the field of CH_2 mass fraction, that is an species produced and consumed within the combustion region, hence giving a sharp representation of the flame thickness. Finally, Figure 1.12i shows the field of H_2 mass fraction, which is produced in the combustion and part of it is consumed in the reactive region. The model results indicates a flame thickness of approximately 130 μm, measure obtained with the CH_2 mass fraction field and Fluent scaled rule. This flame thickness value agrees with the size of 120 μm presented at section 1.2.2, presenting an error of 8.34 %.

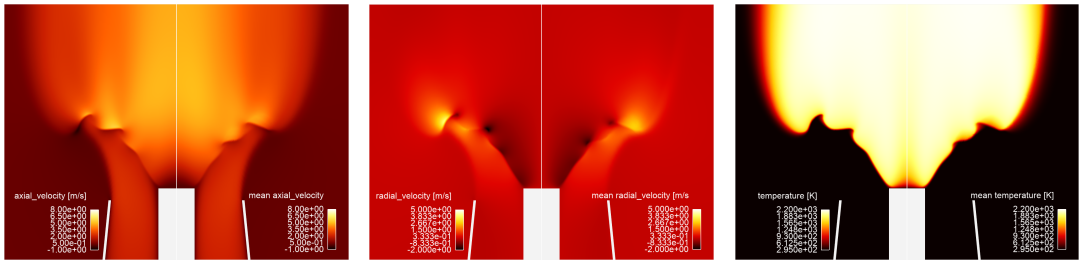
On a global view, all the properties presented on Figure 1.12 present a V-shape, associated to the flame anchored in the central rod, but also, some wrinkles arise along the flame front. These wrinkles, underscored by the squares green marks on Figures 1.12b and 1.12h, represent a flame inherent instability. Indeed, the analysis of the development of some flame properties, which are not shown here for the sake of brevity, show that the wrinkles at the flame front actually tend to move as the iterations proceed. This movement never tends to a permanent state or an strict convergence, but oscillates over a pseudo-transient state point. One may note that this effect could also be caused by computation error, and further research should be developed over the topic.

The previous analysis illustrates the various length scales that results of choosing a kinetic model that accounts for different species and the importance of the adaptive mesh. Indeed, the above discussed chemical species results exhibit different spatial scales, which have been accounted for by the chemical reactions represented by the DRM19 chemical kinetic model. One may also note that the the well resolved flame

results, specially the flame front, have been achieved thanks to the adaptive mesh procedure, which enables the refinement of the mesh from a size of 100 μm to a minimum size at the flame region (5 μm), as discussed in Sections 1.4.4 and 2.2. This mesh size is able to capture the flame scales since it is a mesh $\approx$ 25 times smaller than the flame thickness.

1.6.2 Averaged Laminar Flame Structure

Willing to obtain a better approximation of the ICF in its statistical steady state, the ensemble average of the results is computed, in belief that this average might have a convergent behavior. Figure 1.13 gives the comparison between a steady and the ensemble averaged results, for the axial and radial velocity components, and temperature, for the same model previously shown. The purpose here is to illustrate the effect of ensemble averaging on the results. Each of these contours plots exhibit a steady result on the left, and the ensemble averaged result — over 1000 iterations — on the right side.



(A) Axial velocity component $[m/s]$. (B) Radial velocity component $[m/s]$. (C) Temperature $[K]$.

FIGURE 1.13: Comparison of the flame front structure between Fluent and its average: fields of velocity components and temperature, for two different fuel/air mixture flow rates. Fluent steady field on the left and ensemble average on the right side, for $\dot{\forall}_3 = 180\ cm^3/s$. [36]

On Figure 1.13a, the axial velocity component (left side) and its ensemble average (right side) are presented. These figures show that the average flame front tip, i.e., where the fuel/air mixes with the ambient air, is smeared when compared to the steady field. Indeed, the wrinkles associated to this region are smaller and smoother than those of the steady field, shown at the left side of Figure 1.13a. On Figure 1.13b, a similar behavior is seen. The radial velocity component presents a rather abrupt change of value on steady field, whereas the averaging has an smoothing effect, rendering the wrinkles weaker and smaller. The temperature fields, on Figure 1.13c, underscores that these wrinkles at the flame front tip computed by ensemble averaging the results become smother than those encountered on steady results. The temperature field also highlights that, even though these wrinkles at the flame tip are smeared by the averaging procedure, the flame front still preserves the overall characteristic behavior at the reactive region, such as its anchor point at the bluff-body, the flame front position, shape and length.

The results given on Figure 1.13 indicate that the adopted averaging procedure enables a smoother approximation of the ICF equilibrium state when a qualitative image comparison is performed with the experimental results [9] presented on Figure 1.14. It should be stressed that the flame photograph shown on Figure 1.14 exhibits the natural flame luminosity, which could be associated to CH^* radicals. Such a chemical species is not presented at the DRM19 chemical mechanism, therefore,

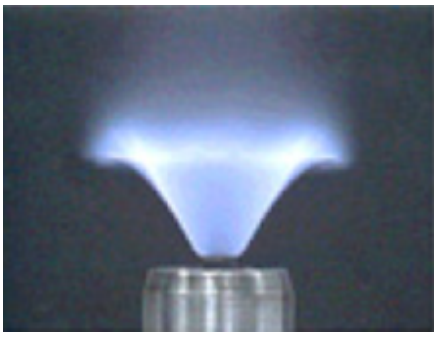


FIGURE 1.14: Experimental steady inverted conical flame, with equivalent ratio $\phi = 0.92$ and nominal volume flow rate $\dot{\forall}_d = 180$ cm^3/s [9].

a qualitative comparison is possible only. These examples illustrate the importance and capacity of computing the average of CFD steady results, ensuring that the obtained model result represents the long term behavior of a system.

1.7 Synthesis

The steady modeling of the inverted conical flame presented in this work, developed with Fluent 2019/2020, computing such complex reactive system enables the study of a diverse quantity of species by modeling the chemical of the system with skeletal kinetic models. One may note that the ICF modeling enables to delve in to the mechanics of flames, thorough an analysis of different physical properties, such as miscellaneous reactive substances from the combustion process (i.e., CH_2, OH and H_2), which can not be achieved experimentally.

However, modeling the steady ICF remains a difficult challenge, since the flame does not tend to a equilibrium state. The ICF flame setup is highly sensible, since the model does not converge to a equilibrium state, but oscillates around a pseudo-steady state point. Indeed, the ICF model presents a better approximation of the steady behavior when the ensemble average of the steady results is computed, but convergence to such a state is still not ensured. To further understand this oscillatory behavior of the steady flame, the modeling of the non forced dynamic ICF, under the same set up of the steady model, is the subject of study of the next chapter.

Moreover, the primary steady model of the ICF enables the use of the developed flame as a base case to initialize other simulations, either steady or dynamic, of the flame. Such initialization remarkably decreases the burden linked to the ignition process of the ICF, which takes a month to fully develop. Such model presented in this chapter represents significant advance on the study of combustion, since it yields a full characterization of reactive flows. However, this kind of model has a large inherent cost, that is expressed on the large amount of time required to solve complex physical system, such that its research and application of other type of models is still envisioned.

Chapter 2

Unsteady Inverted Conical Flame and Thermo-acoustic Coupling

Ce chapitre s'intéresse au comportement dynamique de la flamme conique inversée a travers l'étude de simulations du modèle presenté dans le chapitre précédent. Nous évaluons, dans un premier temps, l'impact de l'adaptation de maillage sur la qualité de la solution numérique, en particulier sur la présence d'instabilité auto-entretenues. Puis, nous proposons une caractérisation du comportement dynamique naturel de la flamme, en particulier des variables d'intérêts suivantes : températures, fraction massique de OH, et surface de flamme. Enfin, nous étudions la réponse de la flamme à des perturbations sinusoïdales de la vitesse d'entrée du mélange en balayant une gamme de fréquence, ce qui nous permet le calcul de la fonction de transfert de la flamme.

2.1 Introduction

Combustion and acoustic coupling can lead to severe dysfunction in a variety of combustion system including gas turbines combustors. The combustion interactions with flow perturbations may lead to unstable behavior that cause structural vibrations and high heat flux to the engine walls, regularly leading to failure[43]. Laminar premixed inverted conical flames (ICF) are combustion systems that feature instability phenomena with a rather simple flow field framework when compared to complex combustion systems [60]. Accordingly, based on experimental studies developed on these flames [9], [10], focusing on the characterization of the flame response due to incoming excitation, we investigate here the self-sustained instabilites of an ICF, as well as its response to forcing.

More specifically, the thermo-acoustic instabilities characterizing combustion processes are caused by flow velocity fluctuations that couple with the flame and generate thermo-acoustic instabilities. These phenomena may be studied by exciting the flame with forced velocity oscillations at a specific frequency and magnitude [9]. A synthetic description of the flame response to velocity fluctuation is the Flame Describing Function, which can be experimentally characterized [9], [10] and can be used to predict instabilities.

Standard laminar conical flame dynamical instabilities have been extensively studied [7], [8], [61], [62]. The flame front dynamics of a inverted conical flame has been analyzed for a confined flame [61], and the non-linear response of ducted flames anchored on a central rod has also been addressed [62]. However, to the best of the authors knowledge, few modeling studies exist concerning laminar premixed inverted conical flames anchored on a bluff-body [9], [36]. The studied flame has been shown to be susceptible to thermo-acoustic instabilities, mainly driven by

flame convective vorticity mode [9]. Such instability is seen at the vicinity of tip of the flame on Figure 1.1, and the coupling of these with combustion is the subject of this chapter.

The characterization of the response of flames to incoming excitation is an active research topic. For instance, the analytical study of a model of a transversely forced flame on a two-dimensional Bunsen flame under transverse mean flow underscored the influence of several effects, such as frequency, transverse mean flow velocity and vertical mean flow velocity on the Flame Transfer Functions (FTFs) [63]. Studies of laminar premixed V-flame forced with high frequency showed that the acoustic transverse standing wave response depends on the acoustic condition [64], having two response patterns; pairing process where multiple-vortex interact in the jet outer layer, or a helical mode in the inner layer behind the rod. The analysis of the dynamic response of premixed flames was also experimentally studied with chemiluminescence cross-correlation maps [12], [65]. Moreover, the results of the first work [65] showed consistency with physical interpretation proposed for the cross-correlation maps, confirming its potential for diagnosing the effective contribution of different flame regions to the global dynamic response [65], whereas the results of the second work [12] showed the dynamics of the flame leading edge in a laminar premixed flame stabilized on a bluff body in a channel [12]. The identification of FTFs in the presence of intrinsic thermoacoustic feedback and noise by applying LES and system identification approach was used to model turbulent reacting flow under broadband excitation [66]. A coupled FDF with a neural network thermoacoustic approach, over an LES model of a turbulent and partially premixed flame led to the prediction of combustion instability limit cycle oscillations [67]. By applying steady flamelet model and the flamelet/progress variable approach, a computational analysis of the coupling of transient flame dynamics, such as the local extinction and the thermoacoustic instability, in self-excited resonance combustor, enabled the identification of mechanisms of thermoacoustic instability [6]. Recent studies on the FTF in premixed flame dynamics analyzed the significant impact of the flame geometry into its acoustic response [11], and modeled the premixed flame linear dynamics in terms of time delays [68], thus characterizing an acoustically compact flame by its impulse response, enabling for the development or control techniques in the combustion and thermoacoustic domain.

The general resonant coupling mechanism of combustion and acoustics is represented by the scheme on Figure 2.1. The flames dynamic response to an incoming upstream velocity fluctuations (v') present flame speed and burning area perturbations, thus causing heat release rate oscillations which then cause velocity fluctuation on the flow. This resulting heat release rate fluctuations (Q') induces unsteady gas expansion which, in return, leads to pressure acoustic oscillations (P'). The pressure fluctuations travel along the domain, including upstream the burner, linking the the pressure and velocity fluctuations at the outlet. This flame response due to incoming velocity perturbation is extensively studied with Flame Transfer Function (FTF) analysis, and here a similar study is presented based on previous analysis [43], [69], [70].

In this Chapter, we investigate the dynamic behavior of the ICF by studying simulations of the model presented in the previous Chapter. First, we evaluate the impact of mesh adaptation on the accuracy of the simulations and, in particular, on the presence of self-sustained instabilities. Then, we propose a characterization of the flame natural dynamic behavior in terms of temperature, OH mass fraction and flame surface area. Finally, we study the flame response to sinusoidal perturbations

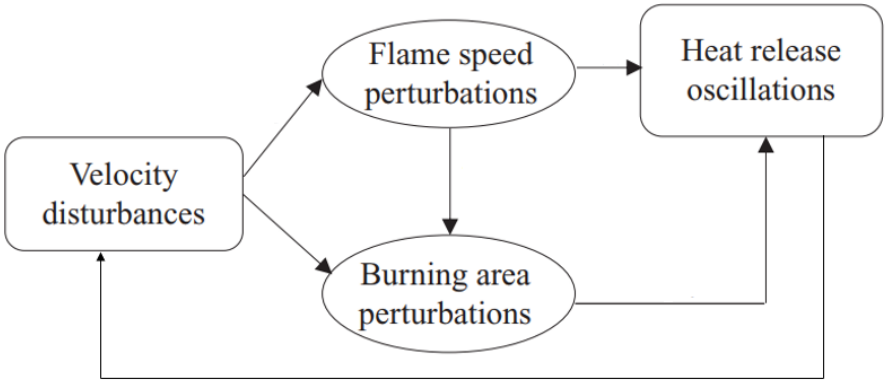


FIGURE 2.1: Resonant coupling mechanisms through which flow velocity oscillations lead to combustion heat release oscillations [71].

of the inlet mixture velocity over a range of frequencies, which enables the computation of the Flame Transfer Function (FTF).

2.2 Mesh Adaption Influence

In this Section, we discuss the impact of the temperature gradient mesh adaption threshold on the accuracy of the dynamic simulations. Wee consider a situation where the flame is excited by an external mean velocity forcing, of the following form

$$v_{mix}(t) = v_d + v_a cos(2\pi f t) = v_d + v', \tag{2.1}$$

where v_d is the nominal fuel/air mean inlet velocity of 2.05 m/s, v_a is the excitation amplitude, and f its frequency in Hz. More specifically, the forced case which is here described has $v_{a,rms} = 0.14\ m/s$ and a frequency ($f = 100\ Hz$). The values are chosen based on the results of [9], which indicate that this set yields the maximum response gain for the inverted conical flame.

The mesh adaption strategy described in Section 1.4.4 comprises two degrees of freedom. Here, the characterization of their impact on the accuracy of the computations is developed by performing four different simulations. These two degrees of freedom are the temperature gradients thresholds for coarsening and refining, respectively. The values used for each simulations are presented in Table 2.1. This particular set of threshold values is chosen to encompass a poorly refined mesh up to an excessively refined mesh. Indeed, a typical value for the laminar flame thickness is $\approx 100\ \mu m$, and the corresponding temperature increase is $1,500\ K$, to which implies a maximum temperature gradient of $\sim 10 \cdot 10^6\ K/m$. Considering that the maximum number of refinement steps is 12, the typical minimum resulting mesh spacing that can be obtained is $0.7\ \mu m$, which is less than the minimum mesh size necessary to modeling the steady state steady state ICF, as discussed in Section 1.2.2. Also, note that the base mesh has $512,612$ nodes in its initial state, which increases as the mesh is adapted.

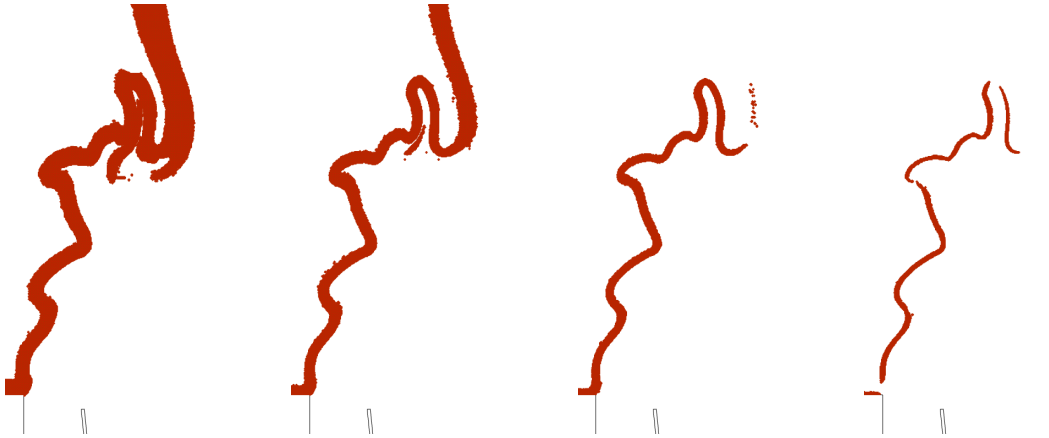
A qualitative appraisal of the adaption strategy on the resulting mesh is achieved by examining Figure 2.2, which shows the refined mesh in red, for one arbitrary instant of the simulation. The refined region span decreases as the temperature gradient refinement threshold increases. The adapted mesh, which is controlled by the

TABLE 2.1: Mesh adaption temperature gradients thresholds influence.

-	Adaption thresholds $[K/m]$		Resulting mesh characteristics		
Case	Refine	Coarse	Added nodes	Wall clock time cost $[days/s]$	Harmonic $[Hz]$ characteristic
1	10	300	162,838	64	40; 100
2	25	400	86,016	21	100
3	50	500	43,332	11	100
4	100	600	23,146	9	100

temperature gradient, has its nodes positioned only at the regions of high temperature gradient, which characterizes the combustion region. The typical thickness of the refined region decreases from $3,100\ \mu m$ to $900\ \mu m$ as the refinement threshold increases from 10 to 100 K/m. Besides this increase of the mesh adapted region, the typical number of mesh points along the flame thickness increases from 2 at the base mesh, to 16 at the most refined mesh. Indeed, the number of added mesh nodes after the first adaption is given in Table 2.1, as well as the wall clock time necessary to compute 1 s of the flame model. The characteristic frequencies encountered at each ICF flame surface fluctuation dynamic response are also are given in Table 2.1.

The sheer influence of the refinement threshold on the computational time is evident in Table 2.1. Halving this threshold from 100 to 50 K/m induces a cost increase of 33%, whereas the subsequent halving doubles the cost. The final threshold variation attempted, i.e., from 25 to 10 K/m corresponds to a three fold increase in the computational cost. Moreover, the increasing wall clock time cost effect is directly linked to the increase of the number of mesh nodes during the simulation, since the smallest refinement gradient of 10 K/m demands the addition of four times more nodes at the first mesh adaption step than when a gradient of 50 K/m is used.



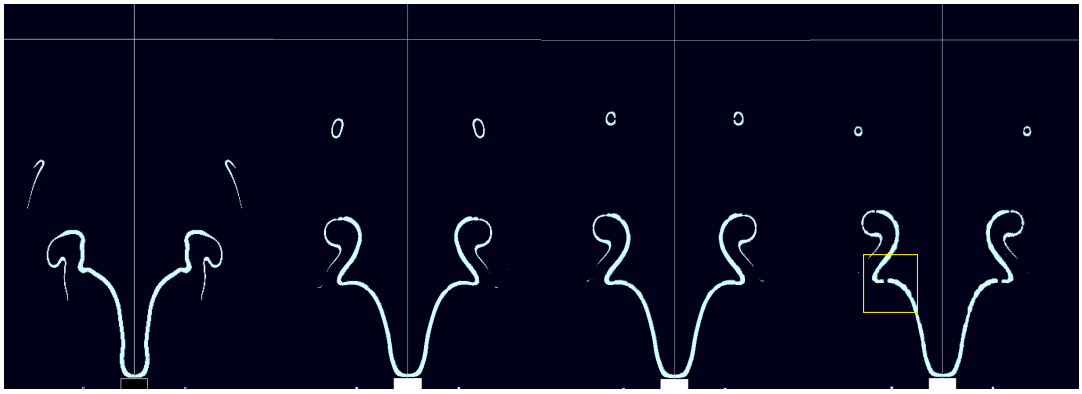
(A) 10 K/m. (B) 25 K/m. (C) 50 K/m. (D) 100 K/m.

FIGURE 2.2: Mesh adaption region for different refinement temperature gradient threshold values.

It is also worth to note that the number of refinement levels is practically constant as the refinement threshold decreases. For instance, the mesh actual number

of levels varies between four and five, for both the coarsest (100 K/m) and the finest (10 K/m) meshes. This consequently impacts on the minimum mesh spacing and thus, on the maximum time step allowed, such that the minimum mesh size decreases from 100 μm at be characteristic mesh to 3.7 μm at the refined mesh at level 5. Nevertheless, the decrease of the mesh temperature refinement gradient threshold leads to an increased computational burden mostly linked to the increase of the size of the region of mesh adaption. Moreover, one must keep in mind that the number of added nodes to the base mesh varies during the simulation, depending of the threshold and the flame dynamics.

To further characterize the mesh adaption influence on the computed ICF, Figure 2.3 depicts the flame front position, at an identical arbitrary instant, but distinct from that of Figure 2.2, using the different thresholds given in Table 2.1. In this figure the flame front is defined as explained in Section 1.5.2, Equation (1.19). Figure 2.3 indicates that the temperature gradient threshold used for mesh refinement yields a similar flame front behavior. Indeed, the flame base exhibits a wide V-shape and the flame tip shows a similar roll-up, which is underscored by comparing Figures 2.3b, 2.3c and 2.3d. Note that when using the largest refinement threshold, 100 K/m, depicted on Figure 2.3d, a few discontinuities along the flame front are seen, as shown by the square yellow mark. These are artifacts of the binarization procedure and do not represent physical behavior, but indicate that such a large refinement threshold is insufficient to describe the flame surface. However, when a temperature gradient refinement threshold of 10 K/m is used, the flame front presents a somewhat different behavior, as depicted on Figure 2.3a. In this particular case, the tighter adaption modifies the flame base shape, tip and roll up behavior, i.e., the flame shows a narrow V-shaped base and a premature rolling up a this specific instant in time. This analysis then, suggests that the adaption spanning from 10 to 50 K/m is capable to describe the overall flame structure, in particular the flame base shape, but some attention must be taken in relation to the impact of using different thresholds.

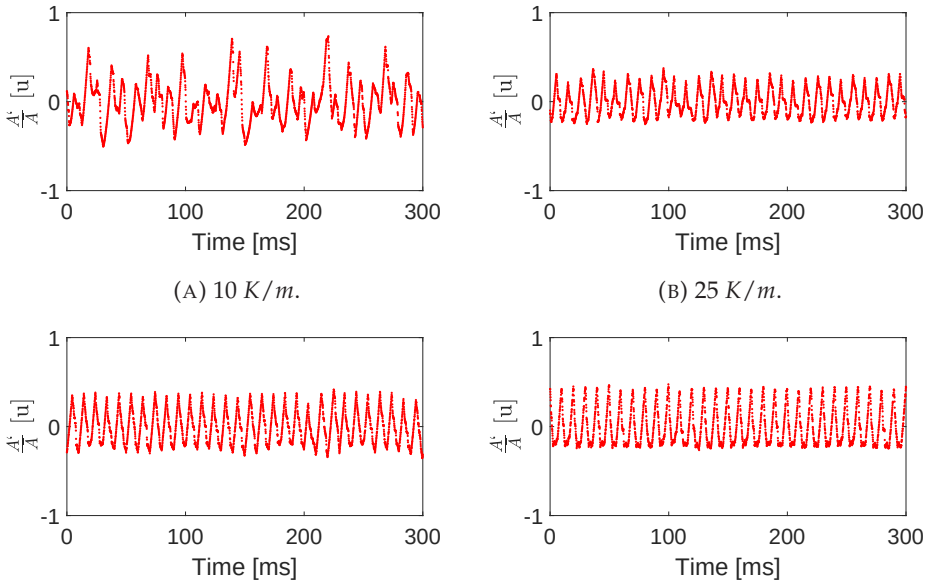


(A) 10 K/m. (B) 25 K/m. (C) 50 K/m. (D) 100 K/m

FIGURE 2.3: Instantaneous of the flame front for different mesh refinement temperature gradient threshold values.

The flame surface area fluctuations, computed as explained in Section 1.5.2, is depicted on Figure 2.4 illustrating the impact of the thresholds on the flame front. In addition, the stronger frequency present on the spectrum of each of the thresholds signals is given in Table 2.1, since the frequency analysis and characterization of the ICF is discussed later in Chapter 2. This figure and Table 2.1 underscore the trade-off between flame surface features representation and the corresponding cost. It is clear that choosing the tighter refinement approach of 10 K/m leads to a richer flame

surface area behavior, but at the expense of a significant computational cost. As the refinement threshold increases, the flame surface variations are certainly less complex. More precisely, for the refinement threshold of 10 K/m, the flame surface fluctuations present a maximum oscillation amplitude of approximately ± 0.5 (Figure 2.4a), and the fluctuation behavior corresponds to two main frequencies of 100 Hz and 40 Hz, the first of which corresponds to the forcing frequency. The smaller frequency (40 Hz) is absent from the flame surface fluctuations observed for the three larger refinement thresholds, which retain the forcing frequency only, with a smaller surface area amplitude, of ± 0.4. Thus, even if the 100 K/m adaption approach has been seen not to reproduce the flame surface details adequately, the overall forcing frequency response is obtained. Note that the flame frequency response and structure is discussed in Section 2.4.



(A) 10 K/m.

(B) 25 K/m.

(C) 50 K/m.

(D) 100 K/m.

FIGURE 2.4: Flame surface area fluctuations results for each of the cases presented in Table 2.1, i.e., different mesh refinement thresholds.

As seen in this Section, the most detailed model is the one with a temperature refinement gradient threshold of 10 K/m. However, as already seen in Table 2.1, three months are necessary to compute 1.5 s of the dynamics of the ICF using a refinement gradient of 10 K/m, which is around six times the time necessary to perform the same computation but using 50 K/m. As a consequence, the choice of the threshold is based on the objective of the simulation. For example, a model with the intention of characterizing the flame complete physics for one scenario, such as species, velocity and temperature, should be simulated with the finer mesh refinement threshold. However, a model which wishes to study the impact of several parametric variables into the flame dynamic response, should be simulated with a larger threshold, since the cost and time to simulate the impact of varying parameters is reduced. The trade-off between cost and precision is an important point that should be taken into account for every combustion process simulated with adaptive mesh refinement.

2.3 Flame dynamics

To anticipate potential instabilities due to thermo-acoustic coupling, the model described in Chapter 1 is used to compute the dynamical behavior of the flame. The dynamics is studied under both a constant inlet mixture velocity and a sinusoidal forcing, given by Equation (2.1). The forcing frequency, f, varies between 50 Hz and 300 Hz, whereas the magnitude is constant $v_a = 0.14$ m/s. These values are based on the experimental study [9], which indicate that higher frequencies are entirely filtered by the flame dynamics. In Section 2.4, the flame behavior is characterized in the two following ways

- A qualitative description of the evolution of the fields of various physical quantities, in particular those identifying the flame front;
- A quantitative evaluation of the heat release harmonics, in the form of a Flame Transfer Function, discussed in the next Section.

2.3.1 Flame Transfer Function (FTF)

Although flames dynamics are the result of complex distributed phenomena, acoustically compact flames can be considered pointwise with respect to the environment they interact with. In this regard, it is reasonable to try and approximate their behavior using an input-output dynamical model. This has been the object of a number of contributions [7], [8], [43], [72], [73] which focus on experimental identification of the heat release harmonic response to incoming velocity fluctuations. The investigation of nonlinear models is differed to Chapter 3, and the focus here is on linear ones, in particular the so-called Flame Transfer Function (FTF). The FTF $\mathcal{F}$ is defined in the frequency domain as follows

$$\mathcal{F}(\omega) = \frac{\dot{Q}'(\omega)/\bar{\dot{Q}}}{v'(\omega)/\bar{v}}, \tag{2.2}$$

where $\dot{Q}$ denotes heat release rate, v is the mixture inlet velocity, $\bar{\cdot}$ denotes steady-state values while $\cdot'$ denotes perturbations around the steady-state, i.e. $v = \bar{v} + v'$. For premixed combustion, such as that studied here, the heat release fluctuations ($\dot{Q}'$) are directly proportional to the flame surface area fluctuation (A'), and thus to the flame chemilumonescence [74], [75]. In this work, the flame surface area is used to compute the FTF, such that it is now defined as:

$$\mathcal{F}(\omega) = \frac{A'(\omega)/\bar{A}}{v'(\omega)/\bar{v}}. \tag{2.3}$$

One should note that such an approximation is similar to the one performed in the experiments, where CH* chemiluminescence is assumed to represent the heat release rate [9]. The FTF may also be expressed in terms of gain ($G = |\mathcal{F}|$) and phase ($\gamma = arg(\mathcal{F})$), such that the gain reflects the magnitude flame response and the phase defines the lag between the velocity and flame surface area fluctuation, i.e,

$$\mathcal{F}(\omega) = G(\omega)e^{i\gamma(\omega)}. \tag{2.4}$$

2.3.2 Computation of the Flame Transfer Function

Since the dynamics of the flame are inherently nonlinear, several approximations must be made in order to compute the FTF. The following process is made here

1. Fix the frequency f of the excitation.
2. Compute approximate steady-state values $\bar{v}$, $\bar{A}$.
3. Apply a bandpass filter of bandwith Δf around f to the output A'.
4. Compute the gain and the phase of the FTF.

Each of these steps is now briefly detailed.

Excitation frequencies Several simulations are performed with mono-frequency excitation signals, with frequencies ranging from 50 to 300 Hz. Other classical options for system identification include exciting the system with broadband signals or chirps. Since the flame response is nonlinear, its characteristics in a certain frequency band cannot be entirely attributed to the excitation in the same band. For this reason, broadband signals are ill-suited to FTF identification. Besides, to avoid transient effects, chirp signals are avoided as well.

Steady-state values As detailed in Section 1.6, the equilibrium of the flame is difficult to compute. As a consequence, the steady-state $\bar{\cdot}$ values in (2.3) are unknown. Averaging the signals over several periods of the excitation signal is thus used to approximate $\bar{\cdot}$.

Bandpass filter As mentioned above, the flame has a nonlinear response to sinusoidal excitation. This point is illustrated on Figure 2.5 where the Fourier spectrum of the heat release corresponding to a mono-frequent excitation at $f = 100$ Hz is depicted. The frequency components are isolated around the excitation frequency

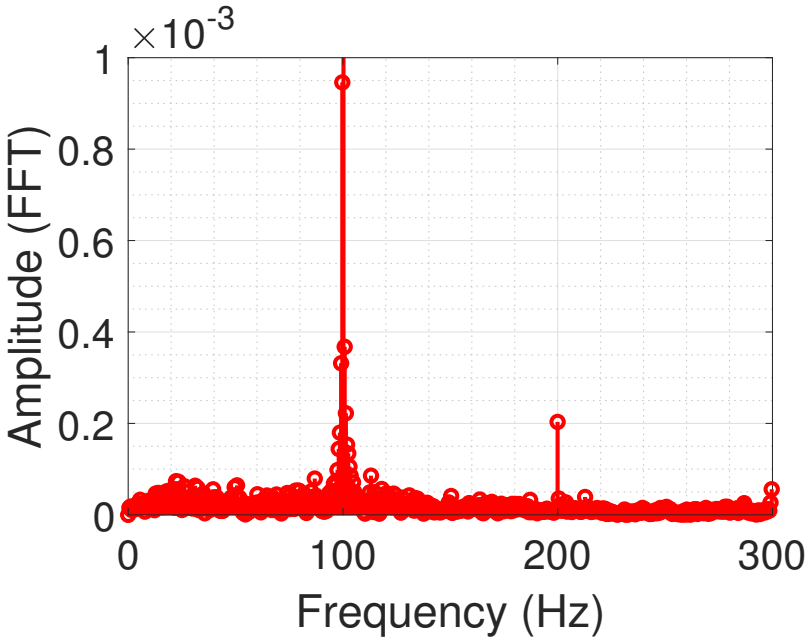


FIGURE 2.5: Spectrum of the heat release response for a mono-frequent excitation at $f = 100$ Hz.

by applying a square window filter with a 10 Hz bandwidth on the Discrete Fourier Transform of the response.

Gain and phase computation After filtering, the gain of the FTF is computed as

$$G = \frac{|\tilde{A}'|/\bar{A}}{|\tilde{v}'|/\bar{v}}, \tag{2.5}$$

where $|A'|$ and $|v'|$ are computed by the RMS in the frequency domain as follows

$$\begin{aligned} \tilde{A}' &= \sqrt{\sum_{i=1}^{N} \left| \frac{\tilde{A}'_i}{N} \right|^2}, \\ \tilde{v}' &= \sqrt{\sum_{i=1}^{N} \left| \frac{\tilde{v}'_i}{N} \right|^2}, \end{aligned} \tag{2.6}$$

where $\tilde{A}'_i$ (resp. $\tilde{v}'_i$), $i = 1, .., N$ are the Discrete Fourier Transform (DFT) coefficients of the filtered flame surface area (resp. velocity).

2.4 Results and Discussion

In this section, the description and discussion of the numerical simulations corresponding to the non forced and excited scenarios are given, respectively in Sections 2.4.1 and 2.4.2.

All the simulation presented here were developed in parallel, with Linux-64 SuSE, Intel(R) Xeon(R), at Ansys cluster, using between 100 to 180 nodes to run Fluent.

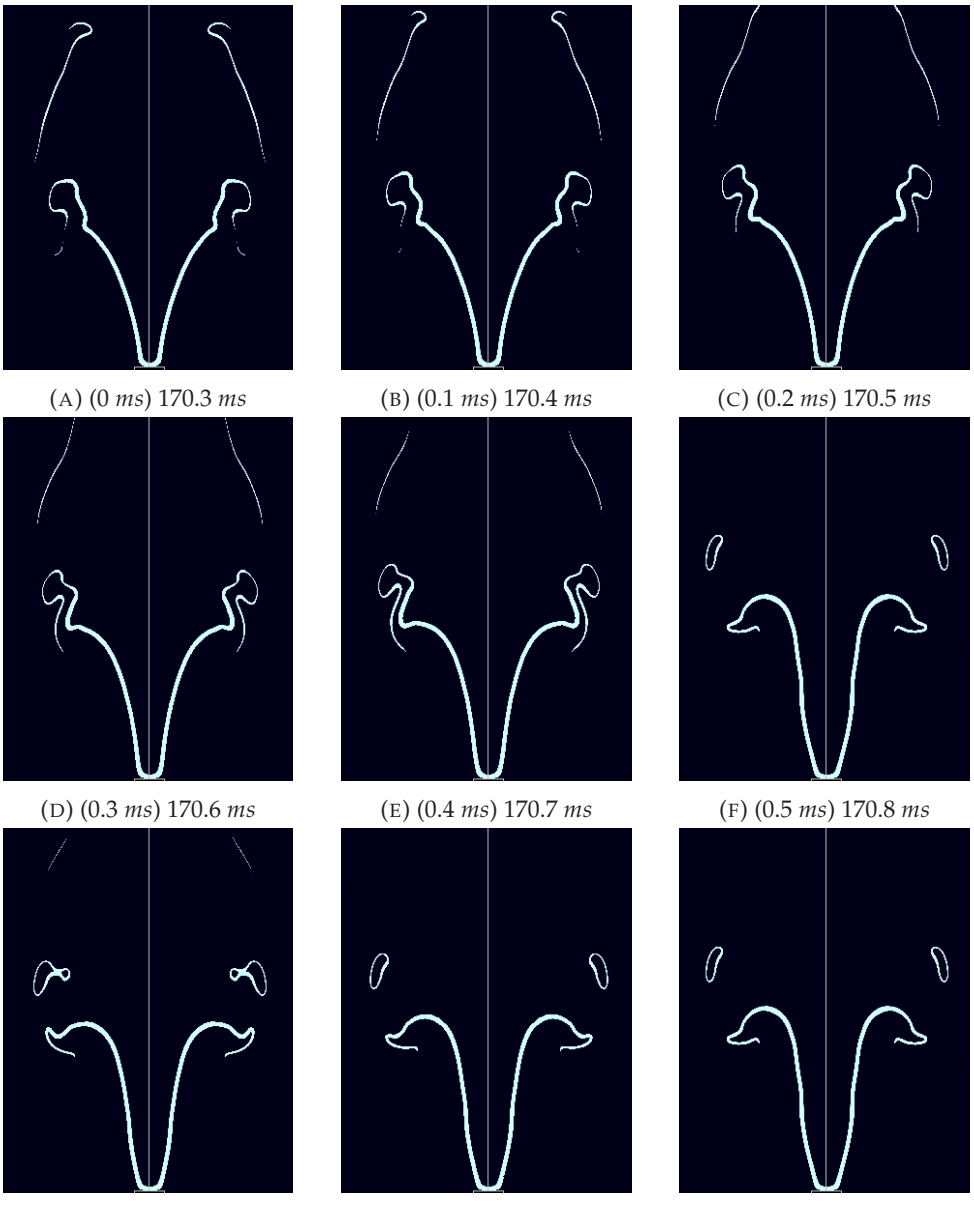
2.4.1 Unforced ICF

All the simulation presented here were developed with Fluent 2019R2/2020R1. The analysis of the dynamic of the unforced inverted conical flame is first presented. The characterization of the flame structure, as well as the surface area and pressure fluctuations in such a naturally unsteady case is developed. Since a single unforced case is analyzed, and in order to capture the flame dynamics in detail, the adaption refinement threshold gradient chosen is of 10 K/m.

Overall flame structures

The unsteady flame model is able to describe several instantaneous flow properties, since the used chemical kinetics model involves diverse species. Here, in order to assess the ICF unforced unsteady behavior, the flame front position is depicted using the field of α defined by Equation (1.19). Accordingly, Figure 2.6 shows the instantaneous flame front at different times, regularly spaced by 100 μs, during 0.8 ms. This particular set of images is chosen such that a full cycle of natural flame oscillation is presented. For the sake of the flame structure discussion, the flame is divided in three different regions, from upstream to downstream. The flame surface exhibits distinct behaviors at each of these three regions; one at the the vicinity of the central rod stabilization, one at the second third, where the roll up begins, and the last at the freely standing flame tip, influenced by the flame pinch off. Indeed, at the first of these regions the flame surface area is nearly invariant in time, whereas at the second and third regions an unsteady behavior arises. In particular, on Figure 2.6 the ICF initially exhibits an increasing flame surface area, Figures 2.6a-2.6e, due to

the rolling up of the flame tip. However, on Figure 2.6f, the rolled up flame front collapses, leading to a fast annihilation of the flame surface. This phenomena, in turn, leads to fluctuations of surface area, associated to the rapid consumption of the fresh reactant pocket, as seen on Figures 2.6f-2.6i. Even if this annihilation is cyclic, it is worth to note that that this cycle period is not deterministic and exhibits some degree of randomness, as it will be later discussed.



(A) (0 *ms*) 170.3 *ms* (B) (0.1 *ms*) 170.4 *ms* (C) (0.2 *ms*) 170.5 *ms*

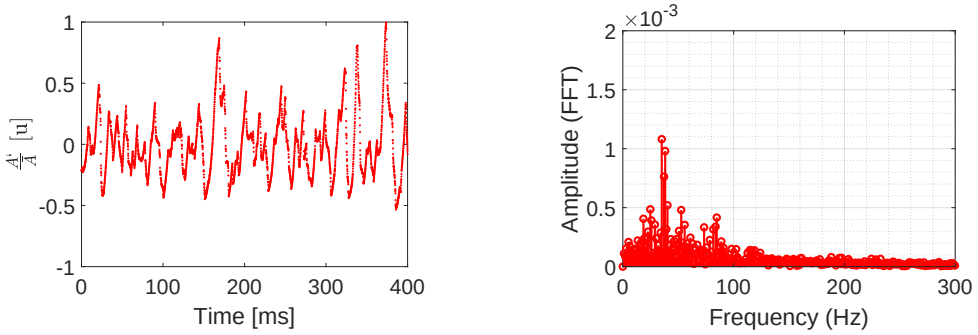
(D) (0.3 *ms*) 170.6 *ms* (E) (0.4 *ms*) 170.7 *ms* (F) (0.5 *ms*) 170.8 *ms*

(G) (0.6 *ms*) 170.9 *ms* (H) (0.7 *ms*) 171.0 *ms* (I) (0.8 *ms*) 171.1 *ms*

FIGURE 2.6: Unforced flame front position at different equally spaced (by 100 μs) instants in time.

In order to further characterize the unforced flame behavior, the flame surface area $A(t)$ is computed as described in Section 1.5.2 and the relative fluctuations $A'/\bar{A}$, are plotted on Figure 2.7a, as well as their frequency spectrum on Figure 2.7b. The flame surface oscillating behavior is clearly seen. The large ($\pm$50%) fluctuations of the flame surface area underscore that at some instants the flame front has an abrupt reduction which are preceded by a relatively slower increase. These abrupt periodic variations, are indeed directly linked with the annihilation of the

flame front surface, seen on Figure 2.6. Moreover, the maximum observed when $170 \leq t \leq 180$ ms at the flame surface fluctuation (Figure 2.7a), lies at the exact moment when the flame surface annihilation begins. Figure 2.7b shows that the corresponding spectrum features a distinct peak at the frequency of 35 Hz. This suggests that the flame behavior features self-excited oscillations at this frequency. This further illustrates the finding that the ICF does not have an equilibrium steady state, or has an unstable one, as discussed in Section 1.6.



(A) Relative flame surface area fluctuation.

(B) FFT.

FIGURE 2.7: Unforced ICF surface area response history and frequency behavior.

The spectrogram of the non forced ICF surface area fluctuation, shown on figure 2.8, agrees with the FFT result, where a broadband low frequency response is seen. However, on this figure, the characteristic frequency fluctuates along the time, having a maximum energy clearly oscillating around 35 Hz. For instance, when time ≤ 200 ms, the frequencies that have more energy are found between 20 and 35 Hz. Later in time, when $300 \leq$ time ≤ 400 ms, tree frequencies are remarked; $20, 35$ and 55 Hz. Subsequently, the behavior mainly due to a frequency of 35 Hz is seen. Such flame response seems to be inherent of the flame unforced dynamic. However, due to the costs linked to running such simulations, more extensive analysis is yet not possible, but it is definitely a perspective for the research on self-excited flames.

The complete Fourier spectrum of the pressure data obtained for the ICF is given on Figure 2.9, and it presents a high energy concentrated into a high frequency ($f = 2000$ Hz). This high frequency perturbation is actually a computational effect created by the mesh adaption, that is updated at every 500 μs, thus having a characteristic frequency of 2000 Hz. Moreover, this non-physical frequency does not seem to interfere with the flame dynamic behavior, since no significant energy is found in this frequency range for other physical quantities, such as the flame surface area. A low-pass filter with a cut-off frequency of 1000 Hz is therefore applied to the pressure signal.

Figure 2.10a depicts the Fourier spectrum of pressure data obtained at point O (Table 1.3), for a frequency range $f \in [0, 300]$ Hz. Figure 2.7b depicts the corresponding reconstructed response in time. It should be stressed that this result is similar for all the points of data extraction presented in Table 1.3 and, for the sake of brevity, only the results for point O are given. Indeed, all the pressure fluctuation curves are superimposed, inducing that the ICF response modeled in this work is acoustically compact [68].

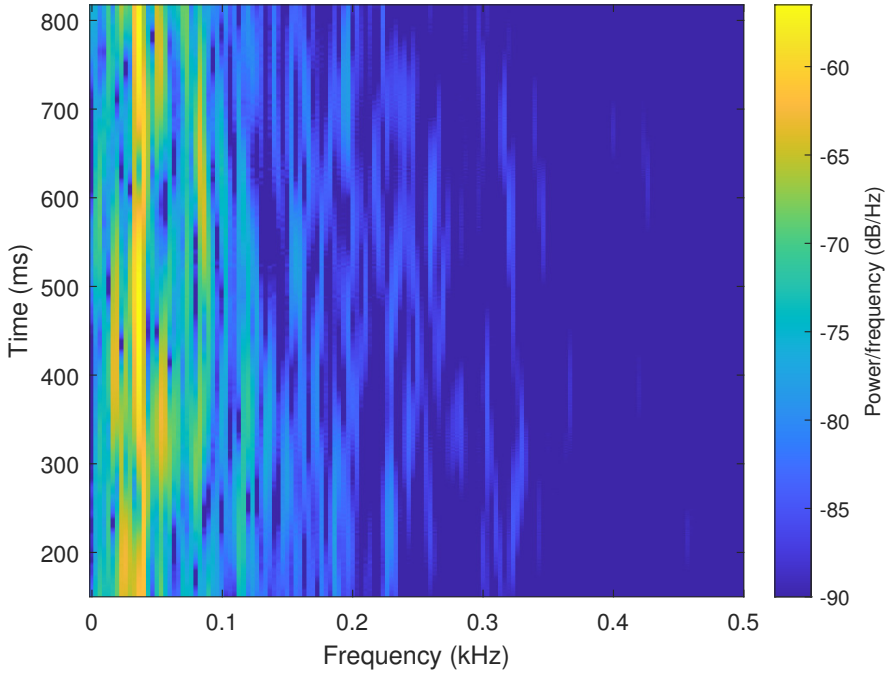


FIGURE 2.8: Spectogram of the ICF surface area fluctuation, for the final 1 s of simulation.

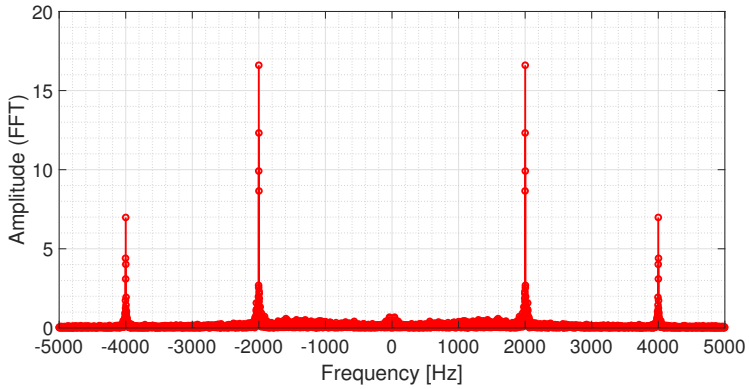
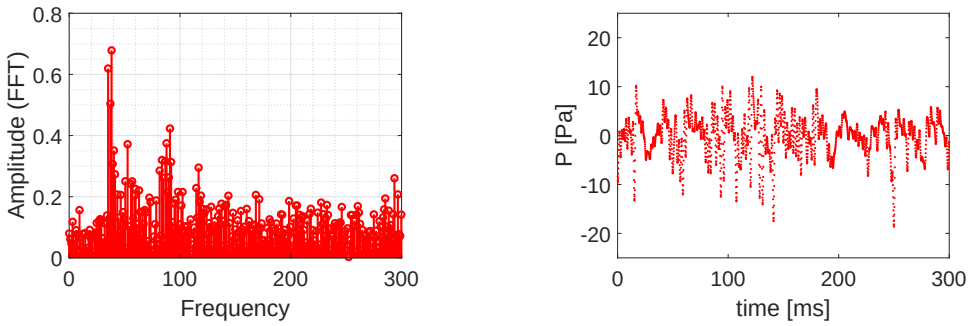


FIGURE 2.9: Complete pressure history frequency analysis for the data extracted at point O (—), presented in Table 1.3.

Fluctuating Temperature and OH Mass Fraction

Here, an unsteady analysis of temperature (T) and OH mass fraction (Y_{OH}) evolution in a period of time is presented.The analysis of the temperature, enables the identification of the position of the flame front since, at this region, the temperature increases from ambient $T_\infty = 300\ K$ to the flame adiabatic temperature $T_{ad} = 2,200\ K$. On the chemical kinetic side, the analysis of OH mass fraction, an intermediate species on the combustion process, enables an alternative characterization of the flame front, since this property has its higher concentration on the reactive region, but non-zero values at equilibrium. This methodology is inspired by the experimental study [9], where the flame front is characterized based on the CH^* radical.

Accordingly, Figure 2.11 depicts the evolution of temperature and OH mass fraction in time, for various probes locations, at points points G (—), I (⊓⊔), M (⊖)



(A) Pressure FFT result.

(B) Reconstructed pressure data.

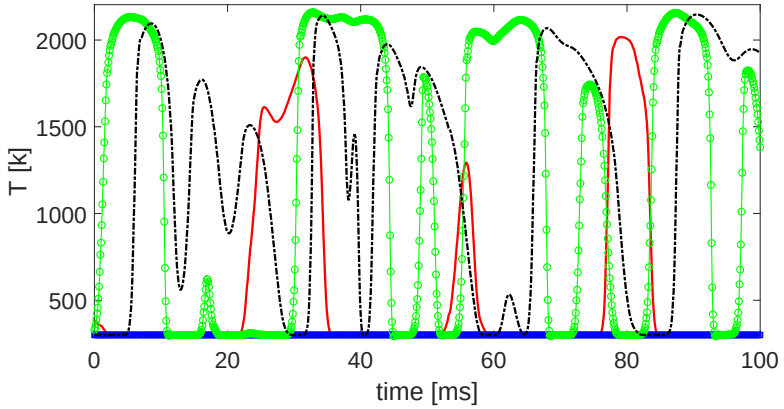
FIGURE 2.10: Unforced ICF pressure history frequency analysis and signal reconstruction. The depicted results are relative to the data extracted at point O (—), presented in Table 1.3.

and O (- · -) from Table 1.3. The unsteady motion of the flame front presents enough temporal resolution to adequately capture the passage of fresh to burned gases, i.e., when the temperature varies from $T = 300$ to $2,200\ K$. Meanwhile, the flame fluctuates across a given position of measurement. Indeed, Figure 2.11a shows that the temperature varies between $T_\infty = 300\ K$ at the fresh gases to $T_{ad} = 2,200\ K$ at the burned gases and vice-versa, e.g., when $30 \leq t \leq 42\ ms$ for point M (⊖—⊖), which also indicates the passage of the flame front over the probe point, where the temperature presents fast variations. The evolution depicted on Figure 2.11 gives an accurate temporal and spatial characterization of the ICF. The time step $100\ \mu s$ is adequate in regard to the time scale of the temperature dynamics, particularly when a high gradient is characteristic of the passage from burned to fresh gases, such as at the period of $2\ ms$. Therefore, the model is able to capture even the intermediary states of the flame, i.e., within the flame front thickness.

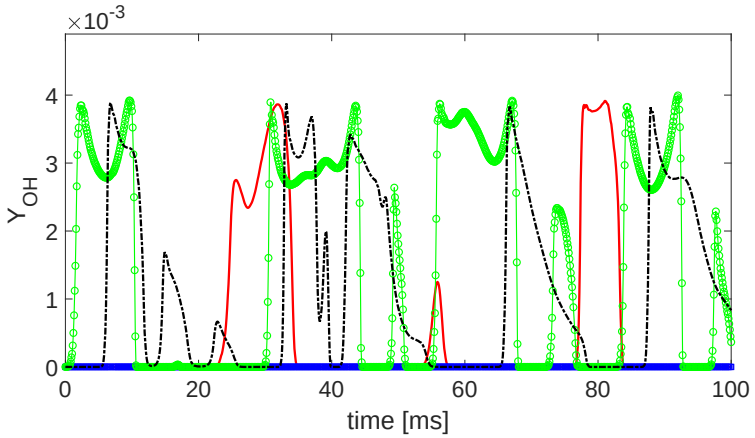
Similarly, the evolution of the OH mass fraction at point M features complete passages of the flame front, characterized by a non-monotonic behavior, whereas points G and O show incomplete passages. Point I (⊓—⊓) has a constantly zero OH mass fraction, thus being positioned in the fresh gases region.

Moreover, Figure 2.11a features incomplete passages of the flame front over the point M, e.g. around $t = 17\ ms$ or $t = 50\ ms$, since the temperature curve has extremes in intermediate stages of the temperature ($T_\infty < T < T_{ad}$). Such dynamic characterization of the flame front is indeed distinct from other methodologies, such as the level-set technique which consists in modeling the flame surface with a Damköhler value that tends to infinity, thus separating the burned from the fresh gases [76]. The temperature extracted with points G (—) and O (- · -) exhibits similar trends, since both temperatures varies in between $T_\infty < T < T_{ad}$ over the time. However, for both probe points, the temperature does not fully increases across the flame surface, hence not reaching the burned gases region and staying at intermediate values most of the time.

Furthermore, when the burned gases are over the measurement point, e.g., point M when $30 \leq t \leq 50\ ms$ on Figure 2.11a, the temperature presents a nearly steady behavior, around the adiabatic flame temperature of $2,200\ K$, until the flame crosses the probe, passing from burned to fresh gases. However, the OH mass fraction, on Figure 2.11b, has a non monotonic behavior when the burned gases are over the probe. The OH mass fraction reaches a maximum value at the beginning of the reactive



(A) Temperature.



(B) OH mass fraction.

FIGURE 2.11: Unforced ICF temporal fluctuations obtained at 4 different positions, points G (—), I (□□), M (○—○) and O (-·-·), given in Table 1.3.

region, but this species continues to react with others products, consequently decreasing its mass fraction until the equilibrium is nearly achieved, around 3×10^{-3}, which agrees with what was discussed in Section 1.2.2.

2.4.2 Forced flame analysis

This section presents a parametrical study of the harmonically excited ICF. A temperature gradient mesh refinement threshold of 50 K/m is applied, as described in Section 2.2. Based on the results of the model with a tighter mesh adaption criteria, one may expect mainly the forcing response to be recovered, such that the natural behavior is seen with less strength. The harmonic excitation is defined by Equation (2.1), with a root mean square magnitude of 0.14 m/s, as previously discussed in Section 2.2. Different situations are simulated, varying the excitation frequency from 50 Hz to 250 Hz. Such a choice is based on the experimental studies [9], [10], which have shown that the flame presents a harmonic response to a incoming velocity excitation in the frequency range $f < 400$ hz. The Strouhal number ($S_{td} = f \cdot (d/\bar{v})$) varies between minimum and maximum values of 0.476 and 2.37, respectively, which are linked to the minimum and maximum exciting frequency of 50 and 250 Hz. In this

section, the fluctuation flame structures and the flame surface analysis is presented first, then, the flame transfer function is determined.

All the simulations presented here span at least 400 ms, which is the window used for computing the results for the Fast Fourier Transform and the flame transfer function.

Fluctuating flame structures

Figure 2.12 gives the flame surface area instantaneous position for the forcing of 50, 75, 100, 125, 150, 172 and 200 Hz. Each row corresponds to a different frequency, whereas the elapsed time labels the image at each column. The starting time (zero ms) corresponds to the beginning of a cycle, defined by the instant when a wrinkle starts developing at the anchor point. A time span of 20 ms is presented, with the flame front depicted at equally spaced intervals of 2.5 ms, thus presenting at least one flame response period for each excitation. It is worth to note, however, that this image interval choice does not permit to follow flame front behavior corresponding to higher frequencies. A longer sample interval, which enables to follow the flame front behavior more completely, is presented in Appendice A. Similarly to what has been observed for the unforced flame (section 2.4.1), the excited flame response is analyzed separated in three regions; (a) the first closer to stabilizing rod, (b) the second one downstream along the flame, where the roll up is seen, and (c) the third at the flame tip, where the pinch-offs are seen.

The flame base response gives an inverted conical shape for all incoming excitations seen on Figure 2.12, however, different patterns are seen. In the first three rows (for 50, 75 and 100 Hz), the flame base oscillates between two different positions; a narrow and a wide V-shape are seen. At the first line, e.g., where the ICF is under a forcing of 50 Hz, the instant 0 ms presents a narrow V-shaped, while instant 12.5 ms presents a wide shape. For a forcing of 100 Hz, instant 5 ms shows narrow V-shaped, whereas at instant 10 ms a wide V-shape is seen. Moreover, when the forcing frequency increases $f > 100$ Hz, at the following four rows (125 Hz, 150 Hz, 172 Hz and 200 Hz), this oscillatory behavior is not remarked, i.e., the ICF presents a wide V-shape. However, the flame front is wrinkled along its base, as seen clearly at the sixth and seventh row, where $f = 172, 200$ Hz, respectively, for all instants. These wrinkles are linked to the incoming velocity excitation, and begin at the anchor point of the ICF, at the centered bluff-body, propagating then along the flame front.

The wrinkles development along the ICF lead to the flame front roll up, which dominate the second and the third regions of the flame. The roll up effect is clearly seen for all excited flames, such as seen for an excitation of 100 Hz, at the sequence of instants $t = 0$ to 10 ms, however, it presents different shapes due to different forcings. At the flames where the incoming forcing frequency varies from $50 \leq f \leq 125$ Hz $(0.48 \leq S_{td} \leq 1.19)$, the roll up is easily remarked, e.g., instants 2.5 ms to 5 ms for the incoming forcing of 125 Hz, where the wrinkle starts bending the flame, forming a small bulge which subsequently develops into a roll up. The ICF with incoming forcing ranging from $125 < f \leq 200$ Hz $(1.19 \leq S_{td} \leq 1.9)$, however, shows a different roll-up development, since the wrinkles are present along the whole flame front, the roll up starts in a later state. It should be stressed that, at the seventh row, for 200 Hz, the flame has a combined behavior, such that the bulge start forming along the flame front and it can be seen initially, as in instants 0 to 5 ms, but not subsequently (at instants 15 to 20 ms).

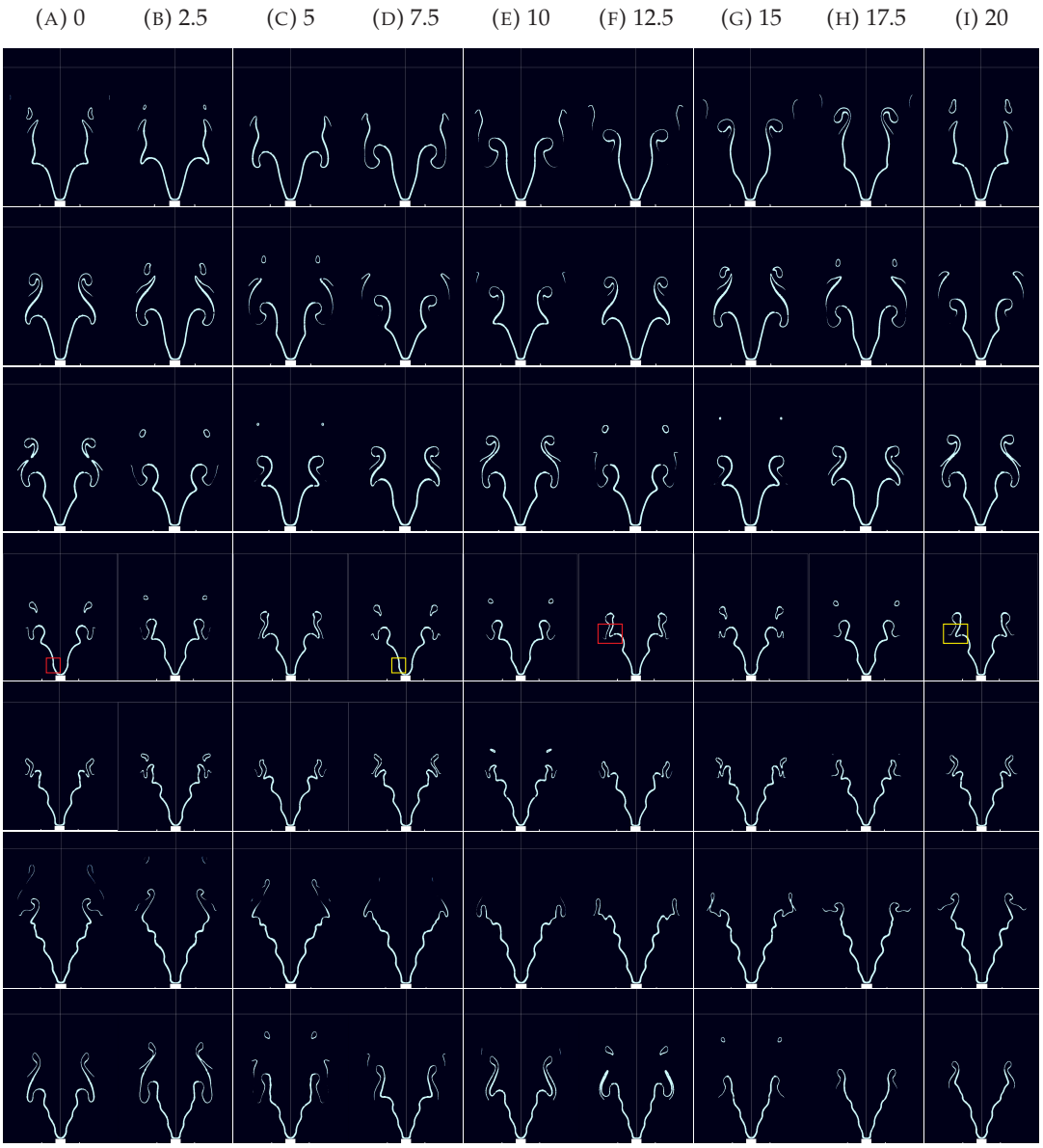


FIGURE 2.12: Flame front surface at different, equally spaced instants (by 2.5 *ms*), for different forcing frequencies. Each row presents a different forcing frequency, in the following order: 50, 75, 100, 125, 150, 172 and 200 *Hz*, corresponding to Strouhal numbers of 0.48, 0.71, 0.95, 1.19, 1.43, 1.63 and 1.9.

Eventually, the roll-up effect at the flame front evolves until the tip of the flame is completely bent, such that two sections of the flame collapse into each other, causing the annihilation of the respective section of the flame front and creating a pinch off. This phenomenon is seen at the ICF for all incoming excitations frequencies, characterizing the last third of the ICF, however some variations are seen. The forcing frequencies ranging from 50 to 125 Hz yield a well defined pinch off, e.g., as shown at the second row ($f = 75$ Hz), instant 15 ms. Nonetheless, the ICF response to higher frequencies (125 to 200 Hz) presents a slightly smaller and less intensive pinch off, when compared to lower frequencies, as seen at the sixth row ($f = 172$ Hz, $S_{td} = 1.63$) for the sequence of instants $t = 12.5$ to 15 ms. Again, the flame response to 200 Hz (seventh row) presents a mixed behavior, which is linked to the fact that

this forcing is an harmonic of the 100 Hz frequency.

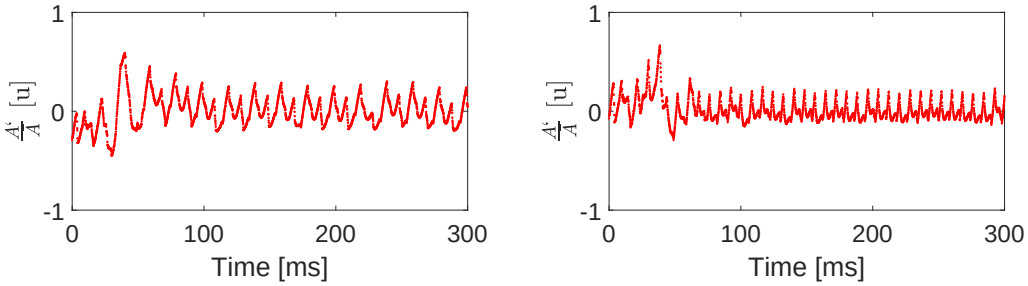
Moreover, Figure 2.12 also suggests a general classification of the ICF response in terms of similar behavior; the behavior (1) due to low frequency forcing, at the first to the fourth rows, $50 \leq f \leq 125\ Hz$ $(0.48 \leq S_{td} \leq 1.19)$, and (2) due to high frequency excitation, from the fifth to the seventh row, $f > 125\ Hz$ $(S_{td} > 1.19)$. For instance, the first class is characterized by a strong flame response due to the incoming excitation, and all phenomena are linked to the frequency of the forcing. The second class corresponds to a mixed response, such that the flame behavior due to the incoming forcing and the flame natural behavior interact.

It should be stressed that the ICF response to incoming velocity excitation of $125\ Hz$ $(S_{td} = 1.19)$ has a smaller flame length (and thus surface area) when compared to response due to other forcing frequencies. This effect is caused by the interaction between the wrinkle velocity propagation and the pinch off. Indeed, the wrinkles travel along the flame front, causing the roll up and pinch off, faster than the velocity which the flame takes to naturally develop. For instance, at the fourth row of Figure 2.12 ($f = 125\ Hz$) the wrinkle travels from the flame anchor point, e.g. the red box at 0 ms, to the instant where it interferes with the bulge formation, e.g. the red box at 12.5 ms, with a propagation time of $\approx 12.5\ ms$. Moreover, while the first wrinkle (red box) propagates, a new wrinkle starts forming (yellow box at 7.5 ms), due to the excitation frequency. The second wrinkle (yellow box) then travels along the flame, until it interferes with a second bulge, as shows the yellow box at 20 ms. In effect, the wrinkle propagation time is 14 ms, such that its frequency is $\approx 62.5\ Hz$, which is also an harmonic of the forcing frequency of 125 Hz, creating a constructive interference between both phenomena and causing the flame front length reduction.

Flame surface area fluctuation frequency analysis

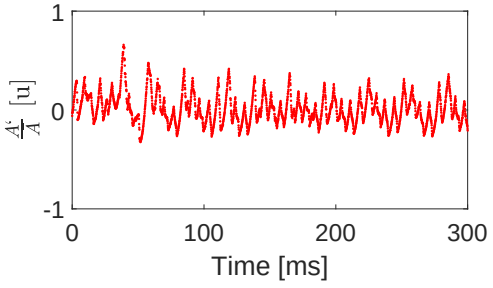
To quantify the dynamic behavior of the flame, similarly to the analysis performed for the unforced case 2.4.1, the flame surface area fluctuations are analyzed for different incoming velocity excitations frequencies, as described by Equation (2.1) and depicted on Figure 2.13. Four different flame behaviors are found to arise, depending on the incoming excitation frequency. First, the ICF response presents an oscillating behavior associated to the forcing, and some of its harmonics, as suggests the two different type of excursions seen on Figure 2.13a. The second behavior is marked only by the forcing frequency, such as when $f = 125\ Hz$, as Figure 2.13b depicts. It is worth to stress that some noise in seen on Figure 2.13b, and this high frequency excursion correspond to a computational error, as discussed in Section 2.4.1. The third behavior, given on Figure 2.13c, is marked by a flame response at the incoming forcing frequency and some other unknown frequencies. The flame surface response due to higher incoming frequencies excitation ($f > 150\ Hz$), corresponding to the fourth ICF behavior, is not disturbed by the forcing frequency, but presents a nonlinear response that does not suggests any visual classification, as depicted on Figure 2.13d where $f = 200\ Hz$. The corresponding frequency spectra results of the flame surface area fluctuations are presented on Figure 2.14.

As expected from the experimental results, the ICF is characterized by a remarkable harmonic response to the incoming excitation, and its behavior depends on the forcing frequency, which underscores the validity of the model. It is noteworthy that the incoming velocity forcing is harmonic immediately upstream to the flame, for all forcing frequencies. The flame surface area response at frequencies $f = 50$ and $125\ Hz$ $(S_{td} = 0.48$ and$1.19)$, Figures 2.14a and 2.14d respectively, are marked by the

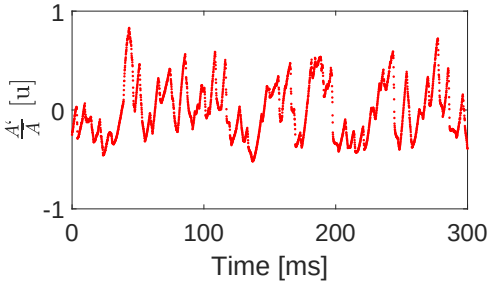


(A) $f = 50Hz$.

(B) $f = 125Hz$.



(C) $f = 150Hz$.



(D) $f = 200Hz$.

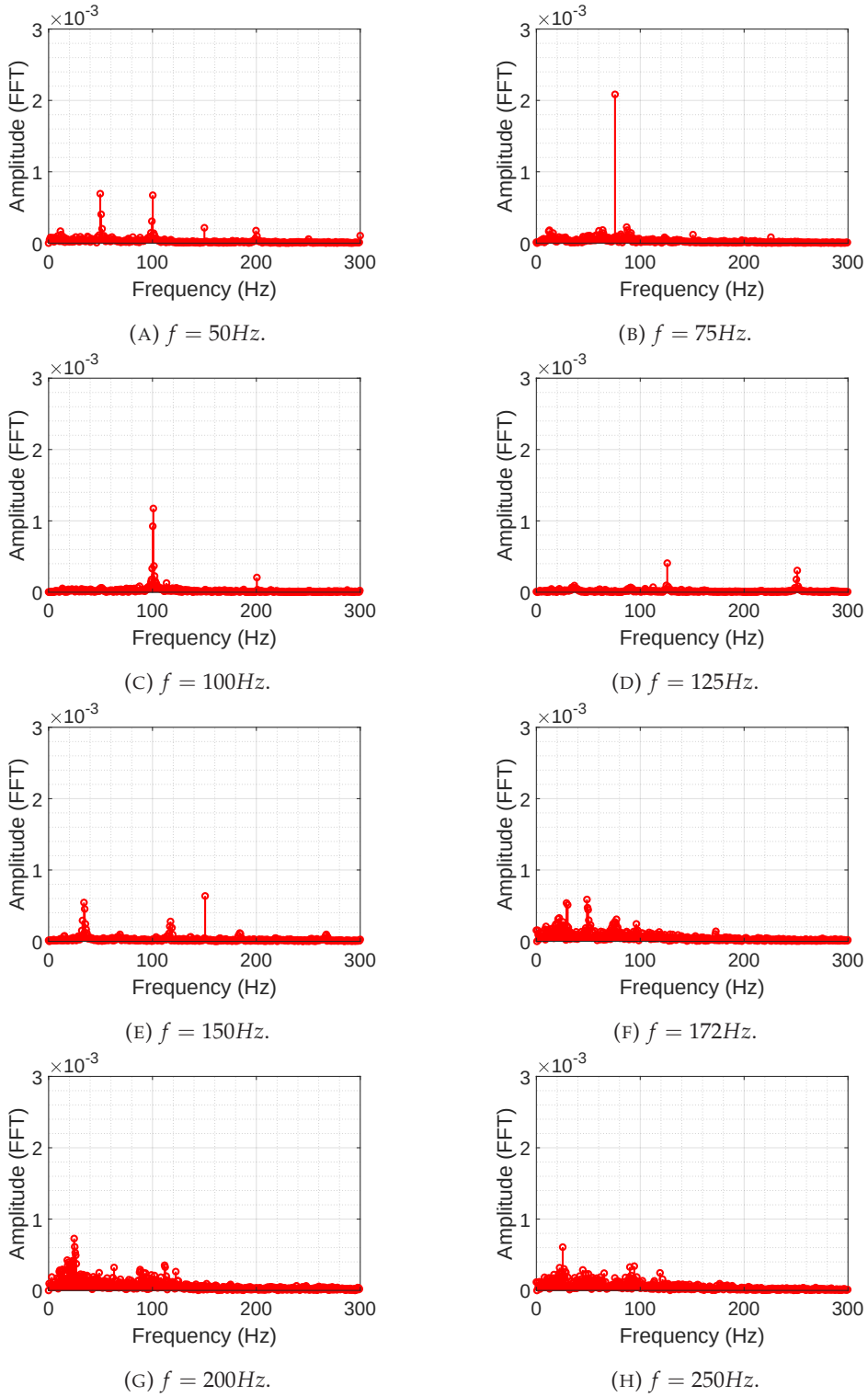
FIGURE 2.13: Flame surface area fluctuation due to four different incoming forcing frequencies, underscoring the flame different responses.

incoming excitation and also by a few harmonics of the forcing. Energy is indeed concentrated at the respective forcing frequency of Figures 2.14a and 2.14d ($f = 50$ and $125\ Hz$) and at its harmonics, i.e., at $f = 100\ Hz$ for the former excitation and $250\ Hz$ ($S_{td} = 2.37$) for the latter. Others ICF responses also exhibit harmonics of the forcing excitation, but with a significantly smaller amplitude, such as for an excitation of $f = 100\ Hz$ ($S_{td} = 0.95$) (Figure 2.14c), where the highest gain is expected from experiments [9]. Moreover, when the forcing frequency increases to $f = 150\ Hz$ ($S_{td} = 1.43$), significantly different behavior arises: a mix between the forcing and low frequencies is seen on Figure 2.14e, with a remarkable flame response around $f = 35\ Hz$ and one at $f = 150\ Hz$, where the first frequency marks the natural behavior of the ICF. Then, for $f \geq 172\ Hz$ ($S_{td} \leq 1.63$), depicted on Figures 2.14f-2.14h, the flame response to the incoming excitation is characterized by a low magnitude, around $35\ Hz$, which is also associated be the flame natural harmonic behavior, and also by a broadband amplitude signal.

Unfortunately, the available experimental results [10], [72] does not include such detailed flame surface area data as those presented here, nor the full spectral analysis. However, since the flame spectral response seems to significantly vary with the forcing frequency, it would be interesting to revisit this flame with diagnostics able to perform a time and spatial resolution of the flame surface.

Flame transfer function

Given the ICF frequency response, it is now possible to characterize the thermo-acoustic response of such flames, enabling a direct comparison between the experimental and numerical results. The FTF is here calculated as expressed in Section 2.3.1. Figure 2.15 depicts the root mean square of the velocity (v'_{rms}) and flame surface area fluctuations (A'_{rms}), followed by the mean of the flame surface area ($\bar{A}$) as a



(A) $f = 50Hz$. (B) $f = 75Hz$.

(C) $f = 100Hz$. (D) $f = 125Hz$.

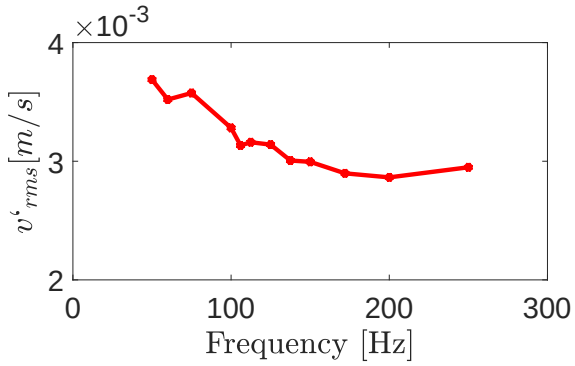
(E) $f = 150Hz$. (F) $f = 172Hz$.

(G) $f = 200Hz$. (H) $f = 250Hz$.

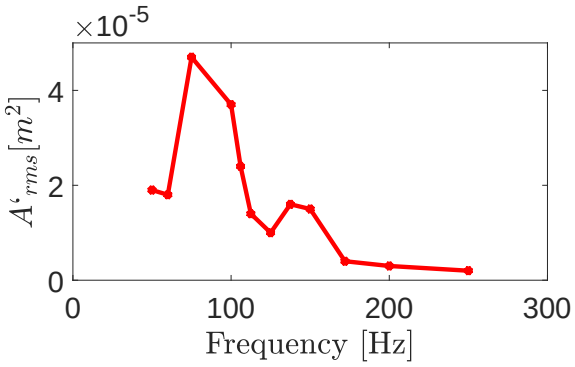
FIGURE 2.14: Harmonic response of the flame surface area fluctuation for different forcing frequencies (f).

function of frequency [Hz]. The corresponding gain and phase of the FTF are given and compared to experimental data on Figure 2.16.

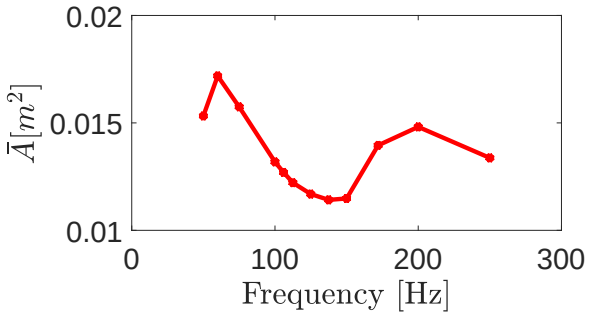
The RMS of the velocity fluctuation immediately upstream to the flame, shown on Figure 2.15a exhibits a decreasing trend with frequency. Such a decrease is associated to the boundary layer thickness decrease with frequency predicted by the



(A) RMS(v').



(B) RMS(A').

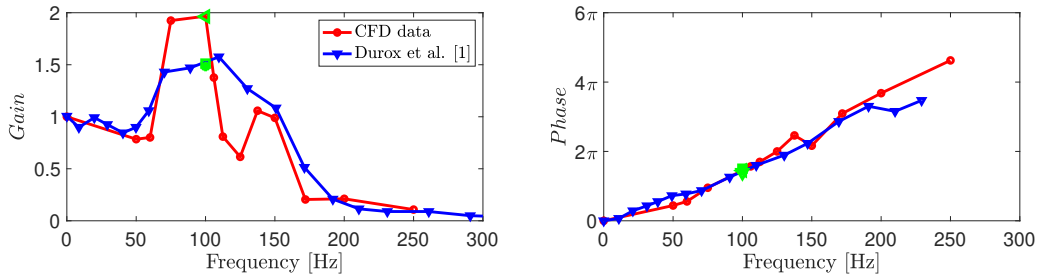


(C) Mean of A.

FIGURE 2.15: Dependency of the RMS of the inlet velocity fluctuation, RMS and mean of the flame surface area fluctuation with the forcing frequency (f).

solution of the second Stokes problem [77]. Conversely, the larger flow cross section blockage due to thicker boundary layers at lower forcing frequencies leads to larger core flow velocity fluctuations.

The RMS of the flame surface area fluctuation (Figure 2.15b) presents its maximum value at the frequency of 75 Hz, and it decreases until it achieves ≈ 0.01, and also, a sudden drop close to 125 Hz. The mean surface area also varies remarkably (Figure 2.15c), such that its maximum is around 60 Hz, and it decreases for frequencies $75 < f < 150$ Hz $(0.71 \leq S_{td} \leq 1.43)$, where it stabilizes, remaining almost constant ≈ 0.014 m^2. This sudden decrease is linked to the length of the inverted conical flame front, which decreases due to the interference between the forcing frequency and the wrinkle propagation time, as already discussed in Section 2.4.2.



(A) Gain. (B) Phase.

FIGURE 2.16: Gain and phase difference between velocity and flame surface area fluctuation of the ICF as a function of the incoming forcing frequency. The results for experiment [10] and CFD are compared. Also, the values for the gain and phase at 100 Hz for different mesh adaption temperature gradients are given for the following gradients; 10 K/m (□), 25 K/m (○), 50 K/m (◁) and 100 K/m (△).

Moreover, the impact of changing the mesh adaption gradient for a forcing frequency of 100 Hz is clearly seen on Fig. 17 also. As discussed in Section 2.5, when refinement thresholds of 10 and 25 Hz (□ and ○) are used, the gain matches the experimental result, which is 1.5. When the threshold is larger (◁ and △), the gain increases to 2 and 2.3, respectively. Concerning the phase, no remarkable difference is seen between the thresholds choices, all results agreeing with the experiments.

The gain, plotted on Figure 2.16a, presents a qualitative behavior similar to the experimental results [9]. The gain tends to 1 for low frequencies ($f \leq 60\ Hz$, $S_{td} \leq 0.57$), and it increases when forcing between $75 \leq f \leq 100\ Hz$ ($0.71 \leq S_{td} \leq 0.95$), reaching a maximum at $f = 100\ Hz$. It is worth to stress that this computed value is higher than the experimental one, which is associated to the mesh refinement threshold choice, that balances the computational cost with respect to model accuracy, as shown in Appendices B. Furthermore, the gain decreases between $100 < f \leq 125\ Hz$ ($0.95 \leq S_{td} \leq 119$), achieving its minimum value of 0.7 at $f = 125\ Hz$, which is linked to the flame surface area fluctuations suppression due to the wrinkle and pinch off interference. For higher frequencies, $f \geq 150\ Hz$ ($S_{td} \leq 1.43$), the model and experiments yield a remarkably close agreement, one for which the gain decreases with frequency. Finally, the phase, on Figure 2.16b, presents a similar behavior to experimental results, where the phase difference between velocity and flame surface area fluctuation increases linearly with frequency.

2.5 Synthesis

The mesh adaption influence analysis shows that the variation of the adaption temperature gradient threshold enables the characterization of the ICF natural and forced behavior. However, the choice of these gradients depend on the objective of the study. For instance, the use of a tight refinement adaption threshold of 10 K/m permits the complete characterization of the flame front, such that even the flame tip behavior is seen, but at the expense of a prohibitive computational cost (at least 2 months for calculation). Also, using a thigh threshold enables the identification of

a flame natural behavior, at a frequency of 35 Hz, in addition to the external forcing of 100 Hz. Enlarging the refinement threshold to 50 K/m, nevertheless, enables the modeling of the flame overall behavior (base, pinch off and wrinkles) and with acceptable reduced computational burden (at least 11 days), but precision is somewhat lost. Indeed, the flame extremities exhibit a different behavior, and the natural flame response is not seen to interact with the external forcing. Moreover, the use of a threshold of 100 K/m also gives an overall flame response that is similar to the one obtained with a threshold of 50 K/m, however, the flame front becomes non-linear, ans thus, is not representing a physical phenomena. Thus, the trade-off between the computational burden and the precision of the results must be kept in mind when using such mesh adaption methods to model thermo-acoustic sensible systems.

The unsteady model of the unforced ICF, also developed with Fluent 2019/2020, enables the further understanding of the flame dynamic behavior with such detailed skeletal mechanisms. The use of the skeletal kinetic chemical model, DRM19, enables the characterization of the instantaneous flame front and of its surface by means of mass fraction of CH_2 and OH. The analysis of the flame structures shows that the behavior of ICF is marked by instabilities in the unforced situation and the roll up of the flame front until the annihilation of a section of the flame, agreeing with previous experimental results. From the fluctuation analysis of temperature, pressure and OH mas fraction, the ICF computational model enables the detailed characterization of the flame front dynamic behavior. Moreover, the CFD results present a well defined solution for different time and space scales, being able to describe the flow of the substances within the fast dynamic movement of the flame front, improving from other standard techniques. For instance, the level-set modeling approaches permits to compute the FTF also. However, the skeletal kinetic mechanism used here enables also to determine the internal flame structure in detail, such as the different species on the flame front and the associated time and space scales.

The studied ICF experiment is surrounded by ambient air. Even though most of flame the burns a homogeneous mixture, at the flame tip the premixed gases equivalence ratio decreases. It was seen that this flame tip plays an important role on the flame dynamic response, since this is where the pinch-off occurs. Correctly describing such a variable equivalence ratio region seems crucial to predict the flame instabilities. Nevertheless, it would be interesting to compare the results of this model with a simulation using one-step or four-step kinetic mechanism in the future, such as using optimized single-step (OSS) chemistry models [78].

The forced unsteady inverted conical flame model studied enable the detailed characterization of the forcing on the flame front dynamic response. The ICF has three main regions; (1) the base that has a conical V-shape that oscillates from narrow and wide, and where the development of the wrinkles are seen, (2) the roll up section at the downstream of the flame and (3) the flame tip, where the flame annihilation happens. Each of these regions is impacted differently by the incoming excitations, i.e., the flame base presents oscillating behavior between wide and narrow V-shape when forced with frequencies between $50 \leq f < 125\ Hz$ $(0.48 \leq S_{td} \leq 0.1.19)$, and it switches to a steady wide shape when $f \geq 150\ Hz$ $(S_{td} \geq 1.43)$. The roll up section exhibits a similar response to the various forcing frequencies. The flame rolls up until annihilation in all cases, however, the position where the roll up occurs along the flame front varies with the forcing, being in a earlier stage for $f \leq 125\ Hz$ $(S_{td} \leq 1.19)$, and in a later stage for $f \geq 150\ Hz$ $(S_{td} \geq 1.43)$. The third region, where the pinch off happens, also has shown a similar behavior for most cases, i.e., all forced ICFs present the annihilation of the flame front at a given instant. This

phenomenon is seen at the forcing period when the excitation frequency is smaller than 125 Hz, but not in synchronized time when $f \geq 150\ Hz$. This loss of the synchronization is associated to the interaction between the flame natural behavior and the ICF response due to the excitation. Moreover, when a excitation frequency of $f = 125\ Hz$ is used, a remarkable reduction on the flame length is caused by the interaction of the wrinkle and the pinch off, impacting also in the flame surface area fluctuation, and therefore on the gain.

The excited ICF frequency analysis of flame surface area fluctuation underscores the multiple behaviors of the flame due to forcing with different frequencies. The response when $f = 50\ Hz$ has a strong response due to forcing and its second harmonic (100 Hz), however, for higher frequencies ($75 \leq f \leq 100\ Hz$, $0.71 \leq S_{td} \leq 0.95$), the response is only due to the forcing. Moreover, when the excitation frequency is around 150 Hz, the flame presents a mixed response due to the incoming velocity fluctuation, which interacts with the flame low frequency natural behavior ($f = 35\ Hz$). At higher frequency excitation, i.e., $f > 150\ Hz$, the flame does not respond to the forcing, but has a strong natural response, characterized by a broadband frequency around 35 Hz. Furthermore, the frequency analysis enables the characterization of ICF thermo-acoustic response by means of FTF gain and phase.

The computed gain agrees with the experimental results, however, two main discrepancies are seen; first, the maximum gain has higher value ($G \approx 2$) then expected at frequencies $f = 75, 100\ Hz$, as a result of the choice of mesh adaption refinement gradient threshold of 50 K/m to model the excited flame. Besides, a decrease on the gain is obtained for $100 < f \leq 125\ Hz$, reaching $G = 0.8$, which is a consequence of the interference between wrinkles and pinch offs at the flame front. Furthermore, the FTF phase shows remarkable agreement with the experiments.

One may note that this study enabled a detailed characterization of the ICF and its surface area and its full spectral analysis, which has not been included by experimental analysis [7], [9]–[11]. In this chapter it was shown that the flame response due to different excitations significantly varies with the forcing, presenting different behaviors. Therefore, would be interesting to revisit the experiments with methodologies that enable a more detailed flame characterization.

The successful modeling and characterization of the ICF response to incoming velocity excitations open doors to the prediction of thermo-acoustic instabilities, by means of Flame Transfer Function, with different approaches. Even though the CFD modeling presents remarkable results, its computational cost is high, and other modeling methodologies, such as Reduced Order Models (ROM), could enable to characterize the flame thermo-acoustic response with smaller computational burden. However, since the ICF presents a naturally unstable dynamical behavior, achieving a ROM that is representative of the flame complete dynamics requires a deeper study, which is the subject of future works.

Willing to estimate a steady-state equilibrium for the ICF for different premixed fuel inlet velocity, under feasible computational time, the next chapter is dedicated to developing a steady ROM, based on CFD averaged data of the inverted conical flame. This work is a first step towards the ROM of the dynamical behavior of unstable premixed flames.

Part II

Machine Learning

Chapter 3

Steady Reduced Order Model

Dans ce chapitre, la construction et la caractérisation d'une ROM de flammes laminaires prémélangées ICF avec une dilution variable par l'air est développée. Le logiciel StaticROM, de Twin Builder(Ansys) est utilisé pour développer un modèle simplifié de la CIF basé sur des données CFD stables, modélisées comme indiqué dans le Chapitre 1. Cette ROM a la vitesse d'entrée du mélange carburant/air comme entrée, et les champs des composantes de la vitesse de la flamme et de la température obtenus avec Fluent comme sortie. Comme le montre le chapitre 3.3, une ROM prometteuse de l'ICF laminaire prémélangé est obtenue.

In this chapter, a ROM of laminar premixed flames ICF with variable dilution by air is developed. The software StaticROM, from Twin Builder(Ansys) is used to develop a simplified model of the ICF based on steady CFD data. This ROM is able to predict the temperature steady-state fields for a range of values of the fuel/air mixture inlet velocity. Only a small number of data points in this range is used to train the ROM, which still shows promising results.

3.1 Introduction

The use of machine learning techniques to model complex system has been subject of study for several fields in the past decades. Traditionally, the study of such systems depends on a massive amount of data from experiments, numerical simulations and field measurements [79]. Machine learning techniques are used to model systems in a modular and agile way, with low computational cost, e.g., to address many problems in fluid mechanics [79], image processing [80] or bio-mechanics [81]. Reduced order models (ROM), for instance, have also been recently used coupled with machine learning processes, significantly decreasing the cost of parametric exploration for complex systems. Reduced models are built over a few well chosen data points in the design space, which, in turn, enable the reduced model to accurately describe the system of interest, even when large parametric excursions arise [81].

Several machine learning techniques have been proposed for modeling different physical systems, such as online and offline models. Online models, which have their learning process developed while the corresponding measurements are undertaken, were previously studied, for example, as Neural Network applied to image recognition [80] or as nonlinear Autoregressive Exogenous (NARX) Neural Network applied to solar radiation [82], and include statistic models as well. Offline models, which are developed over measurements already obtained, involve, for instance, the decomposition of the available data to retain its important features, first using compression techniques, such as proper order decomposition (POD) or singular value decomposition (SVD). Then a machine learning approach is applied to learn the studied system. Offline models coupled with SVD have been applied to

several physical systems, such as on the modeling of pressure ulcer prevention [81], and with POD, such as the thermal behavior of fluid-cooled battery [83].

The computational fluid dynamics (CFD) modeling of combustion processes, which are high-fidelity complex model, demand a significant computational cost due to the complexity of the solved equations, as discussed in Chapter 1. It is often impracticable to develop a parametric study using CFD generated data. For this reason this chapter is devoted to building and characterizing a reduced order model of steady axisymmetrical, laminar premixed flames with variable dilution by air. In this reduced order model takes the fuel/air mixture inlet velocity is taken as input variable, and outputs are the flame velocity components and temperature field.

This chapter is organized as follows; first the reduced order model numerical methodology is presented, followed by the ICF data generation procedure overview. Then, the steady state ICF available CFD data is presented, and the ROM results based on CFD data are discussed.

3.2 Numerical Methodology

In this section, a steady-state Reduced Order Model (ROM) of the ICF is constructed. The construction relies on CFD model presented in Section 1.6 and uses model reduction tools from Ansys TwinBuilder to characterize the flame response to changes in the inlet velocity. The tools used to create the steady ROM are described in Section 3.2.1, followed by the characterization and presentation of the learning dataset in Section 3.2.2.

3.2.1 Reduced Order Model

A reduced order model is a simplification of a high-fidelity steady or dynamical model, which reduces the computational cost or the storage capacity of complex models. The goal is to preserve the essential behavior and dominant effects of the system. Here, a model enabling the efficient computation of the fields of several physical quantities of interest, at steady-state, for a range of inlet velocities is designed. The approach relies on the solution of the CFD model described in 3.2.2, for several values of the inlet velocity. An interpolation between the CFD data is done using a methodology described below, and summarized on Figure 3.1.

As shown on Figure 3.1, the first step in developing a steady state ROM is to set the samples (or snapshots) to the training, which are representative data points of the complete modeled system. A snapshot set is defined by an ensemble of samples used for training the ROM. The training set is then divided into two; the learning and validation snapshot sets. The learning set consists of approximately 60 % of the training snapshots, distributed throughout the whole training set. It is important to stress that the learning set must ensure that the boundaries of the parametric input variables are included in the system learning process, in order to avoid validation through extrapolation. The validation snapshots consist of the remaining 40 % of the original set.

The second step is the application of a Singular Value Decomposition (SVD) on the learning snapshots. Each of the learning snapshots corresponds to a small set of modes coefficients when projected to the reduced SVD base [81]. The third step is the feature extraction, which compresses the learning set by retaining only its most important characteristics, i.e., its larger singular values. Then, the learning process of the ROM, the fourth step, is done by using a Genetic Aggregation Response Surface

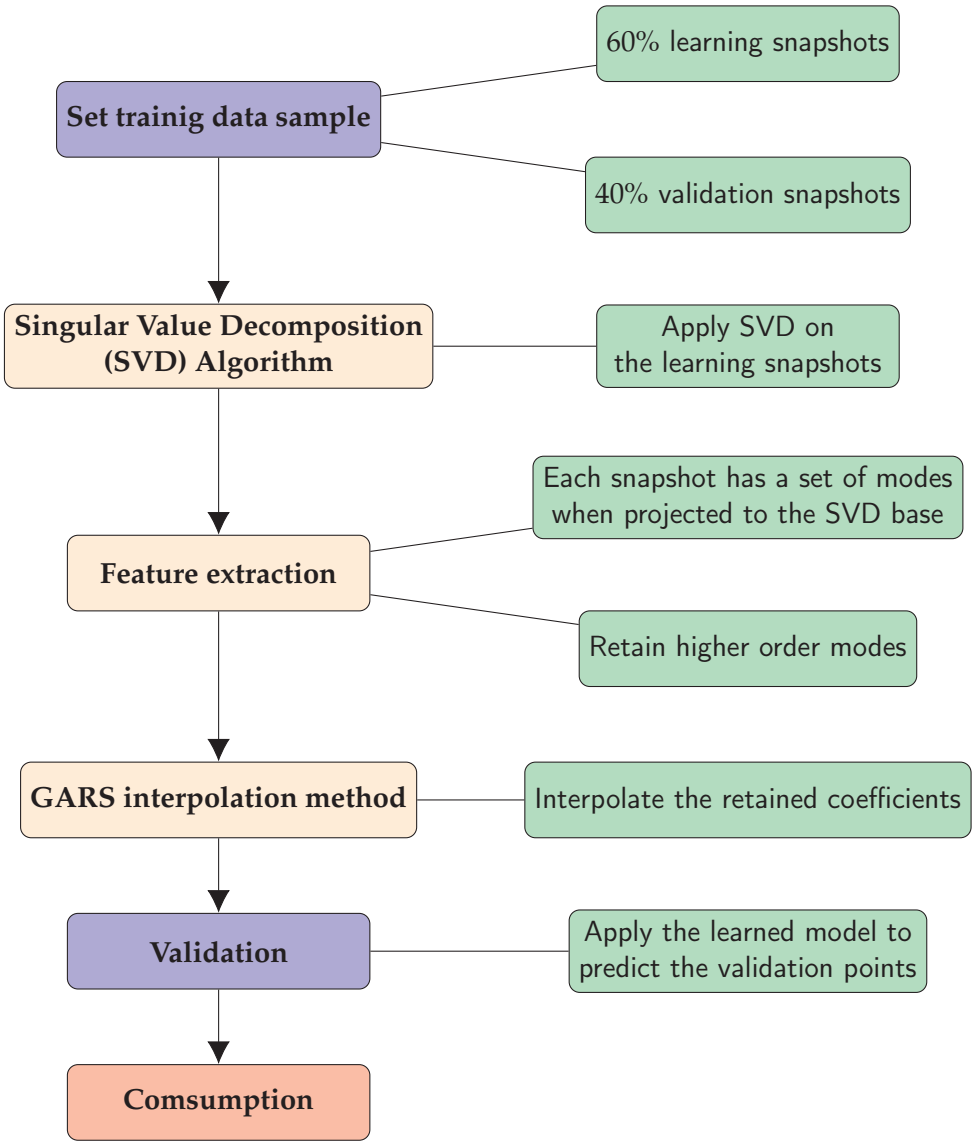


FIGURE 3.1: Flowchart representing the learning methodology for steady ROMs.

(GARS) to interpolate the system retained coefficients with respect to the calculation parameters [84]–[87]. The fifth step is the validation, which consists of the application of the model obtained by the interpolation over the validation snapshots and by computing the Euclidean Norm error between a given validation snapshots and the ROM interpolation results.

To create the training snapshot set for a random system, it is necessary to define the parametric space of interest. For instance, here a ROM is computed describing the ICF relation between the burner mean inlet velocity (or, equivalently, volume flow rate) and the flame properties fields at steady state. Other possibilities for the parametric space could be applied, such as using the burner outlet mean inlet velocity or the equivalence ratio as input value, but, for the sake of brevity, only one possibility is studied here.

3.2.2 ICF training data

The steady-state flame flow field is computed using the model described in Section 1.6. Seven ICF samples are modeled with CFD, with a varying burner outlet mean inlet velocity. All simulations are obtained with Fluent 2019 R2, each taking about 15 to 20 days to complete on a Linux-64 SuSE, at ANSYS cluster, Intel(R) Xeon(R) E5-2660 v3, using 108 nodes on 9 machines.

Moreover, each simulation has the nominal mean inlet velocity, v_i, of the premixed combustible gases varied according to the values presented in Table 3.1. Such values are chosen based on the nominal mean velocity of $v_d = 2.05\ m/s = v_3$, which has been studied in the experimental work [9], by varying the burner outlet mean inlet velocity of the fuel/air mixture in 5 % multiples of the nominal velocity, v_d. In what follows the nominal mixture volume flow rate and the mean velocity values are denoted as $\dot{\forall}_d$ and v_d, respectively.

TABLE 3.1: Fuel/air mixture parameters setup for the Fluent modeling of the Inverted Conical Flame. The values given represent the mean value at the burner outlet.

Sample (i)	0	1	2	**3 [9]**	4	5	6
$\dot{\forall}_i/\dot{\forall}_d$	0.85	0.9	0.95	**1**	1.05	1.10	1.15
$\dot{\forall}_i\ [cm^3/s]$	153.3	162.3	171.3	**180.3**	189.3	198.4	207.4
$v_i\ [m/s]$	1.7	1.85	1.95	**2.05**	2.15	2.26	2.36

It should be recalled that the analysis of the steady simulations showed that model does not converge strictly, but oscillates around a pseudo-steady state point, as discussed in Section 1.6.1. For this reason the data used to compute the ROM of the ICF is the statistically averaged, as seen in Section 1.6.2, since this provides a better approximation of the laminar premixed lean ICF steady state.

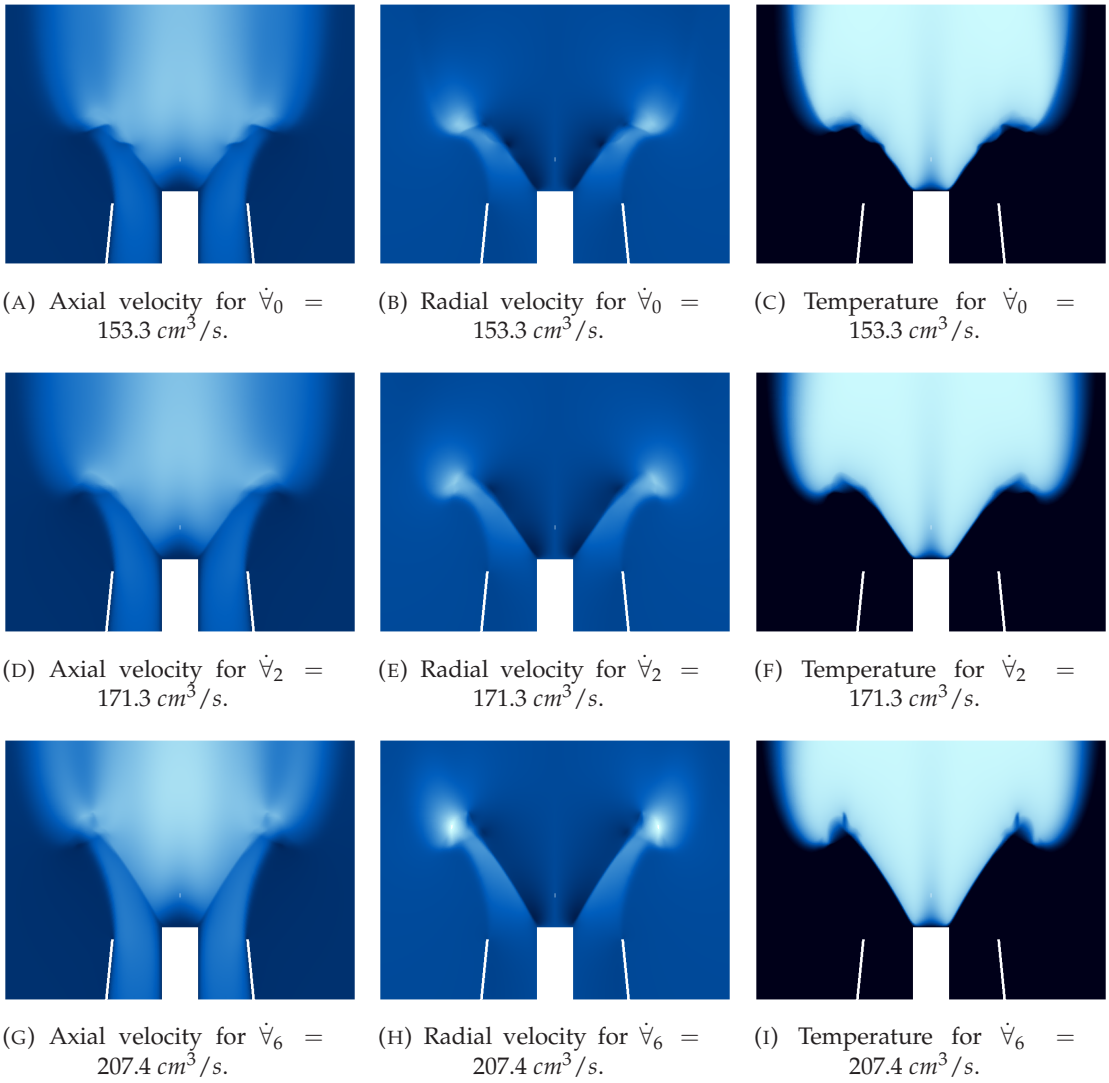
3.3 Results and Discussion

In this section results for the ROM of the lean premixed laminar ICF computed with Fluent are presented. First, an overview of the training sample is given in Section 3.3.1. Then, the ROM results are analyzed in Section 3.3.2.

3.3.1 Learning and Validation dataset generation

Here, the training set that is used to create the ROM of the ICF is discussed. Note that, as addressed in Section 1.6.2, a qualitative comparison of the average field yielded a smother flame front, with a shape resembling that of the steady experimental results [9]. Figure 3.2 shows training samples for the averaged axial and radial velocity components and temperature fields, for $i = 0, 2, 6$, given in Table 3.1.

For the sake of brevity, only three samples are shown on Figure 3.2, such that a mapping sample of the parametric space related to the ROM training is covered. It is worth to stress that the averaged fields of velocity components and temperature present a smooth flame front, underscoring what is discussed in Section 1.6.2 for the nominal scenario (scenario 3 on Table 3.1). Moreover, the impact of increasing on the mixture inlet flow rate is evident on Figure 3.2: the flame lengthens with the flow rate, as can be seen by comparing Figures 3.2b and 3.2h. Furthermore, the averaged field linked to the minimum flow rate presents a slightly different behavior when compared to the others. Indeed, the fields exhibits some smooth wrinkles at the



(A) Axial velocity for $\dot{\forall}_0 = 153.3\ cm^3/s$.
(B) Radial velocity for $\dot{\forall}_0 = 153.3\ cm^3/s$.
(C) Temperature for $\dot{\forall}_0 = 153.3\ cm^3/s$.
(D) Axial velocity for $\dot{\forall}_2 = 171.3\ cm^3/s$.
(E) Radial velocity for $\dot{\forall}_2 = 171.3\ cm^3/s$.
(F) Temperature for $\dot{\forall}_2 = 171.3\ cm^3/s$.
(G) Axial velocity for $\dot{\forall}_6 = 207.4\ cm^3/s$.
(H) Radial velocity for $\dot{\forall}_6 = 207.4\ cm^3/s$.
(I) Temperature for $\dot{\forall}_6 = 207.4\ cm^3/s$.

FIGURE 3.2: ICF training samples for the fields of velocity components and temperature, for three different fuel/air mixture flow rates. The colormap is defined as black an light blue at minimum values, respectively, i.e., $v_y \in [-1, 6]\ m/s$, $v_r \in [-2, 3]\ m/s$ and $T \in [298, 2200]\ K$.

flame tip (Figure 3.2c), whereas no wrinkle is visible for the cases with $\dot{\forall} = 171.3$ and 207.37 cm^3/s, presented on Figures 3.2f and 3.2i, respectively.

The samples presented in this section are those used to develop the steady ROM of the ICF, which is presented at the following section.

3.3.2 ROM Analysis

A reduced order model is created to predict the ICF using some of the flame properties obtained from the ICF Fluent model results. A total of seven samples are available for the ROM training, such that the number of data points used on the learning set of this system is varied between four or five points, to show the impact of the dataset size on this process. Here, the ROM input parameter is the fuel/air mixture mean inlet velocity, v_i, which values are given, for each of the data points, in Table

3.1. The ROM then predicts two properties: the flame averaged axial and velocity components and the averaged temperature fields.

In this study, two models are created for each of the ICF studied properties. The first ROM (denoted ROM4) is composed by a learning set of four samples (scenarios 1, 3, 4, 6 in Table 3.1), whereas the second one (denoted ROM5) uses five samples for learning (scenarios 0, 1, 3, 4, 6 in Table 3.1). For each ROM, scenarios 2 and 5 of Table 3.1 are used as the validation set. Once built, such ROMs should give an accurate approximation of the solution that can be obtained with the CFD solver, but for a different set of volume flow rates.

The model resulting accuracy depends on the number of samples in the training set, the number of modes used in the field compression of the learning dataset, the statistical reduction targeted precision for the flame fields and the interpolation error. Figure 3.3 compares the Fluent averaged model results with the ROM prediction of these results, with either four or five learning points, and four SVD modes, for the velocity components and temperature fields. Table 3.2 reports the errors resulting from the construction of each ROM.

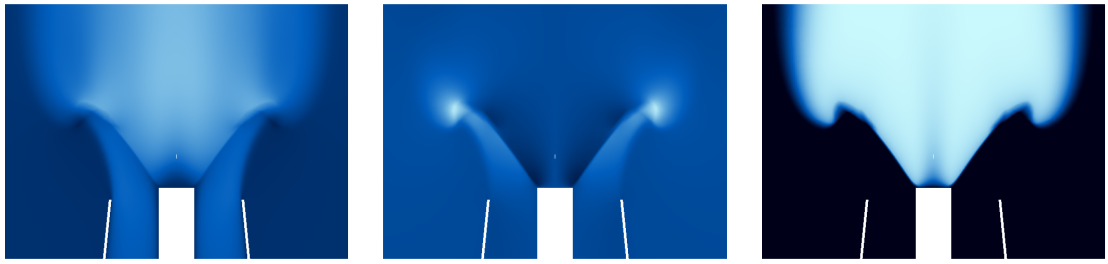
Figures 3.3a, 3.3b and 3.3c depict the average axial and radial velocity components, as well as temperature of the ICF for a volume flow rate of $\dot{\forall}_5 = 198.35\ cm^3/s$, modeled with Fluent. The corresponding steady state ROM results of the averaged ICF are given on Figures 3.3d, 3.3e and 3.3d for ROM4, and on Figures 3.3g, 3.3h and 3.3g for the ROM5.

Firstly, a qualitative comparison between the ROM and Fluent results, on Figure 3.3, enables to verify that the overall flow structure is captured by both ROM4 and ROM5. The important flow structures used to analyze the system results are; (1) the flame anchoring point at the top of the rod, (2) the angle of the ICF, which is directly related to the laminar flame speed, (3) the location of the smeared flame wrinkles, which indicates the dilution region and (4) the outer plume region. More precisely, on Figures 3.3d and 3.3g, the axial velocity, v_y , upstream and downstream to the flame front are equal for both cases, with a value of 2.34 m/s and to 4.2 m/s, respectively. However, at the dilution region, the ROM determined velocity goes from 2.34 m/s to 4.6 m/s. At this region the flame front is smoother and thicker.

Concerning the radial velocity component, v_r, on Figures 3.3e and 3.3h, abrupt changes are seen on the reactive region, varying from 0.9 m/s upstream the flame, to $-0.9\ m/s$ immediately after the flame front, and then slowly increasing, achieving a value of 0 m/s further downstream. Moreover, all ROMs have a smeared flame tip, which is similar to the Fluent averaged flame tip, on Figure 3.3b, presenting small differences on the smeared region size and shape only.

The averaged temperature ROM results, given on Figures 3.3f and 3.3i, increases from $T_\infty = 300\ K$, to $T_{ad} = 2200\ K$ on the fresh and burned gases regions respectively. Furthermore upstream and downstream the flame front, similar Fluent and ROM behaviors are observed. However, on the dilution region, the ROM flame front differs slightly from the Fluent model, exhibiting a smoother flame tip at the upper region when compared with Figure 3.3c.

The analysis of the ICF fields predicted by the ROM underscores that the temperature is the considered flame property that enables the identification the flame front position. Indeed, the interface between $T_\infty = 300\ K$ and $T_{ad} = 2200\ K$ is a well defined surface, both for the averaged Fluent and the ROM. Therefore, the temperature contour of the ROM5 result, which uses 5 learning samples, for $\dot{\forall}_5 = 198.35\ cm^3/s$, presented on Figure 3.4, is used to further understand and compare the flame front position and angle with respect to the fresh gases. Figure 3.4 depicts the temperature contour for the Fluent average in red, and the ROM5 prediction in yellow. Both



(A) Axial velocity component obtained with Fluent.

(B) Radial velocity component obtained with Fluent.

(C) Temperature obtained with Fluent.



(D) Axial velocity component obtained with ROM for 4 training data points.

(E) Radial velocity component obtained with ROM for 4 training data points.

(F) Temperature obtained with ROM for 4 training data points.



(G) Axial velocity component obtained with ROM for 5 training data points.

(H) Radial velocity component obtained with ROM for 5 training data points.

(I) Temperature obtained with ROM for 5 training data points.

FIGURE 3.3: Comparison between the Fluent averaged results with ROM prediction for the averaged steady ICF, for a fuel inlet volume flow rate of $\dot{\forall}_5 = 198.4\ cm^3/s$. The colormap is defined as black an light blue at minimum values, respectively, i.e., $v_y \in [-1, 6]\ m/s$, $v_r \in [-2, 3]\ m/s$ and $T \in [298, 2200]\ K$.

curves are anchored at the same position, i.e., at the top of the bluff-body, and the flame front overlaps for the Fluent and ROM results on the flame base. However, the steady state ROM model is not capable of fully predicting the flame front position without error. Indeed, at the dilution by external air region, further along the flame, the red and yellow lines do not overlap, and exhibit different angles. The angle with the vertical axis has been approximated by a protractor and are 28.13° and 30.38°, for the Fluent (red) and the ROM (yellow curves), respectively. This discrepancy corresponds to a total error of 8 % for the ROM result of the front angle at the air diluted flame tip.

To summarize the ROM prediction capabilities, Table 3.2 gives the quantitative prediction error for the ROM developed in this work. For each property field, the corresponding average RMS error of the SVD decomposition of the training set, and

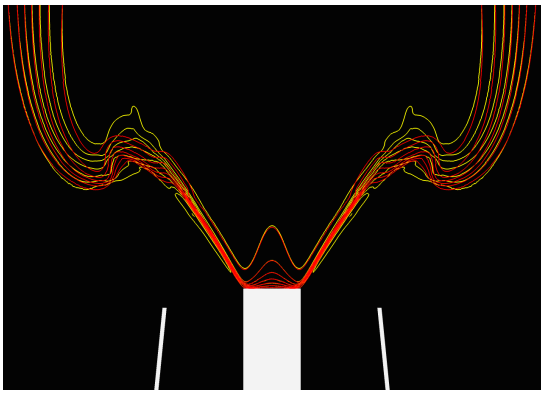


FIGURE 3.4: Comparison of the contour of the flame temperature for the ensemble averaged steady Fluent result (red) and the StaticROM (yellow) prediction for the ICF case 5, with a volume flow rate of $\dot{\forall}_5 = 198.4\ cm^3/s$. [36]

Euclidean norm error of the ROM prediction is computed. In Table 3.2, the prediction of the velocity components and temperature show that the reduction error is zero for the all the properties predicted by ROM4 (ensemble average velocity $\bar{v}$ and temperature $\bar{T}$). This is evident, since the SVD is done over four learning samples, and the number of modes used for the ROM is the maximum available, which is four also. Upon increasing the number of points, one may verify that the reduction error increases, since the SVD is computed over five learning data points, but only the four largest modes are used on the ROM.

TABLE 3.2: RMS errors of the SVD and ROM Euclidean norm errors of the learning using 4 modes, for each of the developed models.

	SVD		ROM	
Number of learning data points	$\bar{v}_{error}$ (%)	$\bar{T}_{error}$ (%)	$\bar{v}_{error}$ (%)	$\bar{T}_{error}$ (%)
4	0	0	2.56	1.03
5	0.558	0.762	2.47	1.26

Regarding the errors for the velocity components, the average ROM Euclidean norm error decreases from 2.56 % to 2.47 % when one point is added to the learning set, which underscores the flame similarities discussed previously for the comparison between ROM4 (Figures 3.3d and 3.3e) and ROM5 (Figures 3.3g and 3.3h). The temperature ROM prediction, however, slightly increases from 1.03 % to 1.26 % when changing from four to five learning samples, which also agrees with the high degree of similarity encountered on Figures 3.3f and 3.3i, since the error is smaller than 2 % for both cases.

Each of the ROM results presented above is computed in real time, taking around 30 s for the learning step of each created of the ROM. Nevertheless, as underscored in Section 1.6.1, a steady CFD simulation of the ICF takes about 15 days to compute. This represents a significant advance on the modeling of flames with an accessible, fast and less expensive method. Furthermore, all the obtained ROM exhibit a rather small error, i.e., less than 3 %, even though a set of 5 samples ii used for the learning only.

3.4 Synthesis

The analysis of the reduced order model of the averaged steady inverted conical flame showed that it is not only possible, but also beneficial, to apply such modeling techniques to predict the behavior of laminar premixed combustion. Using ROM provides a substantial reduction on the computational burden linked to the modeling of combustion. The ROM developed in this work lead to less than 3 % Euclidean norm ROM error, thus meaning that a correct prediction is achieved. One may note that these models are developed using a reduced amount of samples for learning and validation of the ROM. Since the ICF is a complex and sensible to the variation of the velocity inlet, the increase of the number of points on the training sample set could provide even better results.

It is worth to stress that the same methodology can be applied to model other flow properties, but in this work the focus was chosen the velocity components and temperature. It would be interesting to delve deeper in the chemical properties, such as modeling the field of species mass fraction, enabling to characterize not only the flow filed of the ICF, but also the chemical behavior.

Chapter 4

Luenberger Observers

Ce chapitre propose une conception numérique d'observateur de Luenberger pour les systèmes non linéaires, consistant en l'approximation des mappings impliqués dans une telle méthodologie d'observateur. Cette conception repose sur des simulations numériques de la dynamique d'un système d'intérêt et sur l'utilisation de réseaux neuronaux pour trouver les correspondances. L'approche diffère en fonction de la classification de la dépendance du système, comme autonome ou non-autonome. Pour les systèmes autonomes, une approche connue est utilisée [34]. Pour les systèmes excités, l'approche consiste à calculer les mappings correspondant à une excitation spécifique et bien choisie, de telle sorte que ces mappings puissent ensuite être utilisés avec d'autres entrées. Les résultats sont prometteurs, même pour des systèmes complexes, comme la combustion, comme l'illustre la section 4.4.4.

In this chapter, a numerical Luenberger observer design for nonlinear systems is proposed, consisting on the approximation of the mappings involved in such observer methodology. Such design relies on numerical simulations of the dynamics of a system of interest and the use of neural networks to find the mappings. The approach differs depending on the system dependency classification, as autonomous or non-autonomous. For autonomous systems, a known approach is used [34]. For excited systems, the approach consists in computing the mappings corresponding to a specific, well-chosen excitation, such that this mappings can then be used with other inputs. Results show promising results, even for complex system, such as combustion, as illustrated in Section 4.4.4.

4.1 Introduction

State observers are dynamical systems that combine a model and real-time measurements to estimate unmeasured states of a process. These estimates can then be used, e.g., for feedback control. As described in the previous Chapters, the combustion process is high-dimensional, featuring a large number of states, particularly when CFD models are involved. There is an important effort devoted to designing Reduced Order Models (ROM) capturing the essential dynamics of the process while keeping model complexity as low as possible. In [88], a ROM of a thermo-acoustic system is studied, where computational fluid dynamics (CFD) simulation is combined with tools from system identification to characterize a ROM representation of the dynamic of a sub-system, to incoming flow perturbations. The difficulty of placing sensors in combustion systems makes it impossible to measure all the states of these ROMs during a combustion process, let alone those of a CFD model. In this context, state observers can provide estimates of unmeasured quantities, provided the model they rely on is reliable.

More precisely, the state observers enable the estimation of the states of the thermo-acoustic response of flames. Such methodology achieves a state estimation based on a given training trajectory and measure. For instance, in the combustion experiments often measures of pressure are obtained through probes, and accessing other combustion properties is more complicated. In closed combustion chambers, the measure of pressure can then, coupled with a dynamic model of the combustion process and an observer, be used to estimate the heat release of the reactive system, enabling the estimation of thermo-acoustic instabilities, and also the control of such unstable systems.

4.1.1 Context

Observers are dynamical systems used to estimate the unmeasured states of a process, combining real-time data obtained from sensors with a dynamical model of the studied process. A few general observers design approaches for nonlinear systems exists. For instance, the popular Extended Filter [89] relies on the linearization around the current estimate, yielding local guarantees of convergence only. High-gain observers [90], in turn, rely on the strong assumptions on the observability of the system to map it to a triangular form, in which the design is eased. A review of generic observer design methods for nonlinear systems is given in [91].

In a seminal paper [92], the original Luenberger observer design for linear systems is presented. It is shown that observable linear dynamics can be mapped using an invertible variable change, which transforms into a linear, stable dynamical system, having the measurement as input. In other words, changing to a stable linear filter of the output. Then, implementing such filter from any initial condition enables to recover a state estimate of the process by inversion of this mapping. In [32], [93], the same idea of mapping the plant dynamics to a linear filter of its outputs is progressively extended to more general classes of nonlinear systems. In [34], a general notion of observability, *backward distinguishability*, has been shown to be sufficient to guarantee the existence of such an injective mapping. In [94], applications on non-autonomous nonlinear systems give similar result. Even if these results guarantee the existence of the mapping and its (pseudo-)inverse, they are not constructive, and the mapping has no tractable analytical expression.

This a chapter presents a numerical observer design for nonlinear systems that consists in the approximation of such mappings involved in the Luenberger methodology. The design relies on numerical simulations of the dynamics and the use of nonlinear regression. The proposed approach is as follows. For any stable chosen linear observer dynamics, numerical solutions are computed to both the system to be observed and the observer, fed by the corresponding output. Then, a nonlinear regression is performed on the data to compute an approximation of the problem corresponding mapping and its inverse. Different methodologies are proposed, depending on the system dependency classification. In the case of autonomous systems, the method straightforwardly uses the existent result from [34]. For a system with input, the approach consists in computing the mappings corresponding to a specific, well-chosen excitation, and guaranteed to exist [94]. Indeed, such mappings can then be used with other inputs, such that stronger observability assumptions are made and the observer dynamics are appropriately modified.

The nonlinear regression relies on Neural Networks methods. This machine learning approach enables the representation of a problem in multiple complexibility levels, obtained by composing and connecting simple but non-linear modules, also called neurons. These modules enable to transform the representation at one level

into a representation at a higher and more complex and abstract level [80]. Studied neural networks architectures composed by a sufficient number of these transformation modules show a high learning capability for diverse non-linear problems. For instance, different neural network methodologies have been extensively applied for image recognition [80], [95]–[97], for language processing [98], self-learning control systems [99], for the prediction of chaotic series [100], or for the predictive modeling of nonlinear dynamical systems [101].

This chapter is organized as follows. In Section 4.1.2, the formulation the observer design problem is presented. In Section 4.2, the proposed approach is described for both autonomous and excited systems. In Section 4.3, the architecture and learning approach of the neural network are presented. In Section 4.4, the proposed approach is exemplified through numerical simulations on toy examples of autonomous and non-autonomous systems.

4.1.2 Problem Statement

Consider a system of general form

$$\begin{cases} \dot{x}(t) = f(x(t), u(t)) \\ y(t) = h(x(t), u(t)) \end{cases}, \tag{4.1}$$

where $x \in \mathbb{R}^{d_x}$ is the system state, $y(t) \in \mathbb{R}^{d_y}$ is the measured output, f is a continuously differentiable function (C^1), h is a continuous function, and $u \in \mathbb{R}^{d_u}$ an input. For any input u of interest, the online estimation of $x(t)$ from the knowledge of the past values of the output y and input u is the subject of interest, under the following two assumptions.

Assumption 1

There exists a compact set $\mathcal{X}$ such that for any solutions x to (4.1) of interest, $x(t) \in \mathcal{X}$ for all $t \geq 0$.

Assumption 2

For any input u of interest, there exists an open bounded set $\mathcal{O}$ containing $\mathcal{X}$, such that (4.1) is backward $\mathcal{O}$-distinguishable on $\mathcal{X}$. Namely there exists $\bar{t} > 0$ such that for any trajectories x_a and x_b of (4.1), with input u and any $t \geq \bar{t}$, such that $(x_a(t), x_b(t)) \in \mathcal{X} \times \mathcal{X}$ and $x_a(t) \neq x_b(t)$, there exists $s \in [t - \bar{t}, t]$ such that

$$h(x_a(s)) \neq h(x_b(s)),$$

and $(x_a(\tau), x_b(\tau)) \in \mathcal{O} \times \mathcal{O}$ for all $\tau \in [s, t]$. In other words, their respective outputs become different in backward finite time and before leaving $\mathcal{O}$.

Remark 1. *For non-autonomous systems, the time $\bar{t}$ within which the outputs are distinguishable to be uniform with respect to the initial conditions in $\mathcal{X}$ is required. This is relaxed for autonomous systems, as seen in [34, Definition 2].*

Under these mild assumptions, it was shown in [94] that, for any input u of interest, and for almost any controllable pair (D, F) of dimension $d_z := d_y(d_x + 1)$ with D a Hurwitz matrix, there exists a map $\mathcal{T}_u^*$ such that the following system is an

observer for (4.1)

$$\dot{z}(t) = Dz(t) + Fy(t) \tag{4.2a}$$
$$\hat{x}(t) = \mathcal{T}_u^*(t, z(t)). \tag{4.2b}$$

In other words, any trajectory of (4.2) verifies

$$\lim_{t \to +\infty} |\hat{x}(t) - x(t)| = 0,$$

and implementing (4.2) with any initial condition provides an estimate of the plant's state after a certain time.

The existence of $\mathcal{T}_u^*$ relies on the existence and injectivity of a direct transformation $\mathcal{T}_u : \mathbb{R} \times \mathbb{R}^{d_x} \to \mathbb{R}^{d_z}$ such that, for any solution x to (4.1), the image $z(t) = \mathcal{T}_u(t, x(t))$ evolves according to the dynamics (4.2a). Straightforward computations show that $\mathcal{T}_u$ must satisfy

$$\frac{\partial \mathcal{T}_u}{\partial x}(t,x) f(x, u(t)) + \frac{\partial \mathcal{T}_u}{\partial t}(t,x) = D\mathcal{T}_u(t,x) + Fh(x, u(t)), \tag{4.3}$$

for all $(t, x) \in [0, +\infty) \times \mathcal{X}$. According to [94], a solution to (4.3) always exists, however, it is difficult to show that $\mathcal{T}_u(t, \cdot)$ becomes injective after $\bar{t}$ defined in Assumption 2. For $t \geq \bar{t}$, $\mathcal{T}_u^*(t, \cdot)$ can then be designed as a left-inverse of $\mathcal{T}_u(t, \cdot)$. It is worth to stress that, in the particular case where the system (4.1) is autonomous, the transformation can also be taken autonomous, namely $\mathcal{T} : \mathbb{R}^{d_x} \to \mathbb{R}^{d_z}$ and $\mathcal{T}^* : \mathbb{R}^{d_z} \to \mathbb{R}^{d_x}$.

Although the observer existence is proven for a wide category of systems, its implementation requires the knowledge of the map $\mathcal{T}_u^*$. Unfortunately, an explicit expression is rarely available, unless a solution $\mathcal{T}_u$ to (4.3) is known, and building its left-inverse is possible. The goal of this chapter is therefore to develop a numerical methodology to compute this map $\mathcal{T}_u^*$ and, when needed, $\mathcal{T}_u$ and its Jacobian, for both autonomous and excited cases. This work relies on precise theoretical results of existence that are recalled in the next section.

4.2 Methodology

4.2.1 Learning Procedure: Autonomous Systems

Consider an autonomous system of the general form

$$\begin{cases} \dot{x}(t) &= f(x(t)) \\ y(t) &= h(x(t)) \end{cases}. \tag{4.4}$$

The existence of an autonomous transformation $\mathcal{T}^*$ is shown in the following Theorem, derived from [34].

Theorem 4.2.1 ([34]). *Suppose Assumptions 1 and 2 hold. Define $d_z = d_y(d_x + 1)$. Then, there exists $\ell > 0$ and a set S of zero measure in $\mathbb{C}^{d_z}$ such that for any $D \in \mathbb{R}^{d_z \times d_z}$ with eigenvalues $(\lambda_1, \ldots, \lambda_{d_z})$ in $\mathbb{C}^{d_z} \setminus S$ with $\Re\lambda_i < -\ell$, and any $F \in \mathbb{R}^{d_z \times d_x}$ such that (D, F) is controllable, there exists an injective mapping $\mathcal{T} : \mathbb{R}^{d_x} \to \mathbb{R}^{d_z}$ and a pseudo-inverse $\mathcal{T}^* : \mathbb{R}^{d_z} \to \mathbb{R}^{d_x}$, such that the trajectories of (4.4) remaining in $\mathcal{X}$ and any trajectory of*

$$\dot{z} = Dz + Fy, \tag{4.5}$$

satisfy

$$|z(t) - \mathcal{T}(x(t))| \leq M\,|z(0) - \mathcal{T}(x(0))|\,e^{-\lambda_{min}t}, \tag{4.6}$$

for some $M > 0$ *and with*

$$\lambda_{min} = \min\left\{|\Re\lambda_1|, \ldots, |\Re\lambda_{d_z}|\right\}, \tag{4.7}$$

and

$$\lim_{t\to+\infty} |x(t) - \mathcal{T}^*(z(t))| = 0. \tag{4.8}$$

Remark 2. *Notice that, if the observer is perfectly initialized, i.e.* $z(0) = \mathcal{T}(x(0))$*, then one has* $z(t) = \mathcal{T}(x(t))$ *and, consequently,* $x(t) = \mathcal{T}^*(z(t))$*,* $\forall t$*.*

The existence of the mappings being guaranteed by the previous theorem, a numerical computation is proposed to estimate $\mathcal{T}$ and $\mathcal{T}^*$ by generating a large set of (x, z) values, and using a nonlinear universal approximator. More precisely, the procedure is according to the following steps

1. choose of D and F matrix for the observer system (4.5) ;
2. choose a set of initial conditions (x_0, z_0) ;
3. simulate Equations (4.2a) and (4.4) in forward time, generating a set of (x, z) pairs ;
4. perform nonlinear regression to find the mapping $x = \mathcal{T}^*(z)$.

The detailed specific methods applied for each step and the rationale behind them is explained as follows.

Initial conditions The initial conditions affect the distribution in the (x, z)-space of the data used for performing the regression. Ideally, the sampling should be refined where the functions $\mathcal{T}$ and $\mathcal{T}^*$ are not smooth. However, in the absence of *a priori* knowledge on the transformations regularity, standard statistical sampling methods are used, such as Gaussian distributed sampling. It is worth to stress that the dynamics of the system of interest strongly modifies the initial distribution, in ways that cannot be predicted in advance. Therefore, the distribution of the actual $(x(t), z(t))$ data is expected to be very different from that of the initial condition.

Selection of data points The second step is the generation of simulation data with a numerical ODE solver over a finite time interval $[0, t_f]$, from the initial conditions chosen at the previous step. Such data must be pre-processed before it can be used on the nonlinear regression. Indeed, since $\mathcal{T}$ is unknown, it is impossible to initialize the observer exactly as suggested in Remark 2. Rather, the method relies on the stability of the observer and the fact that z "forgets" its initial condition. Then, inequality (4.6) suggests that it is reasonable to eliminate from the dataset the pairs $(x(t), z(t))$ for $t < \frac{k}{\lambda_{min}}$ with $k = 3$ or 5.

Nonlinear regression To learn the mappings $\mathcal{T}$ and $\mathcal{T}^*$, any nonlinear regression methodology could *a priori* be chosen. A neural network is proposed and further discussed in section 4.3, due to the simplicity of implementation and its ability to represent complex nonlinearities with a low number of parameters when compared to other methodologies [80].

4.2.2 Learning Procedure: system with an excitation

To account for excited systems, Theorem 4.2.1, in [94], was extended to general non-autonomous systems (4.1).

Theorem 4.2.2 ([94]). *Supposing Assumptions 1 and 2 hold with $\bar{t} \geq 0$. Define $d_z = d_y(d_x+1)$. Then, for any input u of interest, there exists a set S of zero measure in $\mathbb{C}^{d_z}$ such that for any Hurwitz matrix $D \in \mathbb{R}^{d_z \times d_z}$ with eigenvalues $(\lambda_1, \ldots, \lambda_{d_z})$ in $\mathbb{C}^{d_z} \setminus S$ with $\Re\lambda_i < 0$, and any $F \in \mathbb{R}^{d_z \times d_x}$ such that (D, F) is controllable, there exist mappings $\mathcal{T}_u : \mathbb{R} \times \mathbb{R}^{d_x} \to \mathbb{R}^{d_z}$ and $\mathcal{T}_u^* : \mathbb{R} \times \mathbb{R}^{d_z} \to \mathbb{R}^{d_x}$ such that*

1. *$\mathcal{T}_u(t,\cdot)$ and $\mathcal{T}_u^*(t,\cdot)$ depend only on the past values of u on $[0,t]$,*
2. *$\mathcal{T}_u(t,\cdot)$ is injective for all $t \geq \bar{t}$ with $\mathcal{T}_u^*(t,\cdot)$ a left-inverse on $\mathcal{X}$,*

and any trajectory of equations (4.4)-(4.5) with $x(t)$ remaining in $\mathcal{X}$ satisfies

$$|z(t) - \mathcal{T}_u(t, x(t))| \leq M\,|z(0) - \mathcal{T}_u(0, x(0))|\, e^{-\lambda_{min} t}, \tag{4.9}$$

for some $M > 0$ and λ_{min} defined as in (4.7) and

$$\lim_{t \to +\infty} |x(t) - \mathcal{T}_u^*(t, z(t))| = 0. \tag{4.10}$$

Theorem 4.2.2 differs from Theorem 4.2.1 only through the fact that $\mathcal{T}_u$ is time-varying and the eigenvalues no longer have to be sufficiently large. Quite expectedly, the time $\bar{t}$ after which $\mathcal{T}(t,\cdot)$ becomes injective is the same as the backward-distinguishability time of Assumption 2.

Estimating the map $\mathcal{T}_u^*$ is now more difficult, since it depends on the input u. In the favorable case where u is known in advance (time-varying systems), it is sufficient to learn the map $\mathcal{T}_u^*$ associated to such input u. Otherwise, consider the particular case of an input-affine system

$$\begin{cases} \dot{x}(t) = f(x(t)) + g(x(t))u(t) \\ y(t) = h(x(t)) \end{cases}, \tag{4.11}$$

and a nominal input u_0, such that Assumptions 1 and 2 hold. According to Theorem 4.2.2, there exists a map $\mathcal{T}_{u_0}$ which is solution to the PDE (4.3), with $u = u_0$ and $\mathcal{T}_{u_0}^*$ its left-inverse after a certain time. Then, straightforward computations show that along solutions to (4.11), $z(t) = \mathcal{T}_{u_0}(t, x(t))$ evolves according to

$$\dot{z}(t) = Dz(t) + Fy(t) + \Psi(t, z(t))(u(t) - u_0(t)), \tag{4.12}$$

where

$$\Psi(t,z) = \frac{\partial \mathcal{T}_{u_0}}{\partial x}\left(t, \mathcal{T}_{u_0}^*(t,z)\right) g\left(\mathcal{T}_{u_0}^*(t,z)\right)\ . \tag{4.13}$$

Similarly to the previous design, managing to estimate $z(t) = \mathcal{T}_{u_0}(t, x(t))$, enables then an estimation of $x(t)$, thanks to $\mathcal{T}_{u_0}^*(t, z(t))$. Moreover, when the term $\Psi(t,z)$ is absent, the dynamics of z are contracting, and it is sufficient to simulate z with any initial condition to obtain an estimate asymptotically. Unfortunately, this no longer holds when $\Psi(t,z)$ exists, and the new result is explained in the following

Corollary 4.2.1. *Suppose Assumptions 1 and 2 hold and pick u_0 among the inputs of interest. Assume D, $\mathcal{T}_{u_0}$ and $\mathcal{T}_{u_0}^*$ given by Theorem 4.2.2 are such that $\forall\, t$, $\forall\, z_a$, z_b,*

$$|\Psi(t, z_a) - \Psi(t, z_b)| \leq \mathcal{L}|z_a - z_b|\ .$$

If $\lambda_{min} > \mathcal{L}|u - u_0|_\infty$, *then any solution to* (4.1)–(4.12) *with* x *remaining in* $\mathcal{X}$ *verifies*

$$\lim_{t \to +\infty} \left| x(t) - \mathcal{T}^*_{u_0}(t, z(t)) \right| = 0 \,. \tag{4.14}$$

Proof : Denoting $e(t) = \mathcal{T}_{u_0}(t, x(t)) - z(t)$, compute the derivative of $e^\top e$ along trajectories. Then, apply the left-inverse $\mathcal{T}^*_{u_0}$. ■

However, such contraction condition comes with the setback that $\mathcal{T}_{u_0}$, and thus λ_{min} depend on the matrix D. Therefore, it may not be sufficient to chose D with λ_{min} sufficiently large. Indeed, if satisfying this condition is possible for a given input u, the plant can be observed for any other input u', such that $|u' - u_0|_\infty \leq |u - u_0|_\infty$. Therefore, the plant should be observable or at least detectable for any input. For instance, in [94, Theorem 4] it has been shown that when the plant is observable for any input and the drift system $\dot{x} = f(x)$ is differentially observable of order d_x, $\mathcal{L}$ can be bounded independently from λ_{min} and therefore, this observer also works with $u_0 = 0$ if λ_{min} is sufficiently large.

The proposed numerical methodology is as follows;

1. choose D and F for the observer system (4.5);
2. choose one initial condition (x_0, z_0);
3. choose an excitation $u = u_0$ to excite (4.11), such that $\dot{x} = f(x) + g(x)u_0(t)$;
4. simulate (4.2a),(4.11) with input u_0 in forward time, generating a set of (z, x, t) data points;
5. apply nonlinear regression to find the mapping $z = \mathcal{T}_{u_0}(x, t)$, and the associated left-inverse $x = \mathcal{T}^*_{u_0}(z, t)$;
6. compute $\partial \mathcal{T}_{u_0} / \partial x$ to find $\Psi(t, z)$ in Equation (4.12) ;
7. then, for validation, simulate (4.12), (4.11) in forward time with a different input $u(t) \neq u_0(t)$.

The specific details of the numerical methodology for each step and the rationale behind them are as follows.

Initial conditions and input signal For non-autonomous systems, the initial condition choice is not dominant on the distribution along the (x, z)-space of the data used to perform the regression. Indeed, the perturbation u has a much more significant impact. The question of finding an open-loop control u that generate 'rich' data is a classical question in system identification, and highly depends on the considered system. The objective, as in the autonomous case, is *a priori* to have many samples where the functions $\mathcal{T}$ and $\mathcal{T}^*$ are likely to be non-smooth. In the absence of intuition or *a priori* knowledge on these, the excitation should be chosen such that the system is led to explore as uniformly as possible the compact of interest.

Selection of data points and nonlinear regression The generation and preprocessing of data and the nonlinear regression methodology are identical as specified in section 4.2.1. In the next section, the regression method used to numerically learn the mappings is presented.



FIGURE 4.1: Neural network simplified flow chart.

4.3 Neural Networks

Here, a Neural Networks is applied to perform the nonlinear regression. It is worth to stress that any nonlinear regression method can potentially be applied to approximate the mappings. The basic architecture of the Neural Network is composed of one input layer with $l_i + bias$ neurons, multi-hidden layers with $l_h + bias$ neurons each, and one output layer with l_o neurons, as shown on Figure 4.1. The output value computed by the network is denoted $h_\Theta(x)$, and it depends on the input training values (x) and of the network weights (Θ). As base methodology to implementing a neural network model, this work refers to [80], [102], [103].

More specifically, each neuron of the neural network has some input and output data, which are balanced on means of importance of each characteristic of the learned system. Such nodes consider each input on a weighted form, balancing the importance of each for the prediction, and an activation function ($g(\Theta X)$) is used to decide to decide to fire or not the neuron.

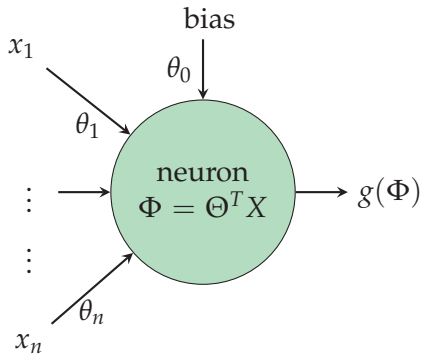


FIGURE 4.2: Neuron representation.

Mathematically, a neuron is expressed as follows. Let X and Θ be the vector form of all x_i, θ_i, $\forall i = 1 \dots n$, where n is the number of inputs of the neuron. Then, the weighted inputs fire or not the node by passing trough the activation function g.

$$\begin{aligned} \Theta^T &= [\theta_0, \theta_1, \theta_2, \cdots, \theta_n] \\ X^T &= [bias, x_1, x_2, \cdots, x_n]. \\ a &= g(\Theta^T X) \end{aligned} \tag{4.15}$$

One may note that, in one layer, there are several nodes, and each has a different related collection of weights. That being said, for a layer k, with l_k neurons, the Θ_k^T is represented by the following matrix;

$$\begin{bmatrix} \theta_0^{(1)} & \theta_0^{(2)} & \cdots & \theta_0^{(l_k)} \\ \theta_1^{(1)} & \theta_1^{(2)} & \cdots & \theta_1^{(l_k)} \\ \vdots & \vdots & \cdots & \vdots \\ \theta_n^{(1)} & \theta_n^{(2)} & \cdots & \theta_n^{(l_k)} \end{bmatrix}, \tag{4.16}$$

were each row corresponds to the weights related to a specific neuron on the layer k, and each column corresponds to an input, including the bias term which is expressed on the first column.

Moreover, given a training dataset with input and output values, the "learning" of the neural network weights is then performed. A cost function (J in $\mathbb{R}$) is used to provide a quantitative measure of the efficiency of the neural network with respect to a given training dataset [102]. This function can have different forms, and depend on the neural network weights (Θ), the training dataset output (Y), and the values predicted by the neural network ($h_\Theta(X)$). The objective here is to find a set of weights that minimizes the cost function, and better fits the training data. To that end, the back-propagation algorithm is applied. The back-propagation methodology and algorithm is detailed elsewhere [102], [103].

The goal of the back-propagation is to determine how changing of the weights of the neural network interferes on the cost function, and this is done by computing the partial derivatives of the cost function, $J(\Theta, h_\Theta(X), Y)$, with respect to any unit weight (j) at any layer (k) [102]. More precisely, $\partial J / \partial \theta_j^{(k)} \ \forall \ j = 0 \dots l_k$. For the back-propagation algorithm, if the neural network has N_L layers, $k = N_L$ is the output layer, and that the number of training examples is m. The algorithm is the following;

1. Define $\delta^{(k)}$ the error vector on the layer k, for all j.

   - For each output $k = N_L$:

   $$\delta^{(N_L)} = (a^{(N_L)} - y) \odot g'(\Phi^{(k)}).$$

   - For all the other layers $k = [N_L - 1, N_L - 2, \cdots, 2]$:

   $$\delta^{(k)} = (\Theta^{(k)})^T \delta^{(k+1)} \odot g'(\Phi^{(k)}),$$

   where $\Phi^{(k)} = \Theta^{(k)} a^k$ and $g'(\Phi)$ is the derivative of the activation function.

2. then, for each layer weights $\Theta^{(k)} \ \forall \ k \leq N_L$, compute the partial derivatives;

$$\frac{\partial}{\partial \Theta^{(k)}} J(\Theta, h_\Theta(X), Y) = \frac{1}{m} a^{(k)} \delta^{k+1}.$$

It is worth to stress that, for the back-propagation to work, some assumptions on the cost function are needed [102]; (1) it can be written as an average $J = 1/m \sum_{i=1}^{m} J_i$ of cost functions (J_i) for individual training examples, which enables the computation of partial derivatives for each single training example, and (2) it can be written as a function of the outputs from the neural network, and thus is a function of the output activation.

4.3.1 Proposed Neural Network Methodology

In this work, the neural network architecture is composed of four layers $(N_L = 4)$: one input (layer (1)), two hidden layers (layers $(2, 3)$), and one output (layer (4)). The number of nodes of the input and output layers depends on the transformation of interest, which are, respectively, d_x and d_y when the the approximation of $\mathcal{T}$ is needed, and the opposite when $\mathcal{T}^*$ is needed. Both hidden layers have 25 units each, which was chosen by trial-and-error, trading-off computational effort against accuracy. For the sake of brevity, this trade of study is not detailed here. The following quadratic cost function is used

$$J_\theta = \frac{1}{2m}\sum_{i=1}^{m}\sum_{k=1}^{l_4}(h_\theta(x_k^i) - y_k^i)^2, \tag{4.17}$$

where m is the number of training data, l_4 is the number of nodes on the output layer ($N_L = 4$), and h_θ is the neural network predicted value. Again, one must keep in mind that this particular choice has been made on a trial-and-error analysis, and is by no means optimal in any sense.

The activation function varies for each layer k. For instance, the activation of the first layer is the input value (x) for the system of interest, plus a bias ($a_0 = 1$), such that; $a^{(1)} = [a_0, x_1, \cdots, x_n]^T$. The hidden layers have the hyperbolic tangent (tanh) as activation function $g(\Phi)$, where Φ is the layer weighted input, as shown in (4.18). However, a linear function is used at the output, i.e., each of the fourth neurons layer has the value multiplied by its respective weight.

$$g(\Phi) = 2\left(\frac{1}{1+e^{-2\Phi}}\right) - 1, \qquad g'(\Phi) = 1 - g(\Phi)^2. \tag{4.18}$$

More precisely, the training methodology is:

1. randomly initialize the weights of each layer k, where $\Theta^k \in \mathbb{R}^{l_{k+1}\times(l_k+1)}$, $\forall k \leq (N_L - 1)$, and define the three Θ matrices necessary for computation, $\Theta^{(1)} \in \mathbb{R}^{l_1\times 26}$, $\Theta^{(2)} \in \mathbb{R}^{25\times 26}$ and $\Theta^{(3)} \in \mathbb{R}^{l_4\times 26}$;

2. effect forward propagation to compute first prediction for $h_\Theta(x)$, as follows;

$$\begin{aligned} a^{(1)} &\rightarrow inputs + bias, \\ \Phi^{(2)} &= \Theta^{(1)}a^{(1)}, \\ a^{(2)} &= [a_0, g(\Phi^{(2)})], \\ \Phi^{(3)} &= \Theta^{(2)}a^{(2)}, \\ a^{(3)} &= [a_0, g(\Phi^{(3)})], \\ \Phi^{(4)} &= \Theta^{(3)}a^{(3)}, \\ h_\Theta(x) &= \Phi^{(4)}. \end{aligned} \tag{4.19}$$

3. compute the cost function (4.17) with respect to $h_\Theta(x)$, and the training output values Y.

4. use the back-propagation methodology to compute the partial derivatives of the cost function; $\frac{\partial}{\partial\Theta_i^{(k)}}J(\Theta, h_\Theta(X), Y)$.

5. apply the optimization method ($fmincg$ ©[1]) with the back-propagation to minimize the cost function and determine the optimal neural network weights Θ.

Optimization method The $fmincg$ function ©[2] is an optimization routine to minimize a continuous differentiable multivariate function. The initial condition is given by the ensemble of weight values of the neural network, arranged at a $(n_w \times 1)$ vector, where n_w is the number of weights. The optimization is performed over

[1] Copyright (C) 2001 and 2002 by Carl Edward Rasmussen. Date 2002-02-13
[2] Copyright (C) 2001 and 2002 by Carl Edward Rasmussen. Date 2002-02-13

such weights, by minimizing the cost function (Equation (4.17)). The Polack-Ribiere method of conjugate gradients is applied to define search directions. A quadratic and cubic polynomial approximations is used for line search and the Wolfe-Powell stopping criteria coupled with the slope ratio method is used to guess the initial step sizes. It is worth to stress that other optimization methods could be used here, but impact of those is not the object of study of this work, as so, only $fmincg$ is applied.

In the next section, such methodology is applied to compute the transformation $\mathcal{T}_u$ and $\mathcal{T}_u^*$ of the previously presented Luenberger observer. Two neural networks are learned to solving the system of interest; (a) one to solve $z = \mathcal{T}_u(x)$, with the nonlinear system x as input and the observer system z as output, and (b) one other with the observer as input and the nonlinear system as output, solving $x = \mathcal{T}_u^*(z)$.

4.4 Numerical simulation

In this section, the proposed approach is illustrated via numerical simulations on toy problems. The main goal is to qualitatively highlight how the data selection and processing impacts the observer performance for autonomous and excited systems.

4.4.1 Autonomous System

Lets consider the following system

$$f(x) = \begin{cases} \dot{x}_1 = x_2^3, \\ \dot{x}_2 = -x_1 \end{cases} \quad y = x_1 \tag{4.20}$$

which admits bounded trajectories (where $x_1^2 + x_2^4$ is constant). This system is weakly differentially observable of order 2 in $\mathbb{R}^2$, since the mapping $x \to \mathrm{H}_2(x) = (x_1, x_2^3)$ is injective on $\mathbb{R}^2$, and so, it is considered *a fortiori* instantaneously backward distinguishable [34], [94]. Applying the Luenberger's methodology presented in section 4.2.1, for the observer (4.2) in $\mathbb{R}^3$, with $D = diag([\lambda_1, \lambda_2, \lambda_3])$ and $F = \begin{pmatrix} 1 \\ 1 \\ 1 \end{pmatrix}$, the necessary mappings are computed.

The training data is generated for several sets of initial conditions, chosen with different sampling methods. The system and observer dynamics are solved over a time interval $[0, t_f]$, with $t_f = 50\ s$ and a time step $\Delta t = 10^{-2}\ s$. In order to improve the neural network behavior, the data is centered around zero and normalized. The approximation of the transformation $x = \mathcal{T}^*(z)$ is then computed with the neural network methodology presented in Section 4.3.1, where the input is $z = (z_1, z_2, z_3)$, and the output is $x = (x_1, x_2)$. A maximum of 1000 iterations is used.

The impact of varying the design choices for the solution is highlighted in the following paragraphs.

Impact of the size of the set $\mathcal{O}$

One of the critical design choices lies on the size of the state-space subset where the mappings are approximated, such that all the subset might contain training data samples to train the neural network. Nevertheless, an inherent trade-off exists: ideally, the choice of set should be as large as possible, but this requires more training

data and, most importantly, a more accurate nonlinear approximator for the mappings. Such choice is therefore linked to the complexity of the neural network and to the number of points in the training dataset. For a fixed architecture, covering a larger set usually has a negative impact on accuracy. The trade-off between the set size and the number of training data samples is illustrated on Figure 4.3, where the same number of points in the training dataset are used for two different sets $\mathcal{O}$. Each figure presents the plot of the training dataset and the asymptotic logarithmic relative error

$$\lim_{t\to\infty} \log \frac{(x_1(t) - \hat{x}_1(t))^2 + (x_2(t) - \hat{x}_2(t))^2}{x_1^2 + x_2^2}. \tag{4.21}$$

Unsurprisingly, both learned mappings have a better qualitative performance in the regions where more training data points are placed. As already known from classic regression methodologies, the extrapolation capabilities are extremely limited, as illustrated by the high error region far from the origin, on Figure 4.3b. This figure also illustrates the difficulty of estimating the mapping $\mathcal{T}^*$ around two symmetrical points close to the origin. This phenomena, in theory, is linked to a small modulus of injectivity for $\mathcal{T}$, which is depicted on Figure 4.4, around $(x_1, x_2) = (0, 0)$.

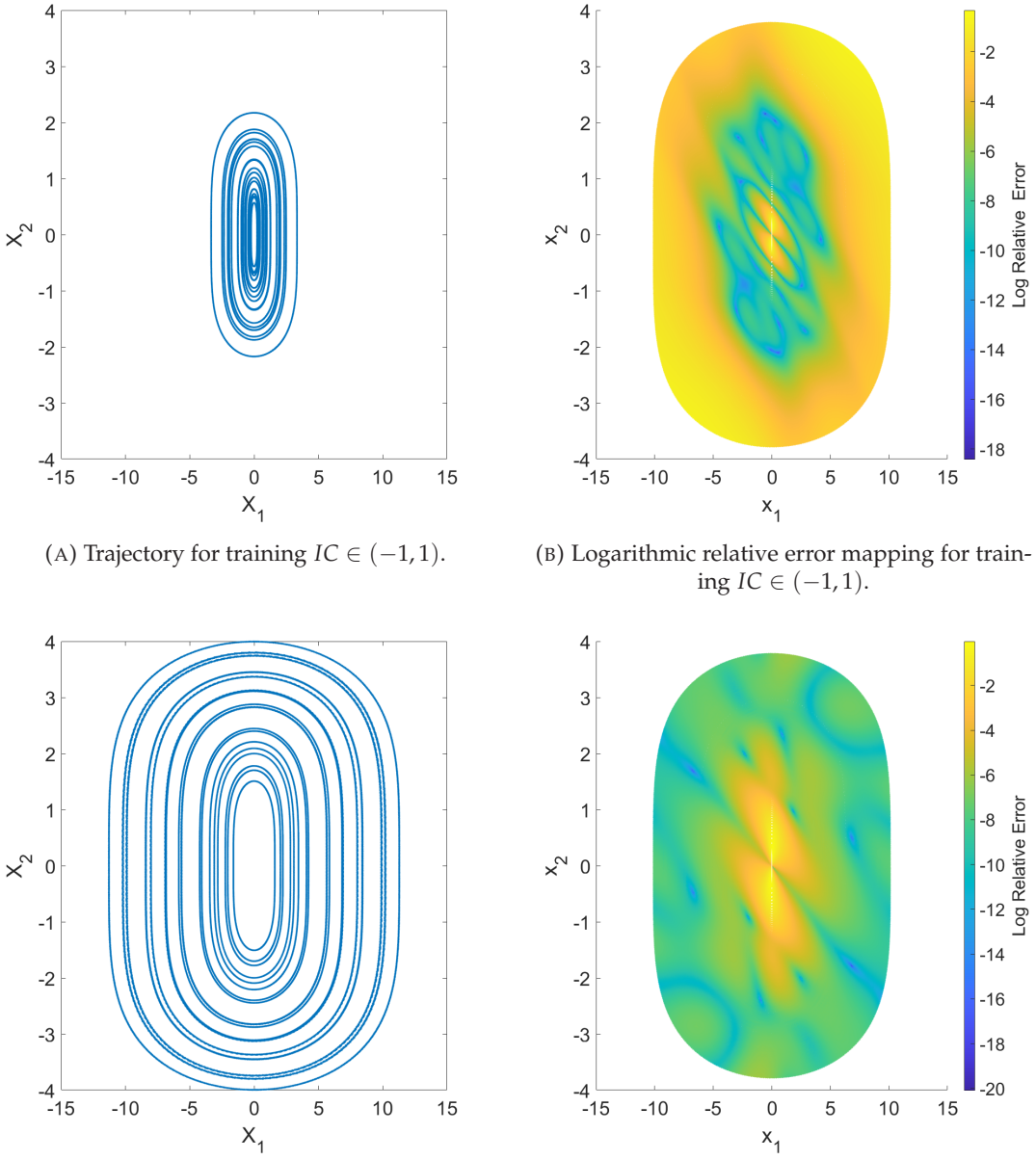
Moreover, as an attempt to increase the efficiency of the prediction over the larger set, the increase of the number of neurons at the neural network hidden layers, or/and the number of hidden layers would be suggested. Accordingly, an architecture with a larger (50) number of neurons has been tested, however, no remarkable difference has been found on the tested case, such that, for the sake of brevity, the results are not shown here.

Impact of the initial condition sampling

Regarding the distribution of the initial conditions, this section compares and discuss the impact of using different statistic methods to choose the initial condition distribution, and the impact of varying the number of data points in the training set given for the learning.

Distribution Different well known standard methods for sampling distribution can be used to choose the initial conditions for the neural network training set of data. Here, in a fixed $[x_1, x_2]$ range of $[-10, 10]$, the impact of using a Gaussian distributed and a regular spaced distribution are shown. Figures 4.3c and 4.3d present the Gaussian distribution trajectory and resultant error, whereas Figures 4.5a, 4.5b, present the regular spaced results. Both methods are applied for a training sample of 20 initial conditions.

Regarding the different distribution methods used to fill the parametric space of initial conditions, small differences are encountered. Comparing the trajectories for Gaussian distribution with the regular partitioning (Figures 4.3c and 4.5a, respectivelly), it is visible that the training trajectories have different distribution on the space; the first one presents several trajectories that better fill the space, whereas the second one presents dynamics that seem to converge to a similar trajectory, such that empty gaps are seen in the parametric space. Regarding the logarithmic relative error, in general, the same behavior from the Gaussian distribution, Figure 4.3b, is seen in the regular partition, Figure 4.5b. Both distributions result presents high error when predicting trajectories closer to $(x_1, x_2) = (0, 0)$, however, the regular



(A) Trajectory for training $IC \in (-1, 1)$.

(B) Logarithmic relative error mapping for training $IC \in (-1, 1)$.

(C) Trajectory for training $IC \in (-10, 10)$.

(D) Logarithmic relative error mapping for training $IC \in (-10, 10)$.

FIGURE 4.3: Impact of the size of the compact: Comparison of the autonomous system (Equation (4.20)) solutions for an observer defined in $\mathbb{R}^3$, with a different range for the Gaussian distributed initial conditions. The prediction test is over 100 equally distributed initial condition $(x_{1,0}, x_{2,0}) \in [-10, 10]$.

distribution presents a slightly smaller region of high error when compared to the Gaussian method.

Number of points The impact of the initial conditions sampling is here tested by comparing the Luenberger proposed methodology with a training set computed over 20 and over 100 different initial condition, with $x_{0,1} \in [-10, 10]$, chosen with a Gaussian distribution, and $x_2 = 0$. The corresponding result for 100 initial conditions is depicted in Figure 4.6.

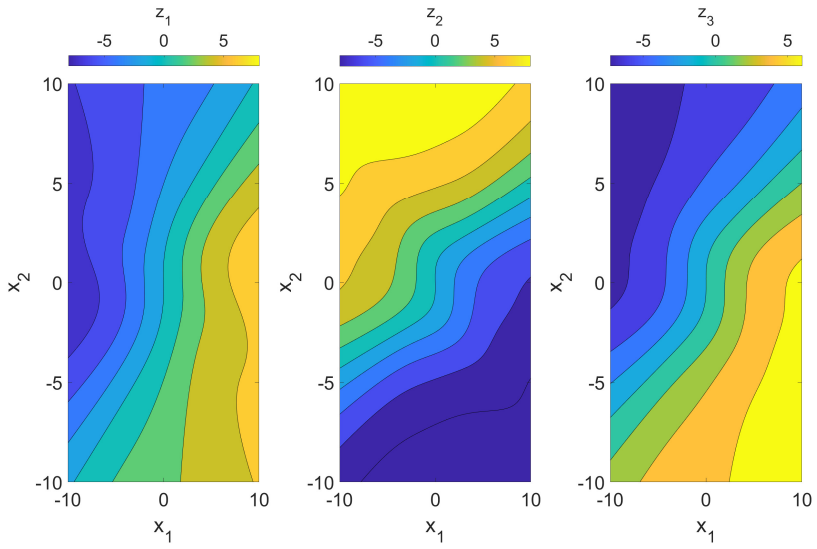


FIGURE 4.4: Transformation $\mathcal{T}$.

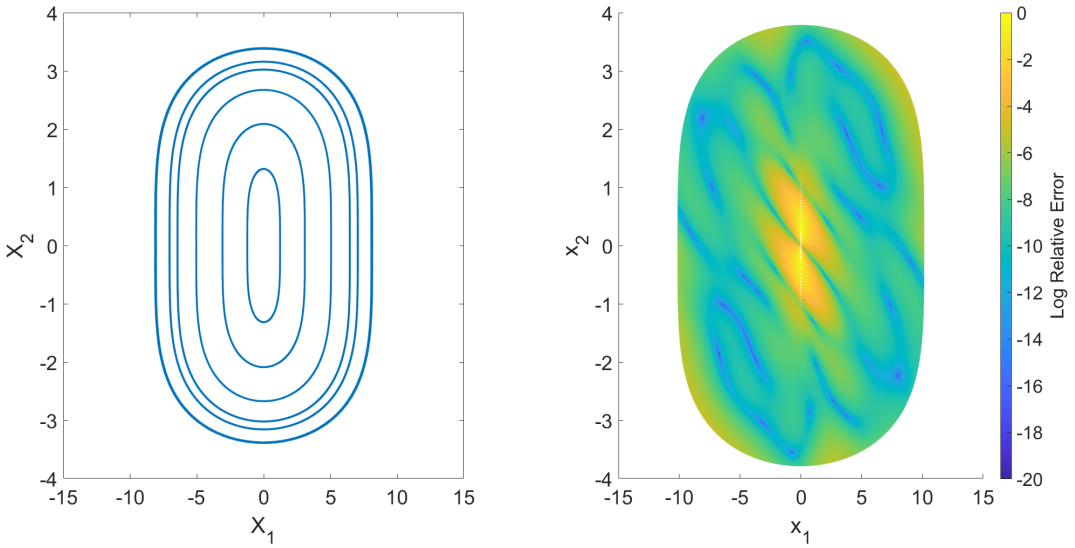
The use of a larger number of initial conditions better fills the training domain, as show on Figure 4.6a. However, this does not result in a significant quantitative accuracy improvement, only on a small reduction of the region of high error around $(x_1, x_2) = (0, 0)$. This point illustrates the need of further research on such neural network design options, i.e., for either a smarter way to chose the training trajectories of interest, e.g. by using mesh refining methods, or for larger scale brute force methods.

Impact of the observer eigenvalues

Another critical design choice lies in the value of eigenvalues of the Huirwtz matrix D on Equation (4.2). Those values are linked to the convergence speed of the observer, although they do not determine it entirely, as the mappings highly depend on their values. An study of the effect of D on, the noise filtering properties of the observer is given in [104], and can be taken for further information on the subject.

Here the study of the impact of the eigenvalues on the learning process is discussed. The comparison of the results obtained with, first, 'arbitrarily' chosen eigenvalues $(-5, -6, -7)$ and, second, eigenvalues corresponding to a third-order Bessel filter, with a cut-off frequency of 2π rad/s. The results for either cases are depicted on Figure 4.7. Although these results are very partial, and a deeper study should be developed, they indicate that a physically sound choice of eigenvalues eases the learning process, for a similar convergence speed, since the dynamic of the observer is imposed by the frequency.

Is is worth to stress that a future works should include a deeper study of the impact of the choice of the eigenvalues on the transformation and the learning process, and how it affect the observer convergence speed. Also, another interesting research direction for this topic would be to perform nonlinear regression, in the state space, observer variables and on the eigenvalues, such that no eigenvalue choice would be necessary. For example, one could envision finding an approximation of $\mathcal{T}^*(z, \omega_c)$, where ω_c is the cut-off frequency of the Bessel filter.



(A) Trajectory for $IC \in (-10, 10)$.

(B) Logarithmic relative error mapping for $IC \in (-10, 10)$.

FIGURE 4.5: Solution for the autonomous system (eq. (4.20)) with an observer z defined in $\mathbb{R}^3$, with regular partition used for choosing the 20 initial conditions $(x_{1,0}, x_{2,0}) \in (-10, 10)$.

4.4.2 Non-autonomous System: Van der Pol

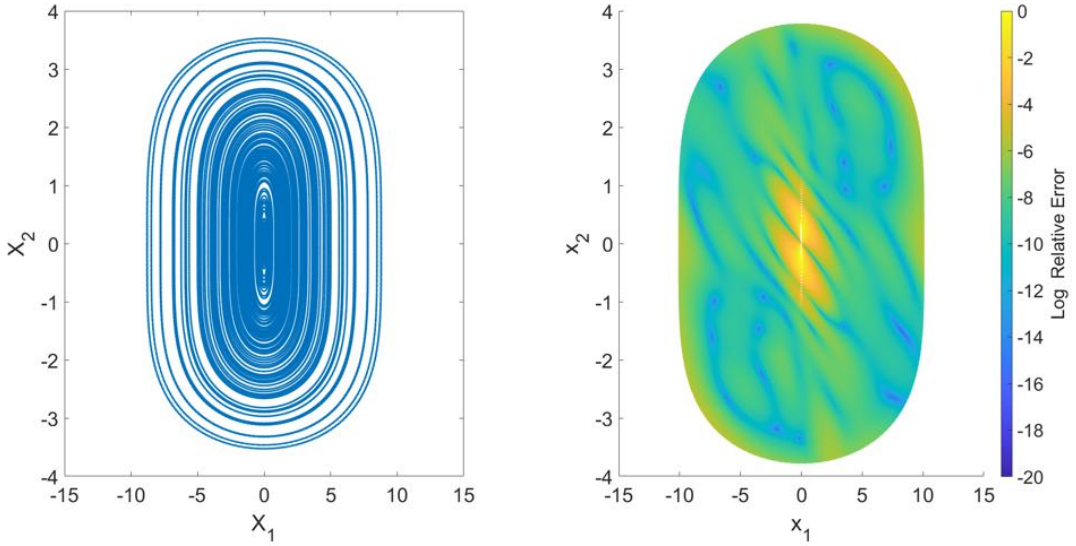
For the non-autonomous system, lets consider the following Van der Pol oscillator as a first example, which is a non-conservative oscillator with nonlinear damping [105]

$$f(x) = \begin{cases} \dot{x}_1 = x_2 \\ \dot{x}_2 = \epsilon(1 - x_1^2)x_2 - x_1 + u(t) \end{cases}, \quad y = x_1, \tag{4.22}$$

where $\epsilon = 1$. When unforced, its trajectories quickly converge to a single asymptotically stable limit cycle, but it exhibits chaotic behavior under sinusoidal forcing. These properties perfectly illustrate how the approach described in Section 4.2.2 significantly improves on the result presented in [94, Section IV]. In that paper it is suggested that, for systems of the form (4.11), the autonomous transformation corresponding to f only, should be used for an observer with sufficiently fast convergence[3]. This strategy is extremely difficult to apply to the Van der Pol oscillator, since the generated data without forcing would be clustered around the attractive limit cycle. Rather, here a linear chirp function is applied to generate the training set, with $\omega_0(t) = 10^{-3} + 9.99 \times 10^{-5} t$, such that the system extensively explores the (x_1, x_2)-plane. Then, the corresponding transformation $\mathcal{T}_{u_0}^*$ is used in an observer of the form (4.12) to estimate the states under a different harmonic forcing $u(t) = 0.44 \cos(0.5t)$. The results corresponding to an observer z evolving in $\mathbb{R}^3$ and $\mathbb{R}^5$, respectively, are shown in Figure 4.8.

On Figure 4.8 one may note that the corresponding plots show the system and the observer trajectories at a period of time between $5,000$ and $5,050$ s. This time span was chosen since the results for both observers show an asymptotic convergence performance, taking a long time to achieve convergence. Moreover, the prediction

[3] Which corresponds to taking $u_0 = 0$ in the approach here proposed.



(A) Trajectory for 100 $IC \in (-10, 10)$.

(B) Logarithmic relative error mapping for 100 $IC \in (-10, 10)$.

FIGURE 4.6: Solution for the autonomous system (Equation (4.20)) with an observer z defined in $\mathbb{R}^3$, with regular partition used for choosing the 100 initial conditions $(x_{1,0}, x_{2,0}) \in (-10, 10)$.

obtained for an observer in $\mathbb{R}^3$ (Figure 4.8a) presents an almost perfect fit for the prediction of trajectories, and increasing the observer to a dimension in $\mathbb{R}^5$ (Figure 4.8b) does not show remarkable improvements.

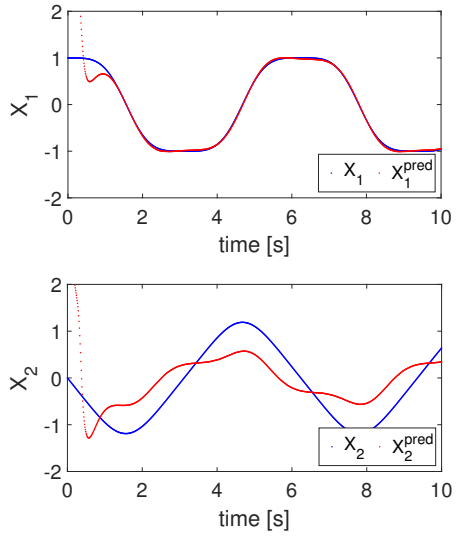
4.4.3 Non-autonomous System: Adding an input to (4.20)

For a second non-autonomous example, the same approach is applied to generate training data for system (4.20), by adding an excitation as

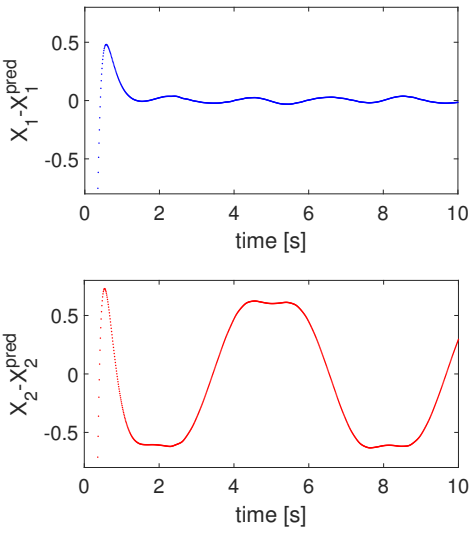
$$f(x) = \begin{cases} \dot{x}_1 = x_2^3 \\ \dot{x}_2 = -x_1 + u(t) \end{cases}, \quad y = x_1. \tag{4.23}$$

Then, the methodology presented in Section 4.2.2 is applied. First, the training data is generated for one initial condition and, again, the linear chirp function used in Section 4.4.2 as forcing $u(t)$. In this case, the observer is in $\mathbb{R}^3$, the Huirwtz matrix D corresponds to a third-order Bessel filter, with cut-off frequency $\omega = 2\pi\ rad/s$, and $F = \begin{pmatrix} 1 \\ 1 \\ 1 \end{pmatrix}$. The dynamics (4.20) are then solved using a built-in Matlab variable-step solver over $10^4\ s$. Nonlinear regression is applied to determine the transformations $(\mathcal{T}_{u_0}, \mathcal{T}^*_{u_0})$, as described in Section 4.3.1, which are then used with an observer of the form (4.12) for $u = 0$. The trajectories and error results for the pulsed and not pulsed systems are depicted in Figures 4.9 and 4.10, respectively.

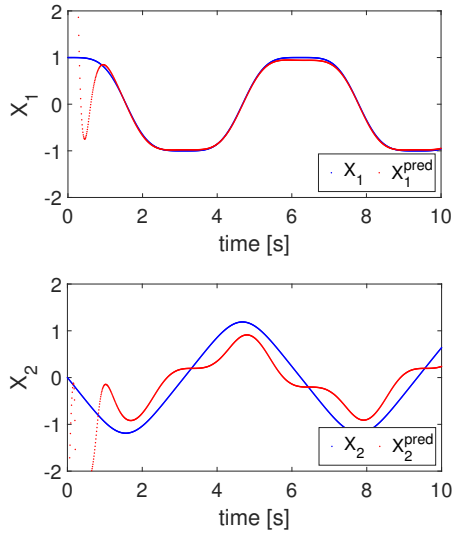
The use of the linear chirp to pulsate the system has a large impact on the distribution of training sample, such that the dynamic of the system vastly explores the set of system, as seen on Figure 4.9a. When compared to the autonomous solution, in Section 4.4.1, the chirp excitation makes the system better fill up the regions of interest (Figure 4.9a), than when a Gaussian distribution is used, for example, as shown on Figure 4.6a. Moreover, when comparing the logarithmic relative error, the forced



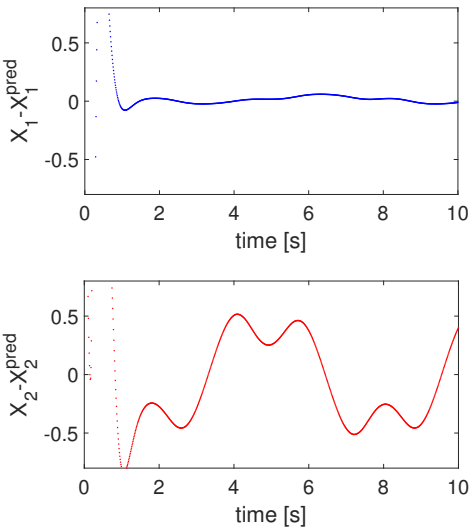
(A) States for $(\lambda_1, \lambda_2, \lambda_3) = -(5, 6, 7)$.



(B) Error for $(\lambda_1, \lambda_2, \lambda_3) = -(5, 6, 7)$.



(C) States for $(\lambda_1, \lambda_2, \lambda_3)$ the eigenvalues of a Bessel filter with cut-off frequency 2π rad/s.

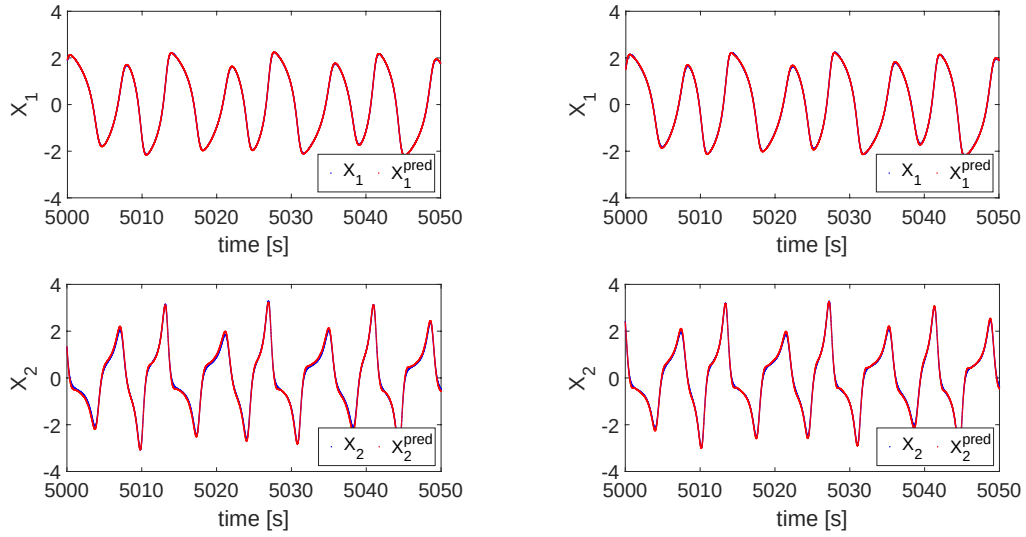


(D) Error for $(\lambda_1, \lambda_2, \lambda_3)$ the eigenvalues of a Bessel filter with cut-off frequency 2π rad/s.

FIGURE 4.7: Evolution of the true and estimated states over time of the autonomous system (Equation (4.20)) for an observer defined in $\mathbb{R}^3$, with different eigenvalues.

system (Figure 4.9b) presents a smoother field than the autonomous case, e.g., given on Figure 4.6b. Also, a remarkable decrease on the size of high error region, around $[x_1, x_2] = [0, 0]$, is seen when the system is pulsed.

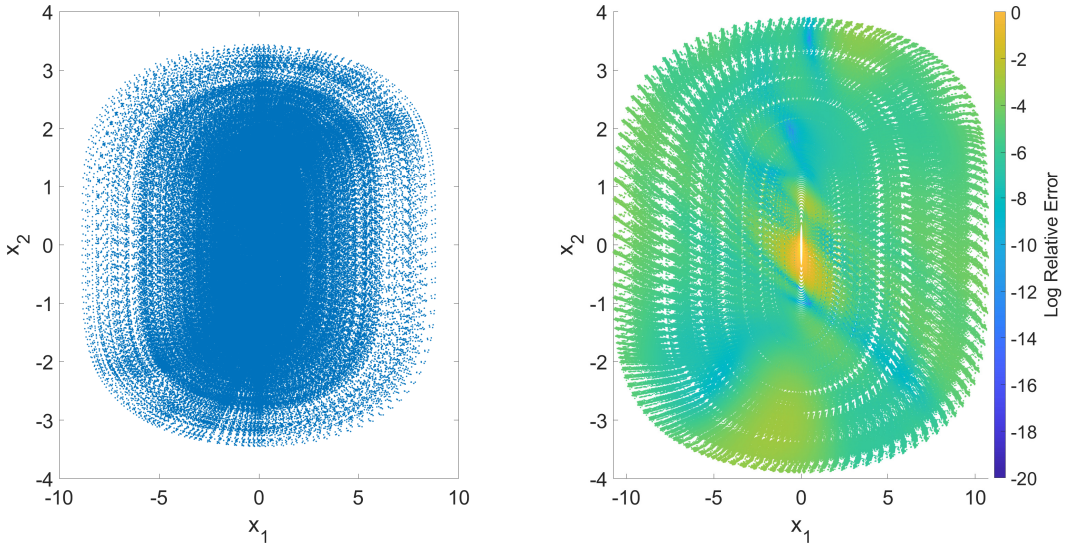
To validate the model, the system was also simulated for $u(t) = 0$, i.e., without excitation. Figure 4.10 shows that the observer has an asymptotic convergence for both states (x_1, x_2), after a transient period of 100 s, obtaining a 0 average error after that, as Figure 4.10b depicts. This behavior is an improvement on the observer, when compared to the autonomous result, e.g., presented in Section 4.4.1, since here the prediction of state x_2 is achieved with low error, giving a much better performance.



(A) Observer $z \in \mathbb{R}^3$.

(B) Observer $z \in \mathbb{R}^5$.

FIGURE 4.8: Evolution of the true and predicted states, showing the impact of the number of states of the observer on the performance of the design for the Van der Pol oscillator.



(A) Training trajectories.

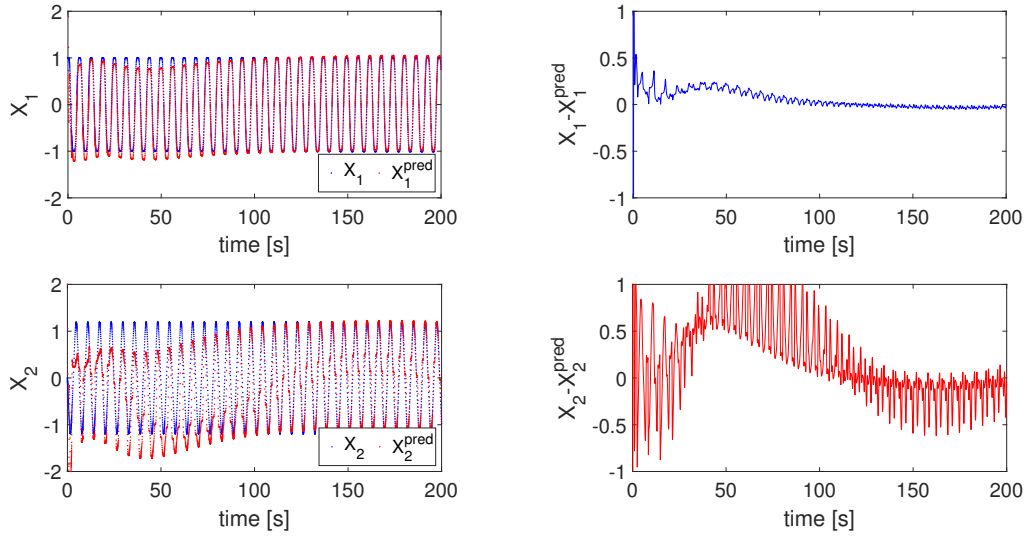
(B) Logarithmic relative error mapping for system with no excitation and $IC \in (-10, 10)$.

FIGURE 4.9: Training trajectories and estimation error for the artificially excited nonlinear oscillator.

4.4.4 Non-autonomous System: laminar flames

Now, for a more realistic application, the methodology is used to design an observer to predict the dynamic behavior of laminar flames. More precisely, we consider a model describing the dynamical behavior of a flame heat release $h(t)$ when subjected to inlet velocity variations $u(t)$.

Unfortunately, no such model could be found for the premixed flame of the previous chapters. This is most likely due to the small amount of input-data available



(A) Trajectories of system (4.23). (B) Prediction error.

FIGURE 4.10: Comparison and error of the prediction for trajectory with initial condition $(x_1, x_2) = (1, 0)$ and input $u(t) = 0$.

(due to the high computational burden of the CFD model) as well as the complexity of that flame. In particular, the presence of self-excited oscillations with a chaotic behavior makes the identification of a model of reasonable size a difficult problem, outside of the scope of this manuscript.

Nevertheless, we design an observer for a model of another laminar flame, with an equivalence ratio $\phi = 0.8$, anchored on a multi-slit burner, known as the Kornilov flame [106]. A ROM, based on data generated via computational fluid dynamics, is described in the next section. The data was generated with OpenFOAM [106], using a time step of 1 μs and a sampling time of 1 s. Figure 4.11 depicts the sample data, composed by the velocity and the heat release fluctuation.

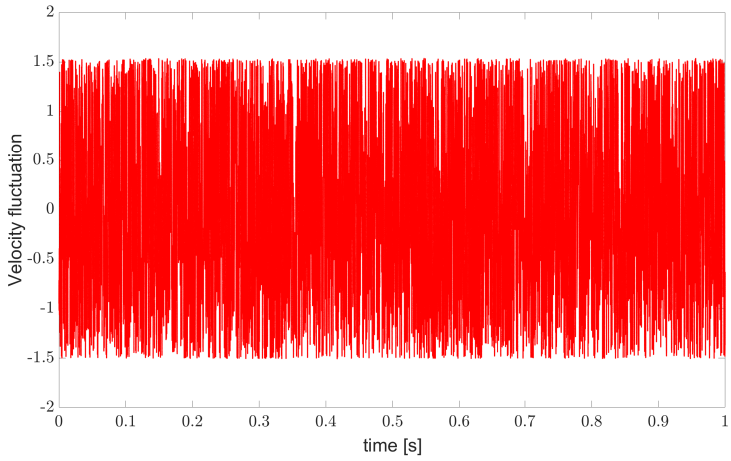
Now, a brief description of the modeling process is given.

Reduced Order Model of the Kornilov flame heat release dynamics

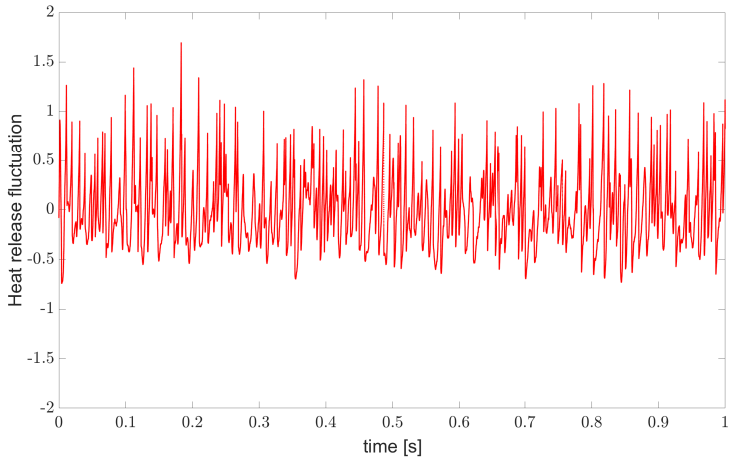
The model is derived by Ansys Twin Builder 2020 R2, a tool which performs input-output system identification for nonlinear systems. More precisely, given time-series of input and output data, the software relies on Deep Learning methods, standing between ARMAX [107] and NARX [108], to construct a dynamical system, taking the form of a set of Ordinary Differential Equations (ODE), that represents the data [109]. Figure 4.11 depicts the signals used as input (velocity fluctuations and their delayed version) and output (heat release from the flame). The input signal (Figure 4.11a) corresponds to a broadband signal. Similar to the ICF behavior, the Kornilov heat release fluctuation has sharp excursions in time domain, representing the nonlinear response of the flame due to the incoming excitation.

The model identified by Twin Builder, schematically represented in Figure 4.12, takes the following form

$$\dot{x}(t) = f(x(t)) + g(x(t))U(t)n, \qquad h(t) = x_5(t), \tag{4.24}$$



(A) $v(t)$.



(B) $h(t)$.

FIGURE 4.11: Kornilov flame training samples [106].

where f and g are non linear functions, h is the heat release, the state $x \in \mathbb{R}^5$ has five components, given as Dynamic ROM result, and the input has two components $U = (u(t), u(t-\tau))$, where $\tau = 150\ \mu s$ is imposed, as explained following.

Remark 3. *The choice of defining the input of the model as both the velocity fluctuations and a delayed version of it is based on flame models from the literature that feature similar terms, such as the n-tau model [110], the Neural Network model of [29] or the distributed delay model of [68]. The value of the delay is defined based on a trial-and-error study, not shown here for the sake of brevity.*

Generating training trajectories

Now the methodology presented in Section 4.2.2 can be applied coupled with the Dynamic ROM of the Kornilov flame. For that purpose it is necessary to choose the training trajectories such that the system travels over the whole compact of interest. However, this is not an easy task for such complex systems. Since the original Dynamic ROM is of high order ($\mathbb{R}^5$), classical visualization approaches become unfeasible. Then, the following sampling methodology is proposed;

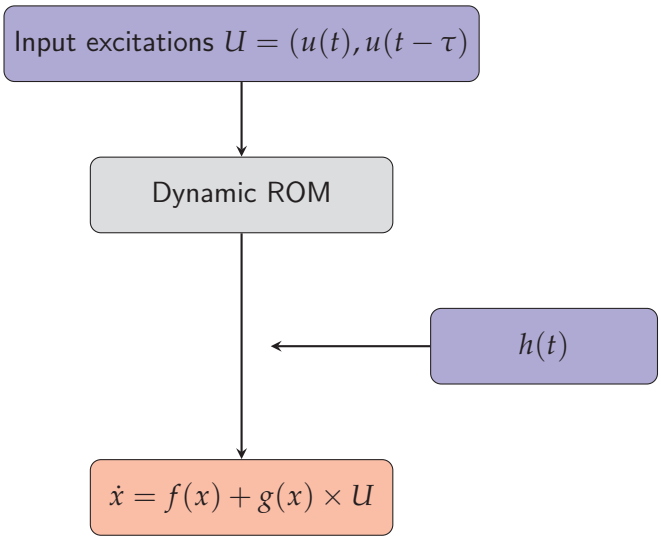


FIGURE 4.12: Dynamic ROM scheme.

1. Choose excitations ($U(t)$) to force the original system;
   - Single frequency harmonic signals
   - Broadband signals
2. Integrate $\dot{x}$ forward in time with the chosen excitations and extract the states x;
3. Integrate $f(x)$ backwards in time, using points along the obtained trajectory (x) as initial contrition and extract the states x_b;
4. Obtain the states x_b at the last instant of the backward simulation;
5. Simulate the system ($g(x)$) and the observer ($\dot{z}$ from Equation (4.11)) forward in time, with the last instant of the states x_b as initial condition;

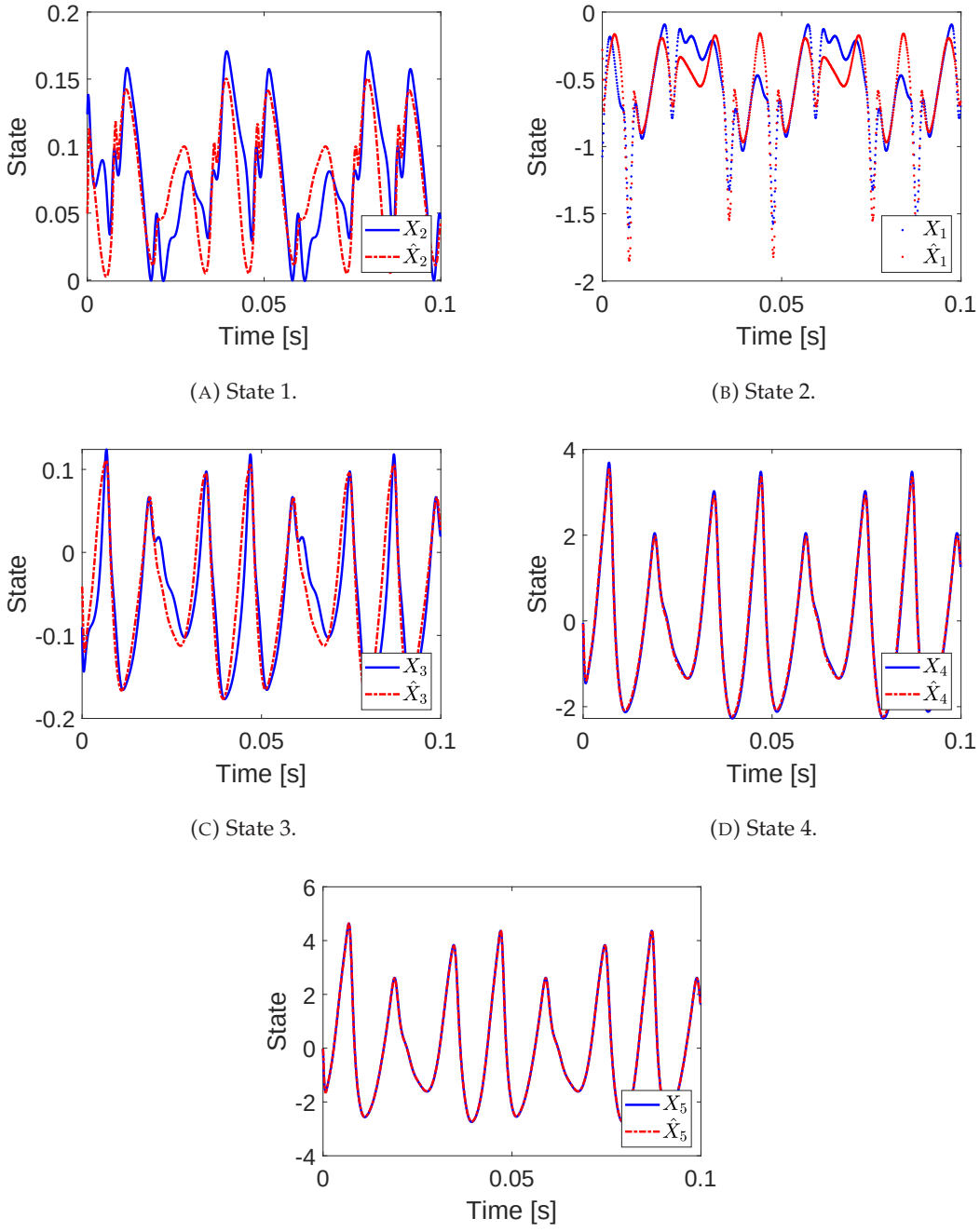
Moreover, the trajectories obtained at step 5 for the system and the observer (x, z) are then used as training trajectories for the forced observer methodology. Here, five different forcing frequencies and amplitudes are used as single frequency excitation, equally split between $[25, 300]$ Hz and $[0.5, 1.5]$, generating a total of 25 pulses. For the broadband excitation, 25 pulses are used, also varying from $[25, 300]$ Hz.

Validation

To validate the observer, the system is simulated for $u(t) = 0.4 \cdot sin(2\pi 100t) + 0.8 \cdot sin(2\pi 150t)$ and for a linear chirp excitation, with $\omega = 155 + 158t^2$, and the results are depicted on Figures 4.13 and 4.14, respectively.

As shown on Figure 4.13, the observer is able to predict the states of the system, but some states are harder than other. More precisely, the estimated states $\hat{x}_1$, $\hat{x}_2$ and $\hat{x}_3$ present higher error when compared to the trajectories, whereas the two last states presents an almost perfect fitting. It is worth to stress that, for this case, $h(t)$ depends only of $\hat{x}_5$, which means that the prediction of the system due to this pulse excitation has a good agreement.

The estimates due to a chirp excitation, however, have a larger error for states $\hat{x}_1$, $\hat{x}_2$ and $\hat{x}_3$, as shown in Figures 4.14a, 4.14b, 4.14c. It is seen that a close estimation is



(A) State 1.

(B) State 2.

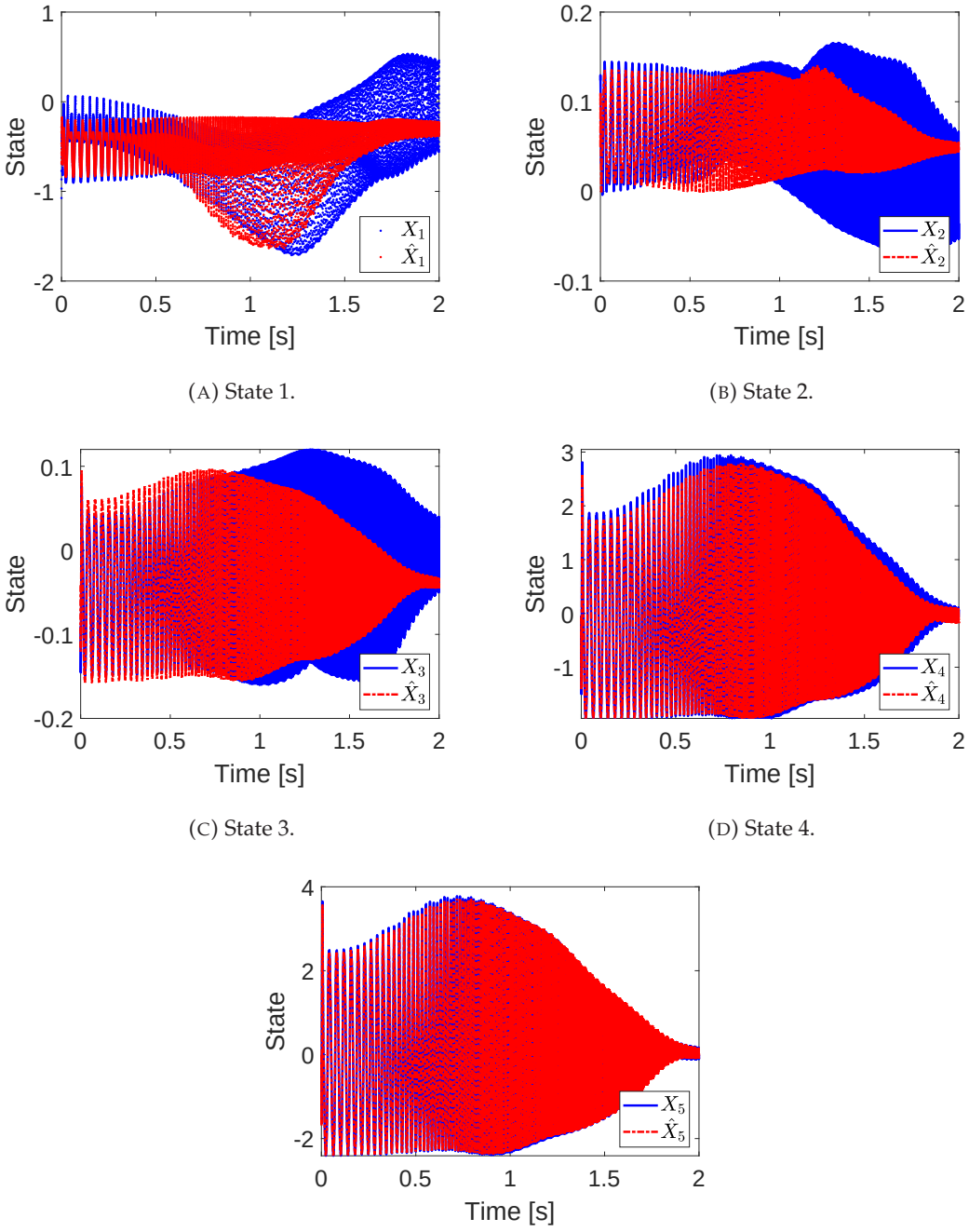
(C) State 3.

(D) State 4.

(E) State 5.

FIGURE 4.13: Comparison of the prediction for the trajectories with $u(t) = 0.4 \cdot sin(2\pi 100t) + 0.8 \cdot sin(2\pi 150t)$.

obtained for the beginning of the simulate ($t < 1$), but after that the error increases and the estimation derivatives from the original trajectories. This large error might happen because the chirp forcing takes the dynamic of the system out of the domain which was used for training the transformations. However, further research on this subject must be developed to fully understand such effect. Nevertheless, the estimations for $\hat{x}_4$, $\hat{x}_5$ also present an almost perfect agreement.



(A) State 1.

(B) State 2.

(C) State 3.

(D) State 4.

(E) State 5.

FIGURE 4.14: Comparison of the prediction for the trajectories with a linear chirp forcing.

4.5 Synthesis

This chapter presented a first step towards the usage of Luenberger observer theory coupled with simulation data-based Machine Learning to systematically design observers for complex nonlinear systems.

The application of the methodology proposed in this work for autonomous systems relies on the very mild assumption of backward distinguishability, which makes it quite general. The application of the methodology showed promising results, but

there are remaining questions which are two-fold. First, the generation of relevant data, which is briefly discussed in Section 4.2.1, should deserve further attention and study. For instance, a research on the impact of resampling the state-space after a first estimation of the mappings should be envisioned, that is similar to dynamic mesh refining techniques currently used in numerical simulations. However, this raises several issues regarding the refinement criteria. Second, the choice of method for nonlinear regression remains a fully open question, and here it was shown that the proposed Neural Network gives promising results, but it is by no means a definitive one.

When non-autonomous systems are of interest, the proposed methodology relies on stronger observability assumptions, somewhat equivalent to differential observability of the state order. This might be undesirable, however, it is necessary to ensure that the learning can be performed for a single nominal excitation, and that it can be extrapolated for other inputs. Indeed, it was shown in Sections 4.4.2 and 4.4.3 that choosing an appropriate nominal excitation that makes the system dynamic to completely explore the set of interest enables to obtain an observer that predicts the response for other different (or none) excitations. Relaxing such assumptions is a topic of future research. Another important aspect is the selection of the appropriate nominal excitation. Indeed, analogously to the autonomous case, the selection criterion used is paramount, with the added possibility here of steering the system towards regions of uncertainty. This problem is linked to active learning [111] and, more generally, input selection for identification [107], [112].

Chapter 5

Conclusions and Perspectives

This work presented the modeling of thermo-acoustic instabilities in a unstable laminar lean premixed flame. First, a high-fidelity CFD model was developped and used to compute the behavior of an inverted conical flame, both in steady-state and transient simulations. To incorporate methane-air combustion dynamics into Ansys Fluent, a 19 species skeletal kinetic mechanism was used. Then, a Reduced Order Model of the steady-state characteristics of steady ICF was derived based on CFD data, which enables the computation of various flame characteristics for a range of inlet velocities. Finally, a method to numerically design Luenberger observers for general non-linear systems was proposed.

The comparison of CFD simulation results with experimental results from the literature illustrates the accuracy of the model and its predictive capabilities. The use of a skeletal chemical kinetic mechanism resulted on a detailed model of the ICF time and space scales. However, to achieve precise results, an extremely refined mesh must be used, highly increasing the computational cost of simulations. It is, thus, unfeasible to use a linear regular mesh on the computational domain. Then a domain divided on different blocks is used, coupled with a mesh adaption tool, such that the characteristic mesh size varies for each block. The mesh refinement based on the temperature gradient enabled to decrease the mesh size on the reactive regions, where the flame front and tip are positioned, dynamically changing the mesh. However, the study of the refinement/coarsening adaption thresholds showed that there is a trade-off between reducing the simulation computational burden and the accuracy of the simulations. A flame dynamical analysis showed that a tight refinement threshold enables the characterization of the flame natural unstable behavior, even under external forcing, but still under high computational cost. If the refinement threshold is increased, the flame naturally unstable behavior is not evident when the flame is under external forcing, but the computational burden decreases. Although the mesh adaption tool decreases the burden linked to such simulations, it is still a remarkable computational cost, and other ways of optimizing such simulations are in the perspective of this work.

Moreover, the CFD model of ICF shows that the flame is naturally unstable, exhibiting self-excited oscillations under the simulated operating conditions. For this reason, the equilibrium computation fails to converge to a steady-state profile, and rather oscillates around a pseudo-steady state. To achieve an approximation of the equilibrium state of the ICF, statistic tools, such as ensemble averaging, and techniques as feedback control are considered for future work.

In view of predicting thermo-acoustic instabilities the computation of the Flame Transfer Function is achieved through a series of simulations under single frequency excitation. These presents satisfying results, since the computational and experimental results have an overall agreement. However, there is a high computational burden linked to simulating the flame response due to several excitations. To overcome

this problem, the modeling of the flame response due to a broadband excitation, such as a linear chirp, is envisaged, which could enable the of the FTF and the derivation of dynamical Reduced Order Models from a limited set of simulations, similarly to results from the literature [29]. The unstable nature of the flame dynamics makes this task a difficult one and is left for future work.

The steady ROM based on CFD data of the averaged steady-state of the ICF, however, yields less than 3% RMS error on the prediction of the velocity components and temperature. The ROM model presented a much lower computational cost when compared with the CFD models. Increasing the complexity of ROM of combustion systems based on CFD data is a perspective of this work. For instance, including other combustion properties into the modeling is envisaged, such as species mass fractions, providing a representation of all flame scales involved on the reactive process. An study of ROM of methane laminar diffusion flames is being developed in collaboration with the combustion laboratory at PUC-Rio. The analysis of adding different flame properties together and developing a ROM is on development, and will be soon published.

Regarding the Luenberger observer design, promising results were seen, both for autonomous and excited systems. The application of the methodology to estimate the states of thermo-acoustic instabilities on the so-called Kornilov flame gives low error for single frequency or simple excitations. When multi-frequency excitations are applied, the estimations present higher error. Such effect is caused by the state trajectories that leave the compact where the Luenberger transformations were trained, leading the observer design to a central question: How to properly choose the training data? There is a problem linked to the application of the designed observer to excitations that are different from the training one, since there is no guarantee that the new trajectories are inside of the training compact. This question becomes quickly more complex when non-autonomous systems of large dimension are of interest, since it is difficult to predict and visualize the transformations. A deeper study of such effect is envisaged.

Moreover, the Luenberger methodology is dependent of a dynamic formulation of the system of interest, which is often not available. The usage of the Dynamic ROM enables to obtain a set of ODE that represents the data, but the process is not straight forward and more research is envisaged. More specifically, the development of a Dynamic ROM of the ICF is now on search, but, since the behavior of the flame is unstable, such model is even more challenging, being then, the main perspective of this research.

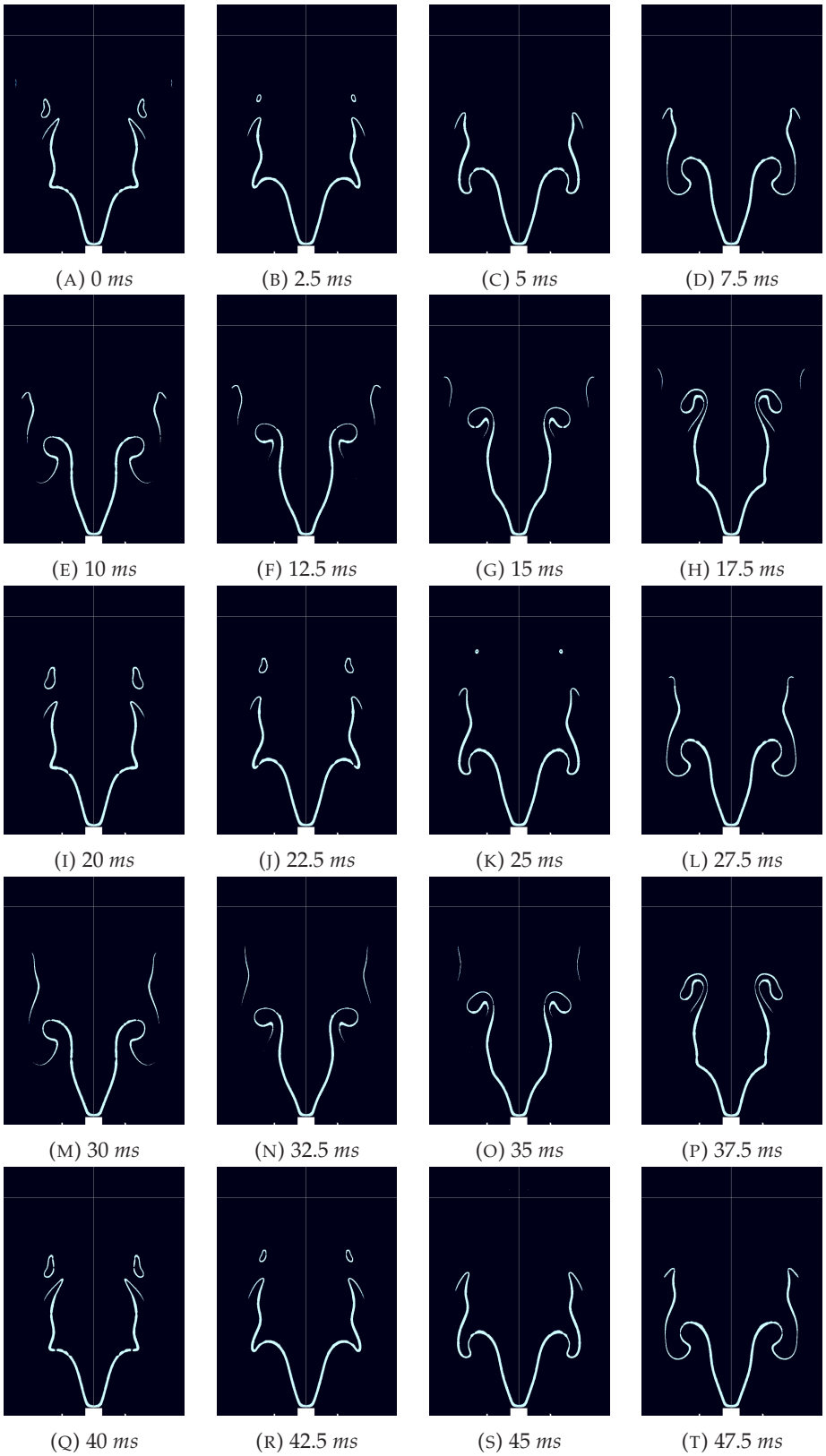
Appendix A

ICF Flame Front Complete Response Cycles

Ce chapitre présente des images supplémentaires de l'ICF excité modélisé, permettant la visualisation d'une période ou plus de tous les comportements harmoniques observés sur de telles flammes.

This chapter presents additional images of the modeled excited ICF, enabling the visualization of a period or more of all the harmonic behaviors seen on such flames.

Here a full cycle of the flame front response of the ICF under forcing is presented. Equally spaced instants of the flame front are shown, for a sampling period of 0.5 ms. The ICF response is depicted for the frequency excitations of 50, 75, 100, 125, 150, 172, 200 and 250 Hz. On these figures, the image interval enables to follow the complete flame front behavior, during several cycles, even for the high frequency excitation.



(A) 0 *ms* (B) 2.5 *ms* (C) 5 *ms* (D) 7.5 *ms*

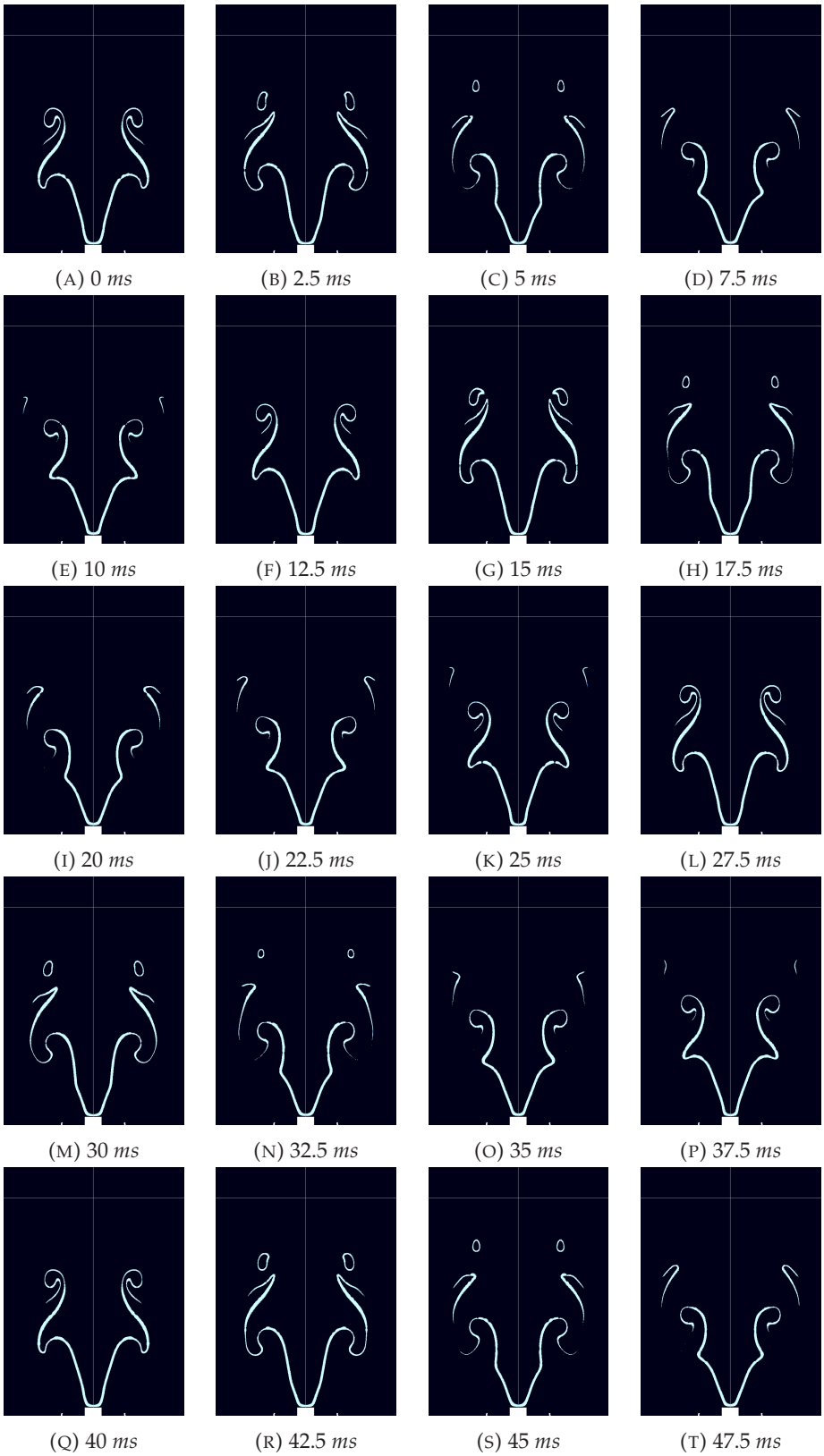
(E) 10 *ms* (F) 12.5 *ms* (G) 15 *ms* (H) 17.5 *ms*

(I) 20 *ms* (J) 22.5 *ms* (K) 25 *ms* (L) 27.5 *ms*

(M) 30 *ms* (N) 32.5 *ms* (O) 35 *ms* (P) 37.5 *ms*

(Q) 40 *ms* (R) 42.5 *ms* (S) 45 *ms* (T) 47.5 *ms*

FIGURE A.1: Forcing of 50 Hz with adaptation 50 K/m.



(A) 0 *ms* (B) 2.5 *ms* (C) 5 *ms* (D) 7.5 *ms*

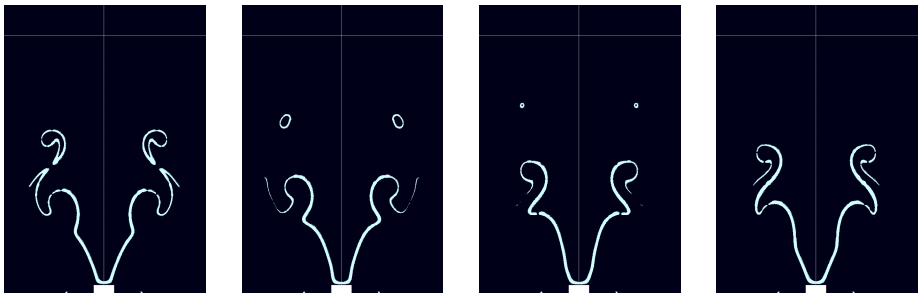
(E) 10 *ms* (F) 12.5 *ms* (G) 15 *ms* (H) 17.5 *ms*

(I) 20 *ms* (J) 22.5 *ms* (K) 25 *ms* (L) 27.5 *ms*

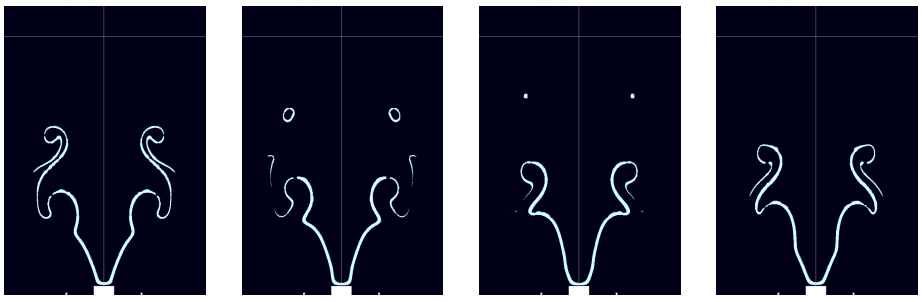
(M) 30 *ms* (N) 32.5 *ms* (O) 35 *ms* (P) 37.5 *ms*

(Q) 40 *ms* (R) 42.5 *ms* (S) 45 *ms* (T) 47.5 *ms*

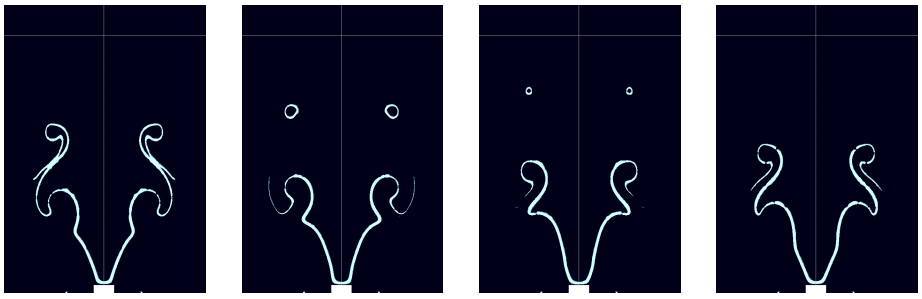
FIGURE A.2: Forcing of 75 Hz with adaptation 50 K/m.



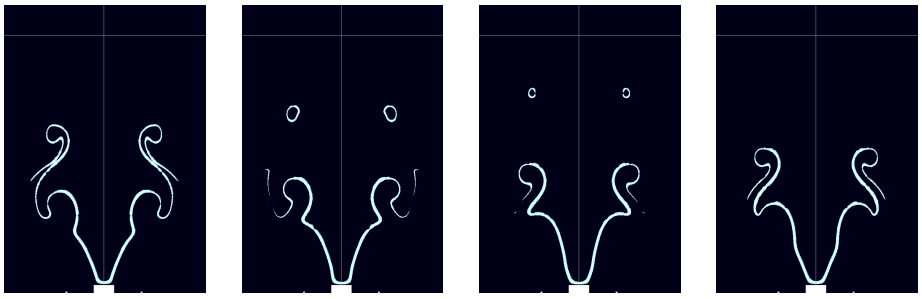
(A) 0 *ms* (B) 2.5 *ms* (C) 5 *ms* (D) 7.5 *ms*



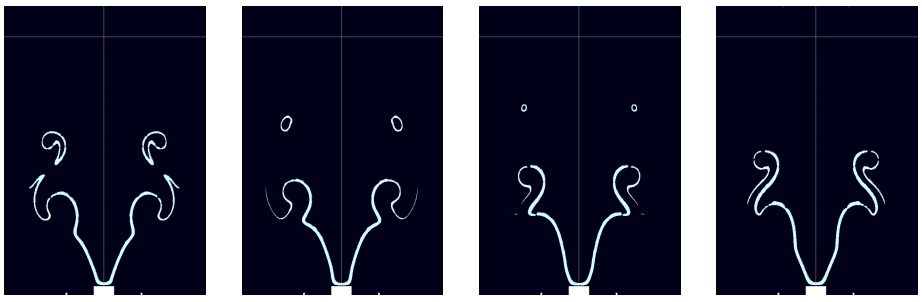
(E) 10 *ms* (F) 12.5 *ms* (G) 15 *ms* (H) 17.5 *ms*



(I) 20 *ms* (J) 22.5 *ms* (K) 25 *ms* (L) 27.5 *ms*

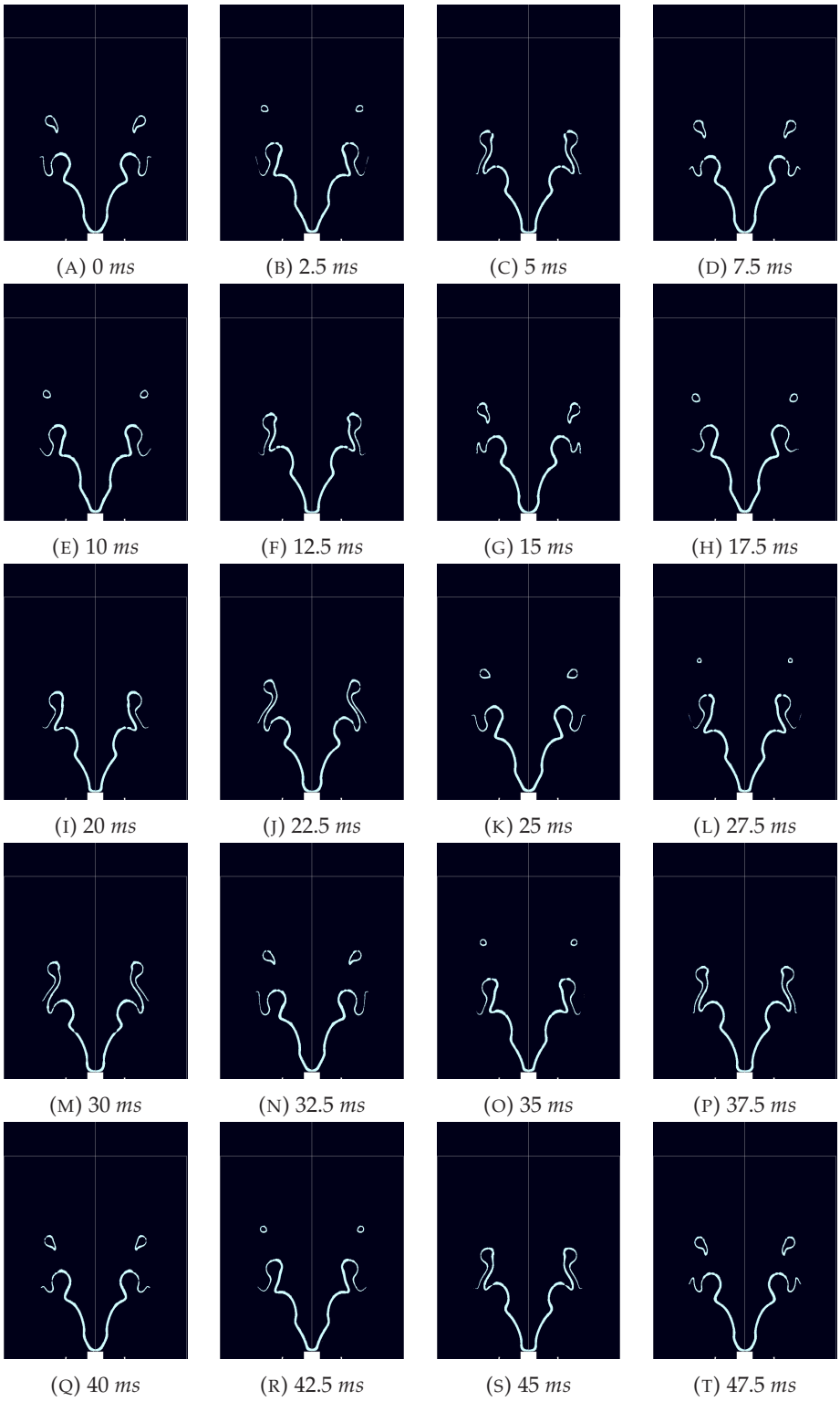


(M) 30 *ms* (N) 32.5 *ms* (O) 35 *ms* (P) 37.5 *ms*



(Q) 40 *ms* (R) 42.5 *ms* (S) 45 *ms* (T) 47.5 *ms*

FIGURE A.3: Forcing of 100 Hz with adaptation 50 K/m.



(A) 0 *ms* (B) 2.5 *ms* (C) 5 *ms* (D) 7.5 *ms*

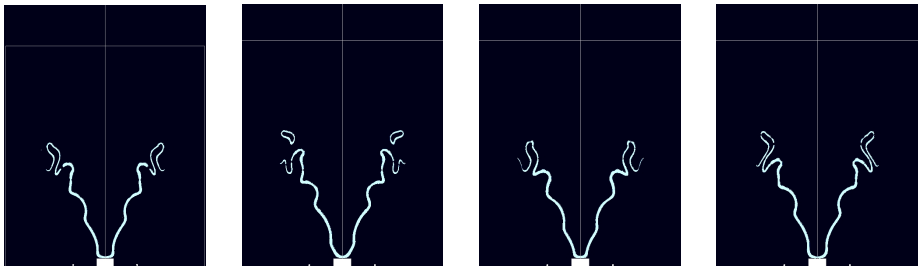
(E) 10 *ms* (F) 12.5 *ms* (G) 15 *ms* (H) 17.5 *ms*

(I) 20 *ms* (J) 22.5 *ms* (K) 25 *ms* (L) 27.5 *ms*

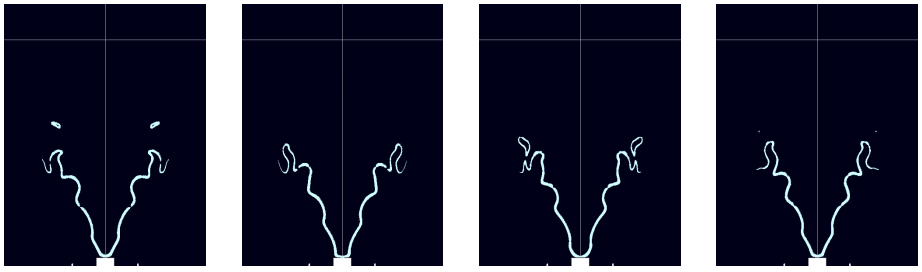
(M) 30 *ms* (N) 32.5 *ms* (O) 35 *ms* (P) 37.5 *ms*

(Q) 40 *ms* (R) 42.5 *ms* (S) 45 *ms* (T) 47.5 *ms*

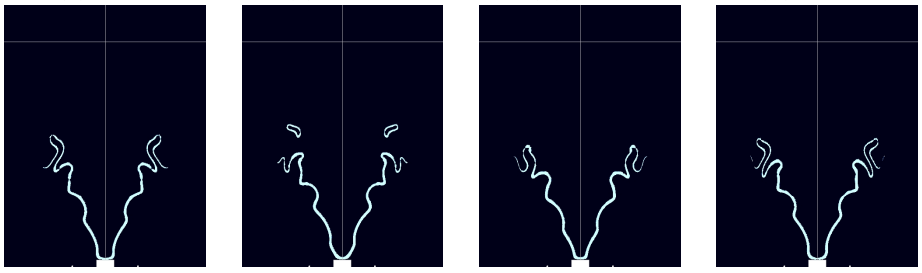
FIGURE A.4: Forcing of 125 Hz with adaptation 50 K/m.



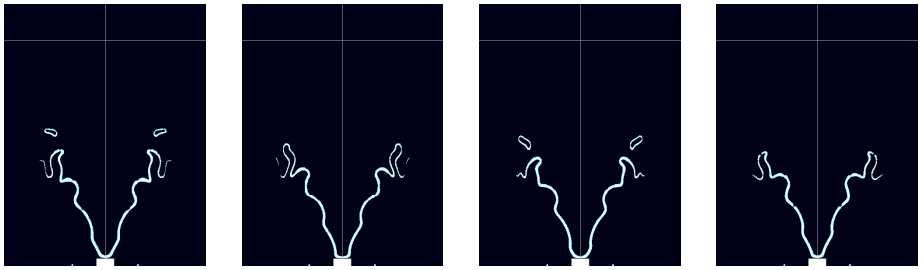
(A) 0 *ms* (B) 2.5 *ms* (C) 5 *ms* (D) 7.5 *ms*



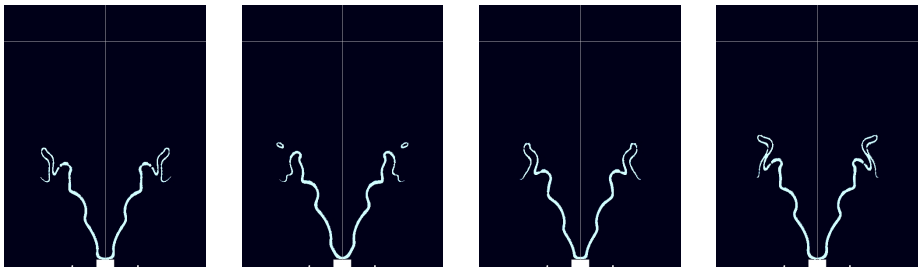
(E) 10 *ms* (F) 12.5 *ms* (G) 15 *ms* (H) 17.5 *ms*



(I) 20 *ms* (J) 22.5 *ms* (K) 25 *ms* (L) 27.5 *ms*

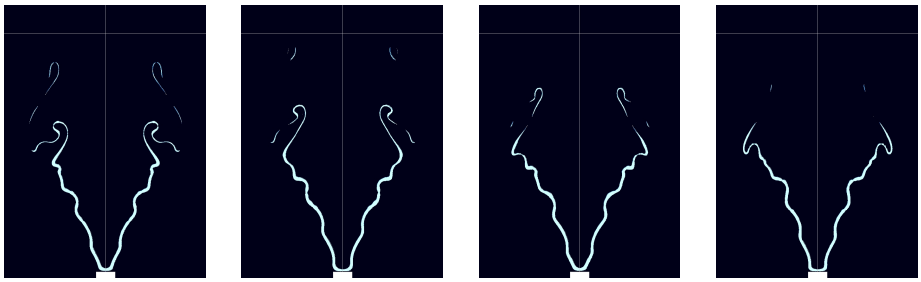


(M) 30 *ms* (N) 32.5 *ms* (O) 35 *ms* (P) 37.5 *ms*

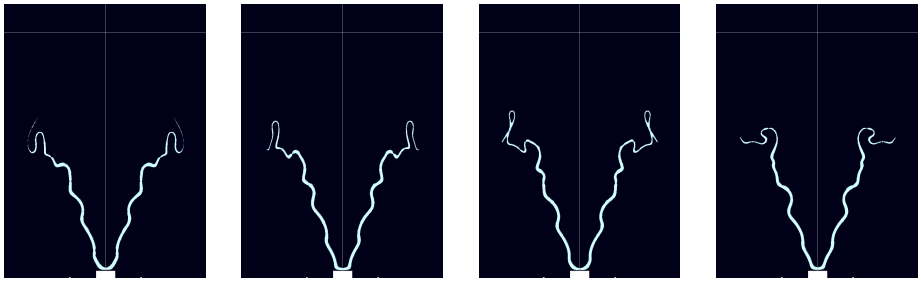


(Q) 40 *ms* (R) 42.5 *ms* (S) 45 *ms* (T) 47.5 *ms*

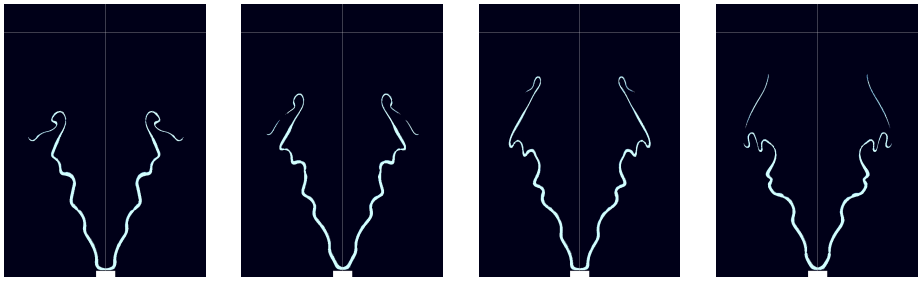
FIGURE A.5: Forcing of 150 Hz with adaptation 50 K/m.



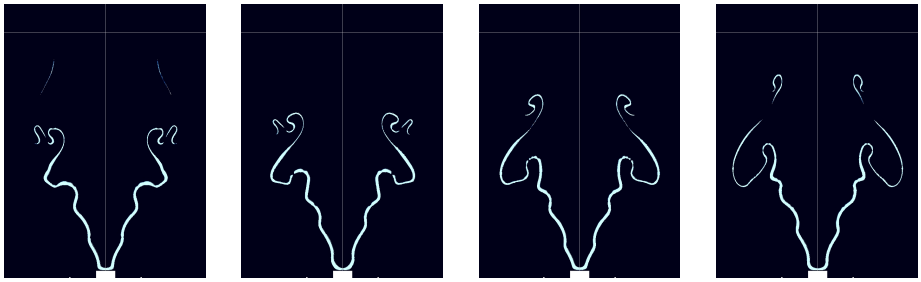
(A) 0 *ms* (B) 2.5 *ms* (C) 5 *ms* (D) 7.5 *ms*



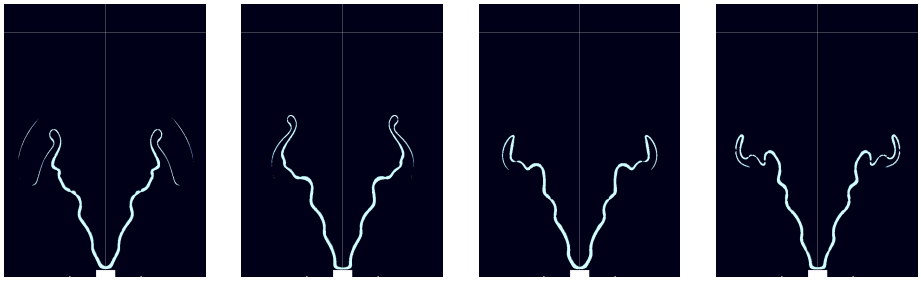
(E) 10 *ms* (F) 12.5 *ms* (G) 15 *ms* (H) 17.5 *ms*



(I) 20 *ms* (J) 22.5 *ms* (K) 25 *ms* (L) 27.5 *ms*

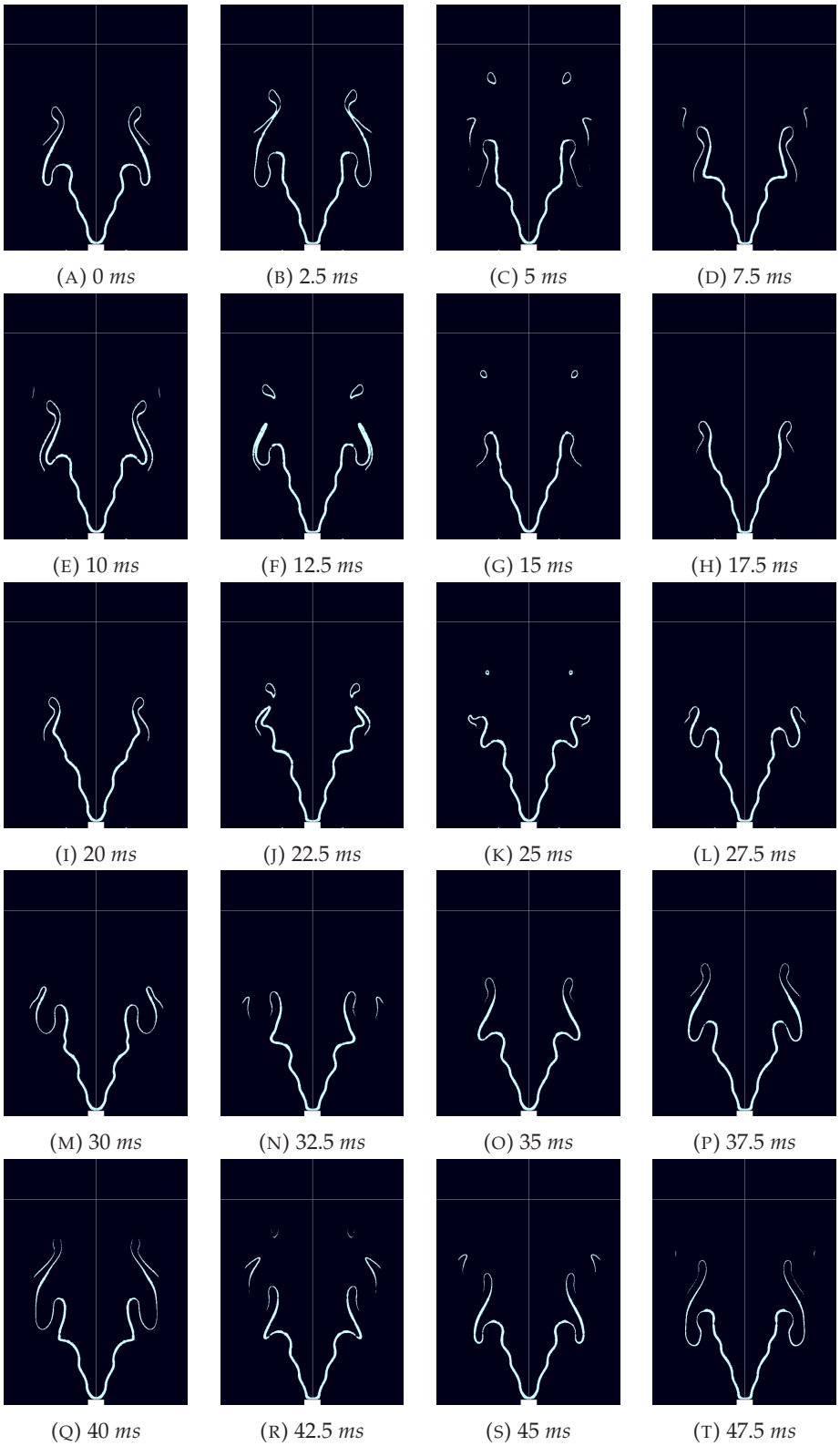


(M) 30 *ms* (N) 32.5 *ms* (O) 35 *ms* (P) 37.5 *ms*



(Q) 40 *ms* (R) 42.5 *ms* (S) 45 *ms* (T) 47.5 *ms*

FIGURE A.6: Forcing of 172 Hz with adaptation 50 K/m.



(A) 0 *ms* (B) 2.5 *ms* (C) 5 *ms* (D) 7.5 *ms*

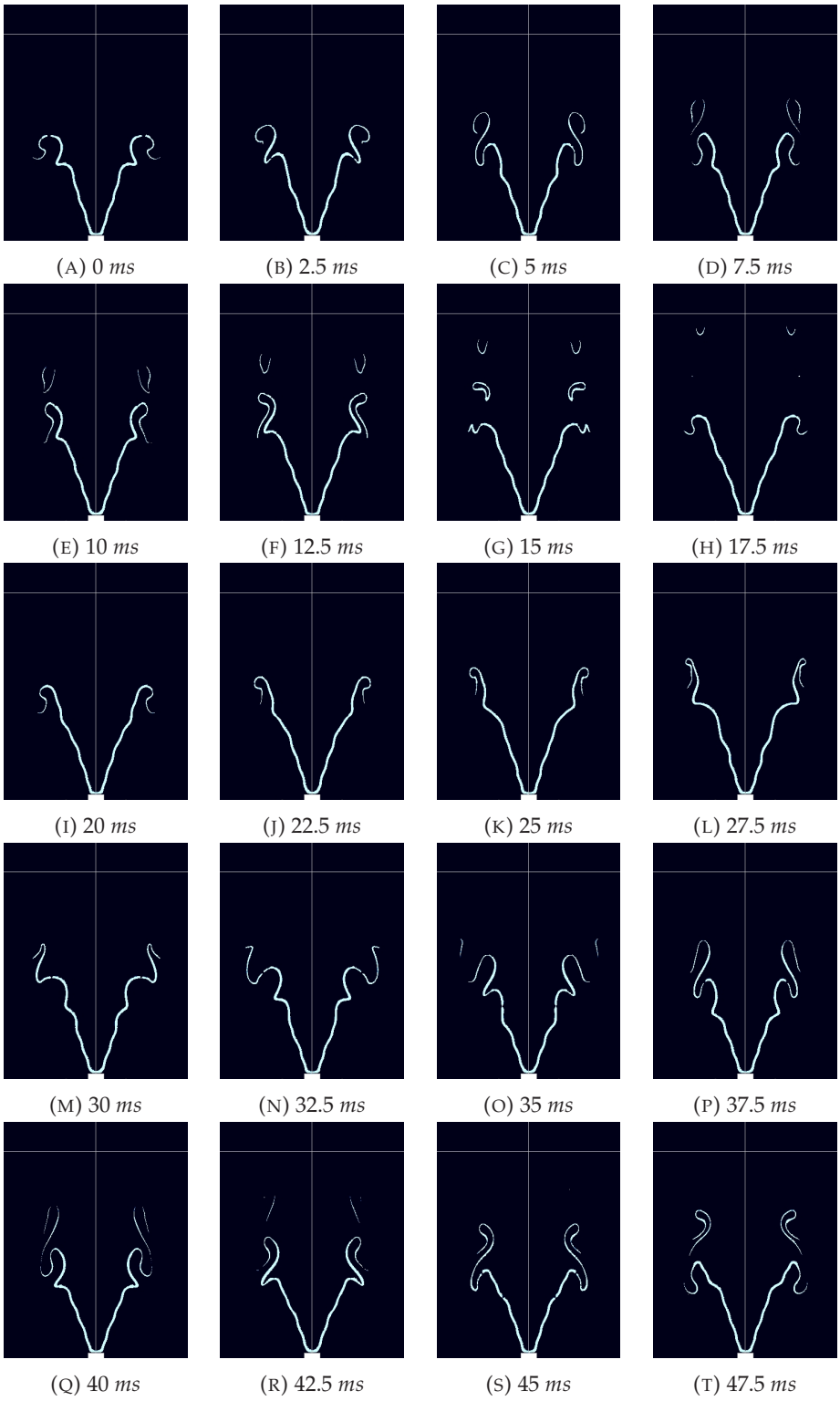
(E) 10 *ms* (F) 12.5 *ms* (G) 15 *ms* (H) 17.5 *ms*

(I) 20 *ms* (J) 22.5 *ms* (K) 25 *ms* (L) 27.5 *ms*

(M) 30 *ms* (N) 32.5 *ms* (O) 35 *ms* (P) 37.5 *ms*

(Q) 40 *ms* (R) 42.5 *ms* (S) 45 *ms* (T) 47.5 *ms*

FIGURE A.7: Forcing of 200 Hz with adaptation 50 K/m.



(A) 0 *ms* (B) 2.5 *ms* (C) 5 *ms* (D) 7.5 *ms*

(E) 10 *ms* (F) 12.5 *ms* (G) 15 *ms* (H) 17.5 *ms*

(I) 20 *ms* (J) 22.5 *ms* (K) 25 *ms* (L) 27.5 *ms*

(M) 30 *ms* (N) 32.5 *ms* (O) 35 *ms* (P) 37.5 *ms*

(Q) 40 *ms* (R) 42.5 *ms* (S) 45 *ms* (T) 47.5 *ms*

FIGURE A.8: Forcing of 250 Hz with adaptation 50 K/m.

Appendix B

FTF Gain and Phase for the Mesh Adaption Different Refinement Thresholds

Dans ce chapitre, une analyse de l'impact du seuil d'adaptation du maillage du gain FTF de l'ICF est présentée pour souligner la relation des seuils d'adaptation avec les divergences constatées sur le modèle CFD de l'ICF par rapport aux expériences.

In this Chapter, an analysis of the impact of the mesh adaption threshold of the FTF gain of the ICF is presented to underscore the relation of the adaption thresholds with the discrepancies found on the CFD model of the ICF with respect to the experiences.

To provide a CFD and experimental [9] comparison, the Root-Mean-Square (RMS) of the flame surface area fluctuations and the corresponding FTF gain are given on Figure B.1, which are computed as described in Section 2.3, as a function of the refinement threshold. This figure shows that both these quantities decrease simultaneously when the mesh adaption is tighter. Indeed, when the temperature gradient refinement threshold is either 50 or 100 K/m, $RMS(A') \approx 0.3\ m^2$ and the gain is close to 2.1. The gain has a value of around 1.5 for the thresholds of 10 and 25 K/m, and and the corresponding $RMS(A') \approx 0.15\ m^2$. The computed mean flame surface area, the RMS velocity and mean velocity have a constant dependency of the refinement gradient, and its corresponding values are 0.0132 m, 0.2 m/s and 2.31 m/s, respectively.

Concerning the phase, no remarkable difference has been observed between the thresholds choices, all results agree with experiments, with a value of $\approx 1.5\pi$. For the sake of brevity these are not shown here. Note that since the CFD model uses a second order upwind discretization, the mesh coarsening introduces some level of artificial dissipation, and thus smooths the solution, which in turn increases the gain. This smoothing is linked to the discontinuities of the flame front, identified with the α parameter, as discussed above. However, such smoothing does not interfere on the phase lag between the forcing and the flame surface fluctuation.

The experimental results [9], obtained for identical forcing, present a gain of 1.5, which is the same value obtained here for the refinement threshold of 10 K/m or 25 K/m. However, as already seen at Tab. 2.1, at least three months are necessary to model 1.5 s of the dynamics of the ICF using a refinement gradient of 10 K/m, which is around six times the time necessary to perform the same computation but using 50 K/m. As a consequence, a parametrical analysis of the frequency influence on the flame behavior could not be performed using the tighter refinement approach of 10 K/m. For this reason, a threshold value of 50 K/m is used in what follows for

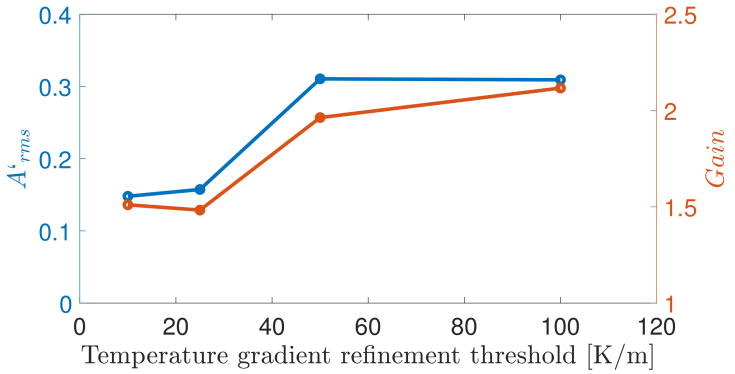


FIGURE B.1: RMS values of the flame surface area fluctuation $[m^2]$ and the corresponding FDF gain as a function of the temperature gradient refinement threshold.

the forced ICF. Although this result is an overestimation of the gain, the qualitative response of the flame can still be assessed.

Bibliography

[1] A. Demirbas, "Combustion systems for biomass fuel," *Energy Sources, Part A: Recovery, Utilization, and Environmental Effects*, vol. 29, no. 4, pp. 303–312, 2007. DOI: 10.1080/009083190948667.

[2] R. Mishra and S. Chandel, "Soot formation and its effect in an aero gas turbine combustor," *International Journal of Turbo and Jet-Engines*, vol. 36, 2016. DOI: 10.1515/tjj-2016-0062.

[3] T. Lieuwen and K. McManus, "Combustion dynamics in lean-premixed prevaporized (lpp) gas turbines," *Journal of Propulsion and Power*, vol. 19, no. 5, pp. 721–721, 2003. DOI: 10.2514/2.6171.

[4] D. Zhao and Z. Chow, "Thermoacoustic instability of a laminar premixed flame in rijke tube with a hydrodynamic region," *Journal of Sound and Vibration*, vol. 332, no. 14, pp. 3419–3437, 2013.

[5] G. Waxenegger-Wilfing, U. Sengupta, J. Martin, W. Armbruster, J. Hardi, M. Juniper, and M. Oschwald, "Early detection of thermoacoustic instabilities in a cryogenic rocket thrust chamber using combustion noise features and machine learning," *Chaos: An Interdisciplinary Journal of Nonlinear Science*, vol. 31, no. 6, p. 063 128, 2021. DOI: 10.1063/5.0038817.

[6] T. Pant, C. Han, and H. Wang, "Computational investigations of the coupling between transient flame dynamics and thermo-acoustic instability in a self-excited resonance combustor," *Combustion Theory and Modelling*, vol. 23, no. 5, pp. 854–884, 2019. DOI: 10.1080/13647830.2019.1599444.

[7] S. Ducruix, D. Durox, and S. Candel, "Theoretical and experimental determinations of the transfer function of a laminar premixed flame," *Proceedings of the Combustion Institute*, vol. 28, no. 1, pp. 765 –773, 2000, ISSN: 1540-7489. DOI: https://doi.org/10.1016/S0082-0784(00)80279-9.

[8] T. Schuller, S. Ducruix, D. Durox, and S. Candel, "Modeling tools for the prediction of premixed flame transfer functions," *Proceedings of the Combustion Institute*, vol. 29, pp. 107–113, 2002. DOI: 10.1016/S1540-7489(02)80018-9..

[9] D Durox, T Schuller, and S Candel, "Combustion dynamics of inverted conical flames," *Procedings of the Combustion Institute*, vol. 30, pp. 1717–1724, 2005. DOI: 10.1016/j.proci.2004.08.067.

[10] A. L. Birbaud, D Durox, S Ducruix, and S Candel, "Dynamics of confined premixed flames submited to upstream acoustic modulations," *Procedings of the Combustion Institute*, vol. 31, pp. 1257–1265, 2007. DOI: 10.1016/j.proci.2006.07.122.

[11] T. Steinbacher, A. Albayrak, A. Ghani, and W. Polifke, "Consequences of flame geometry for the acoustic response of premixed flames," *Combustion and Flame*, vol. 199, pp. 411 –428, 2019, ISSN: 0010-2180. DOI: https://doi.org/10.1016/j.combustflame.2018.10.039.

[12] D. Michaels and A. F. Ghoniem, "Leading edge dynamics of lean premixed flames stabilized on a bluff body," *Combustion and Flame*, vol. 191, pp. 39 –52, 2018, ISSN: 0010-2180. DOI: https://doi.org/10.1016/j.combustflame.2017.12.020.

[13] K. S. Kedia and A. F. Ghoniem, "The anchoring mechanism of a bluff-body stabilized laminar premixed flame," *Combustion and Flame*, vol. 161, no. 9, pp. 2327–2339, 2014, ISSN: 0010-2180. DOI: https://doi.org/10.1016/j.combustflame.2014.02.005.

[14] K. Prieur, D. Durox, T. Schuller, and S. Candel, "A hysteresis phenomenon leading to spinning or standing azimuthal instabilities in an annular combustor," *Combustion and Flame*, vol. 175, pp. 283–291, 2017, Special Issue in Honor of Norbert Peters, ISSN: 0010-2180. DOI: https://doi.org/10.1016/j.combustflame.2016.05.021.

[15] *Self-Sustained Instabilities in an Annular Combustor Coupled by Azimuthal and Longitudinal Acoustic Modes*, vol. Volume 1B: Combustion, Fuels and Emissions, Turbo Expo: Power for Land, Sea, and Air, Jun. 2013. DOI: 10.1115/GT2013-95010.

[16] "Forcing of self-excited round jet diffusion flames," *Proceedings of the Combustion Institute*, vol. 32, no. 1, pp. 1191–1198, 2009, ISSN: 1540-7489. DOI: https://doi.org/10.1016/j.proci.2008.05.065.

[17] A. Khan, M. Zihaib Khan, and S. Ansari, "Machine learning and soft computing techniques for combustion system diagnostics and monitoring: A survey," in. Feb. 2021, pp. 172–186, ISBN: 978-981-16-0418-8. DOI: 10.1007/978-981-16-0419-5_14.

[18] V. Michelassi, C. Allegorico, S. Cioncolini, A. Graziano, L. Tognarelli, and M. Sepe, "Machine learning in gas turbines," *Mechanical Engineering*, vol. 140, S54, Sep. 2018. DOI: 10.1115/1.2018-SEP5.

[19] W. Yan and L. Yu, "On accurate and reliable anomaly detection for gas turbine combustors: A deep learning approach," *arXiv preprint arXiv:1908.09238*, 2019.

[20] K. Wan, S. Hartl, L. Vervisch, P. Domingo, R. S. Barlow, and C. Hasse, "Combustion regime identification from machine learning trained by raman/rayleigh line measurements," *Combustion and Flame*, vol. 219, pp. 268–274, 2020, ISSN: 0010-2180. DOI: https://doi.org/10.1016/j.combustflame.2020.05.024.

[21] O. Choi, J. Choi, N. Kim, and M. Lee, "Combustion instability monitoring through deeplearningbased classification of sequential highspeed flame images," *Electronics*, vol. 9, p. 848, May 2020. DOI: 10.3390/electronics9050848.

[22] B. Cockburn, "Discontinuous galerkin methods," *ZAMM-Journal of Applied Mathematics and Mechanics/Zeitschrift für Angewandte Mathematik und Mechanik: Applied Mathematics and Mechanics*, vol. 83, no. 11, pp. 731–754, 2003.

[23] B. Cockburn, G. E. Karniadakis, and C.-W. Shu, *Discontinuous Galerkin methods: theory, computation and applications*. Springer Science and Business Media, 2012, vol. 11.

[24] N. Peters and M. Dekena, "Combustion modeling with the g-equation," *Oil and Gas Science and Technology-revue De L Institut Francais Du Petrole*, vol. 54, pp. 265–270, 1999.

[25] S. A. McQuarrie, C. Huang, and K. E. Willcox, "Data-driven reduced-order models via regularised operator inference for a single-injector combustion process," *Journal of the Royal Society of New Zealand*, vol. 51, no. 2, pp. 194–211, 2021. DOI: 10.1080/03036758.2020.1863237.

[26] U. Sengupta, M. Croci, and M. Juniper, "Real-time parameter inference in reduced-order flame models with heteroscedastic bayesian neural network ensembles," Oct. 2020.

[27] G. Aversano, M. Ferrarotti, and A. Parente, "Digital twin of a combustion furnace operating in flameless conditions: Reduced-order model development from cfd simulations," *Proceedings of the Combustion Institute*, vol. 38, no. 4, pp. 5373–5381, 2021, ISSN: 1540-7489. DOI: https://doi.org/10.1016/j.proci.2020.06.045.

[28] N. Anathkrishnan, S. Deo, and F. E. C. Culick, "Reduced-order modeling and dynamics of nonlinear acoustic waves in a combustion chamber," *Combustion Science and Technology*, vol. 177, no. 2, pp. 221–248, 2005. DOI: 10.1080/00102200590900219.

[29] N. Tathawadekar, N. A. K. Doan, C. F. Silva, and N. Thuerey, "Modeling of the nonlinear flame response of a bunsen-type flame via multi-layer perceptron," *Proceedings of the Combustion Institute*, vol. 38, no. 4, pp. 6261–6269, 2021, ISSN: 1540-7489. DOI: https://doi.org/10.1016/j.proci.2020.07.115.

[30] C. J. Lapeyre, A. Misdariis, N. Cazard, D. Veynante, and T. Poinsot, "Training convolutional neural networks to estimate turbulent sub-grid scale reaction rates," *Combustion and Flame*, vol. 203, pp. 255–264, 2019, ISSN: 0010-2180. DOI: https://doi.org/10.1016/j.combustflame.2019.02.019.

[31] R. Roncancio, J. Kim, A. El Gamal, and J. P. Gore, "Data-driven analysis of turbulent flame images," in *AIAA Scitech 2021 Forum*, 2021, p. 1787.

[32] N. Kazantzis and C. Kravaris, "Nonlinear observer design using lyapunov's auxiliary theorem," *Systems & Control Letters*, vol. 34, no. 5, pp. 241–247, 1998.

[33] A. Krener and M. Xiao, "Nonlinear observer design in the siegel domain," *SIAM J. Control and Optimization*, vol. 41, pp. 932–953, 2003. DOI: 10.1137/S0363012900375330.

[34] V. Andrieu and L. Praly, "On the existence of a kazantzis–kravaris/luenberger observer," *SIAM J. Control and Optimization*, vol. 45, pp. 432–456, 2006. DOI: 10.1137/040617066.

[35] P. Bernard, "Luenberger observers for nonlinear controlled systems," in *2017 IEEE 56th Annual Conference on Decision and Control (CDC)*, 2017, pp. 3676–3681. DOI: 10.1109/CDC.2017.8264200.

[36] L. da Costa Ramos, F. Di Meglio, L. F. Figueira Da Silva, and V. Morgenthaler, "Reduced order model of laminar premixed inverted conical flames," in *AIAA Scitech 2020 Forum*. 2020. DOI: 10.2514/6.2020-0416.

[37] ——, "Modeling of pulsating inverted conical flames: A numerical instability analysis," in *Combustion and Theory Modeling*. 2021.

[38] L. d. C. Ramos, F. Di Meglio, V. Morgenthaler, L. F. F. da Silva, and P. Bernard, "Numerical design of luenberger observers for nonlinear systems," in *2020 59th IEEE Conference on Decision and Control (CDC)*, 2020, pp. 5435–5442. DOI: 10.1109/CDC42340.2020.9304163.

[39] J Shinjo, Y Mizobuchi, and S Ogawa, "Numerical simulation of flame behavior in a lean premixed gas turbine combustor," in *Combustion and Noise Control*, G. D. Roy, Ed., Cranfield, UK: Cranfield University Press, 2003, p. 9.

[40] P. Gobbato, M. Masi, A. Lazzaretto, and A. Toffolo, "Analysis of the natural acoustic modes of a gas turbine combustor using isothermal cfd simulations," *Applied Thermal Engineering*, vol. 126, pp. 489–499, 2017, ISSN: 1359-4311. DOI: https://doi.org/10.1016/j.applthermaleng.2017.07.076.

[41] J. van Oijen, A. Donini, R. Bastiaans, J. ten Thije Boonkkamp, and L. de Goey, "State-of-the-art in premixed combustion modeling using flamelet generated manifolds," *Progress in Energy and Combustion Science*, vol. 57, pp. 30–74, 2016, ISSN: 0360-1285. DOI: https://doi.org/10.1016/j.pecs.2016.07.001.

[42] A. Coimbra and L. Silva, "Modelling of a turbulent lean premixed combustor using a reynolds-averaged navier–stokes approach," *Journal of the Brazilian Society of Mechanical Sciences and Engineering*, vol. 42, 2020. DOI: 10.1007/s40430-020-2273-y.

[43] N Noiray, D Durox, T Schuller, and S Candel, "A unified framework for nonlinear combustion instability analysis based on the flame describing function," *Journal of Fluid Mechanics*, vol. 615, pp. 139–167, 2008. DOI: 10.1017/S0022112008003613.

[44] V. D. Milosavljevic, "Pertubation in combustor near-field aerodynamics as a main source of thermoacoustic instabilities in modern industrial dry low no_x gas turbine combustion systems," in *Combustion and Noise Control*, G. D. Roy, Ed., Cranfield, UK: Cranfield University Press, 2003, pp. 55–60.

[45] S. McAllister, J.-Y. Chen, and A. C. Fernandez-Pello, "Fundamentals of combustion processes," in, 2nd ed. USA: Springer, 2011.

[46] "Reduced reaction sets based on gri-mech 1.2," in, A. Kazakov and M. Frenklach, Eds. Berkeley, USA: <http://combustion.berkeley.edu/drm/>, 1984.

[47] C. Celis and L. F. Figueira da Silva, "Computational assessment of methane-air reduced chemical kinetic mechanisms for soot production studies," *Journal of the Brazilian Society of Mechanical Sciences and Engineering*, vol. 38, no. 8, pp. 2225–2244, 2016, ISSN: 1806-3691. DOI: 10.1007/s40430-016-0494-x.

[48] F. P. I. Theodore L. Bergman Adrienne S. Lavine and D. P. Dewitt, "Fundamentals of heat and mass trasfer," in, 7th ed. USA: John Wiley and Sons, 2011.

[49] M. W. Chase, J. L. Curnutt, A. T. Hu, H. Prophet, A. N. Syverud, and L. C. Walker, "Janaf thermochemical tables, 1974 supplement," *Journal of Physical and Chemical Reference Data*, vol. 3, no. 2, pp. 311–480, 1974. DOI: 10.1063/1.3253143.

[50] I. ANSYS, *Chemkin-pro theory manual*, English, version Release 2020 R2, ANSYS, Inc., Published.

[51] ——, *Fluent user's guide*, English, version Release 2020 R2, ANSYS, Inc., Published.

[52] ——, *Fluent theory guide*, English, version Release 2020 R2, ANSYS, Inc., Published.

[53] D. E. Salane, "A stiff ode solver for use in solving two-dimensional reaction-diffusion problems," *Mathematical and Computer Modelling*, vol. 11, pp. 850–854, 1988, ISSN: 0895-7177. DOI: https://doi.org/10.1016/0895-7177(88)90613-9.

[54] S. Pope, "Computationally efficient implementation of combustion chemistry using in situ adaptive tabulation," *Combustion Theory and Modelling*, vol. 1, no. 1, pp. 41–63, 1997. DOI: 10.1080/713665229.

[55] A. Cunha Jr and L. F. Figueira da Silva, "Assessment of a transient homogeneous reactor through in situ adaptive tabulation," *Journal of the Brazilian Society of Mechanical Sciences and Engineering*, vol. 36, pp. 377–391, 2014. DOI: 10.1007/s40430-013-0080-4.

[56] C. Celis and L. F. F. da Silva, "Computational assessment of methane-air reduced chemical kinetic mechanisms for soot production studies," *Journal of the Brazilian Society of Mechanical Sciences and Engineering*, vol. 38, pp. 2225–2244, 2016.

[57] S. V. Patankar, *Numerical heat transfer and fluid flow*, ser. Series on Computational Methods in Mechanics and Thermal Science. Hemisphere Publishing Corporation (CRC Press, Taylor & Francis Group), 1980, ISBN: 978-0891165224.

[58] T. BARTH and D. JESPERSEN, "The design and application of upwind schemes on unstructured meshes," in *27th Aerospace Sciences Meeting*, 1989. DOI: 10.2514/6.1989-366.

[59] L. F. Figueira da Silva, J. L. Azevedo, and H. Korzenowski, "Unstructured adaptive grid flow simulations of inert and reactive gas mixtures," *Journal of Computational Physics*, vol. 160, pp. 522–540, 2000. DOI: 10.1006/jcph.2000.6470.

[60] Y. Huang and V. Yang, "Dynamics and stability of lean-premixed swirl-stabilized combustion," *Progress in Energy and Combustion Science*, vol. 35, no. 4, pp. 293–364, 2009, ISSN: 0360-1285. DOI: https://doi.org/10.1016/j.pecs.2009.01.002.

[61] L. Boyer and J. Quinard, "On the dynamics of anchored flames," *Combustion and Flame*, vol. 82, no. 1, pp. 51 –65, 1990, ISSN: 0010-2180. DOI: https://doi.org/10.1016/0010-2180(90)90077-5.

[62] A. P. Dowling, "A kinematic model of a ducted flame," *Journal of Fluid Mechanics*, vol. 394, 51–72, 1999. DOI: 10.1017/S0022112099005686.

[63] C. Li, M. Zhu, and J. P. Moeck, "An analytical study of the flame dynamics of a transversely forced asymmetric two-dimensional bunsen flame," *Combustion Theory and Modelling*, vol. 21, no. 5, pp. 976–995, 2017. DOI: 10.1080/13647830.2017.1327677.

[64] F. Baillot and F. Lespinasse, "Response of a laminar premixed v-flame to a high-frequency transverse acoustic field," *Combustion and Flame*, vol. 161, no. 5, pp. 1247 –1267, 2014, ISSN: 0010-2180. DOI: https://doi.org/10.1016/j.combustflame.2013.11.009.

[65] E. Luciano and J. Ballester, "Analysis of the dynamic response of premixed flames through chemiluminescence cross-correlation maps," *Combustion and Flame*, vol. 194, pp. 296 –308, 2018, ISSN: 0010-2180. DOI: https://doi.org/10.1016/j.combustflame.2018.05.005.

[66] S. Jaensch, M. Merk, T. Emmert, and W. Polifke, "Identification of flame transfer functions in the presence of intrinsic thermoacoustic feedback and noise," *Combustion Theory and Modelling*, vol. 22, pp. 1–22, 2018. DOI: 10.1080/13647830.2018.1443517.

[67] X. Han, J. Li, and A. S. Morgans, "Prediction of combustion instability limit cycle oscillations by combining flame describing function simulations with a thermoacoustic network model," *Combustion and Flame*, vol. 162, no. 10, pp. 3632 –3647, 2015, ISSN: 0010-2180. DOI: https://doi.org/10.1016/j.combustflame.2015.06.020.

[68] W. Polifke, "Modeling and analysis of premixed flame dynamics by means of distributed time delays," *Progress in Energy and Combustion Science*, vol. 79, p. 100 845, 2020, ISSN: 0360-1285. DOI: https://doi.org/10.1016/j.pecs.2020.100845.

[69] T Schuller, D Durox, and S Candel, "Self-induced combustion oscillations of laminar premixed flames stabilized on annular burners," *Combustion and Flame*, vol. 135, no. 4, pp. 525–537, 2003, ISSN: 0010-2180. DOI: https://doi.org/10.1016/j.combustflame.2003.08.007.

[70] N. Noiray, D. Durox, T. Schuller, and S. Candel, "Self-induced instabilities of premixed flames in a multiple injection configuration," *Combustion and Flame*, vol. 145, no. 3, pp. 435–446, 2006, ISSN: 0010-2180. DOI: https://doi.org/10.1016/j.combustflame.2006.01.006.

[71] T. C. Lieuwen, *Unsteady Combustor Physics*. Cambridge University Press, 2012. DOI: 10.1017/CBO9781139059961.

[72] S. Ducruix, T. Schuller, D. Durox, and S. Candel, "Combustion dynamics and instabilities: Elementary coupling and driving mechanisms," *Journal of Propulsion and Power*, vol. 19, no. 5, pp. 722–734, 2003. DOI: 10.2514/2.6182.

[73] M. Fleifil, A. Annaswamy, Z. Ghoneim, and A. Ghoniem, "Response of a laminar premixed flame to flow oscillations: A kinematic model and thermoacoustic instability results," *Combustion and Flame*, vol. 106, no. 4, pp. 487–510, 1996, ISSN: 0010-2180. DOI: https://doi.org/10.1016/0010-2180(96)00049-1.

[74] J. O. Keller and K. Saito, "Measu rements of the combusting flow in a pulse combustor," *Combustion Science and Technology*, vol. 53, no. 2-3, pp. 137–163, 1987. DOI: 10.1080/00102208708947024.

[75] B. Lewis and G. Von Elbe, *Combustion, Flames, and Explosions of Gases*. Academic Press, 1987, ISBN: 9780124467514.

[76] T. Poinsot and D. Veynante, *Theoretical and Numerical Combustion*. Edwards, 2005, ISBN: 9781930217102.

[77] H. Schlichting and K. Gersten, *Boundary-Layer Theory*. 2017, ISBN: 978-3-662-52917-1. DOI: 10.1007/978-3-662-52919-5.

[78] A. Er-raiy, Z. Bouali, J. Réveillon, and A. Mura, "Optimized single-step (oss) chemistry models for the simulation of turbulent premixed flame propagation," *Combustion and Flame*, vol. 192, pp. 130–148, 2018, ISSN: 0010-2180. DOI: https://doi.org/10.1016/j.combustflame.2018.01.038.

[79] S. L. Brunton, B. R. Noack, and P. Koumoutsakos, "Machine learning for fluid mechanics," *Annual Review of Fluid Mechanics*, vol. 52, pp. 477–508, 2020.

[80] Y. LeCun, Y. Bengio, and G. Hinton, "Deep learning," *Nature*, vol. 521, pp. 436–44, 2015. DOI: 10.1038/nature14539.

[81] V. Luboz, M. Bailet, C. Boichon Grivot, M. Rochette, B. Diot, M. Bucki, and Y. Payan, "Personalized modeling for real-time pressure ulcer prevention in sitting posture," *Journal of Tissue Viability*, vol. 27, pp. 1571–1583, 2007. DOI: 10.1002/fld.1365.

[82] Z Boussaada, O Curea, R Ahmed, H Camblong, and N Mrabet-Bellaaj, "A nonlinear autoregressive exogenous (narx) neural network model for the prediction of the daily direct solar radiation," *Energies*, vol. 11, p. 620, 2018. DOI: 10.3390/en11030620.

[83] S Asgari, X Hu, M Tsuk, and S Kaushik, "Application of pod plus lti rom to battery thermal modeling: Siso case," *SAE International Journal of Commercial Vehicles*, vol. 7, pp. 278–285, 2014. DOI: 10.4271/2014-01-1843.

[84] E. Acar, "Various approaches for constructing an ensemble of metamodels using local measures," *Structural and Multidisciplinary Optimization*, vol. 42, no. 6, pp. 879–896, 2010. DOI: 10.1007/s00158-010-0520-z.

[85] F. A. C. Viana, R. T. Haftka, and V. Steffen, "Multiple surrogates: How cross-validation errors can help us to obtain the best predictor," *Structural and Multidisciplinary Optimization*, vol. 39, no. 4, pp. 439–457, 2009. DOI: 10.1007/s00158-008-0338-0.

[86] M. B. Salem and L. Tomaso, "Automatic selection for general surrogate models," *Structural and Multidisciplinary Optimization*, vol. 58, pp. 719–734, 2018. DOI: 10.1007/s00158-018-1925-3.

[87] M. Ben Salem, O. Roustant, F. Gamboa, and L. Tomaso, "Universal prediction distribution for surrogate models," *SIAM/ASA Journal on Uncertainty Quantification*, vol. 5, no. 1, pp. 1086–1109, 2017.

[88] W. Polifke, "Black-box system identification for reduced order model construction," *Annals of Nuclear Energy*, vol. 67, pp. 109–128, 2014, Advanced stability analysis for nuclear reactors, ISSN: 0306-4549. DOI: https://doi.org/10.1016/j.anucene.2013.10.037.

[89] A. H. Jazwinski, *Stochastic processes and filtering theory*. Courier Corporation, 2007.

[90] J Gauthier and G Bornard, "Observability for any u (t) of a class of nonlinear systems," *IEEE Transactions on Automatic Control*, vol. 26, no. 4, pp. 922–926, 1981.

[91] P. Bernard, *Observer design for nonlinear systems*. Springer, 2019, vol. 479.

[92] D. Luenberger, "Observers for multivariable systems," *IEEE Transactions on Automatic Control*, vol. 11, no. 2, pp. 190–197, 1966.

[93] A. Shoshitaishvili, "On control branching systems with degenerate linearization," *Proc. IFAC Symp. Nonlinear Control Syst.*, pp. 495–500, 1992.

[94] P. Bernard and V. Andrieu, "Luenberger observers for nonautonomous nonlinear Systems," *IEEE Transactions on Automatic Control*, vol. 64, no. 1, pp. 270–281, 2019. DOI: 10.1109/TAC.2018.2872202.

[95] M. I. Quraishi, J. P. Choudhury, and M. De, "Image recognition and processing using artificial neural network," in *2012 1st International Conference on Recent Advances in Information Technology (RAIT)*, IEEE, 2012, pp. 95–100.

[96] J. Fu, H. Zheng, and T. Mei, "Look closer to see better: Recurrent attention convolutional neural network for fine-grained image recognition," in *Proceedings of the IEEE conference on computer vision and pattern recognition*, 2017, pp. 4438–4446.

[97] A. Krizhevsky, I. Sutskever, and G. E. Hinton, "Imagenet classification with deep convolutional neural networks," *Commun. ACM*, vol. 60, no. 6, 84–90, 2017, ISSN: 0001-0782. DOI: 10.1145/3065386.

[98] Y. Goldberg, "A primer on neural network models for natural language processing," *J. Artif. Int. Res.*, vol. 57, no. 1, 345–420, 2016, ISSN: 1076-9757.

[99] D. H. Nguyen and B. Widrow, "Neural networks for self-learning control systems," *IEEE Control Systems Magazine*, vol. 10, no. 3, pp. 18–23, 1990.

[100] E. Diaconescu, "The use of narx neural networks to predict chaotic time series," *WSEAS Transactions on Computer Research*, vol. 3, 2008.

[101] S. Pan and K. Duraisamy, "Long-time predictive modeling of nonlinear dynamical systems using neural networks," *Complexity*, vol. 2018, 2018.

[102] M. A. Nielsen, *Neural networks and deep learning*, misc, 2018.

[103] Hecht-Nielsen, "Theory of the backpropagation neural network," in *International 1989 Joint Conference on Neural Networks*, 1989, 593–605 vol.1.

[104] N. Henwood, "Estimation en ligne de paramètres de machines électriques pour véhicule en vue d'un suivi de la température de ses composants," Ph.D. dissertation, MINES ParisTech, PSL University, 2014.

[105] T. Kanamaru, "Van der Pol oscillator," *Scholarpedia*, vol. 2, no. 1, p. 2202, 2007, revision #138698. DOI: 10.4249/scholarpedia.2202.

[106] S. Jaensch and W. Polifke, "Uncertainty encountered when modelling self-excited thermoacoustic oscillations with artificial neural networks," *International Journal of Spray and Combustion Dynamics*, vol. 9, no. 4, pp. 367–379, 2017. DOI: 10.1177/1756827716687583.

[107] L. Ljung, *System Identification: Theory for the User*, ser. Prentice Hall information and system sciences series. Prentice Hall PTR, 1999, ISBN: 9780136566953.

[108] H. T. Siegelmann, B. G. Horne, and C. L. Giles, "Computational capabilities of recurrent narx neural networks," *IEEE Transactions on Systems, Man, and Cybernetics, Part B (Cybernetics)*, vol. 27, no. 2, pp. 208–215, 1997.

[109] I. ANSYS, *Twin builder help*, English, version Release 2021 R2, ANSYS, Inc., 2021, Published.

[110] L. Crocco, "Theoretical studies on liquid-propellant rocket instability," *Symposium (International) on Combustion*, vol. 10, no. 1, pp. 1101–1128, 1965, Tenth Symposium (International) on Combustion, ISSN: 0082-0784. DOI: https://doi.org/10.1016/S0082-0784(65)80249-1.

[111] M. Buisson-Fenet, F. Solowjow, and S. Trimpe, *Actively learning gaussian process dynamics*, 2019. arXiv: 1911.09946 [cs.LG].

[112] E. Walter and L. Pronzato, "Identification of parametric models," *Communications and control engineering*, vol. 8, 1997.

RÉSUMÉ

La combustion est un processus réactif présent dans presque tous les secteurs sociaux, étant responsable de plus de 80% de la conversion primaire de l'énergie. Par exemple, dans les moteurs d'avion, le couplage entre la combustion et l'acoustique peut conduire à des instabilités thermo-acoustiques qui peuvent endommager les moteurs, conduisant à l'échec. Ce travail se concentre sur la modélisation, caractérisation et contrôle des instabilités de combustion, à travers des approches computationnelles. Plus précisément, des modèles réactifs de dynamique des fluides numériques, des modèles d'ordre réduit et la conception d'observateurs d'état sont utilisés. Les processus de combustion instables étudiés présentent un riche spectre de fréquences, et le gain et la phase correspondants sont comparés favorablement aux expériences. Un observateur a été conçu en utilisant des techniques de réseaux neuronaux artificiels, et son application à des systèmes non linéaires a mis en évidence la faible erreur d'estimation des états des systèmes.

MOTS CLÉS

Combustion, acoustique, instabilités, CFD, machine learning, observateurs d'état

ABSTRACT

Combustion is a chemical reaction process present in almost all social sectors, being responsible for more than 80% of the energy primary conversion. For instance, in aircraft engines, the combustion and acoustic coupling may lead to thermoacoustic instabilities that could damage the engines, causing failures. This work focuses on the modelling, characterization and control of combustion instabilities, through computational approaches. More precisely, reactive computational fluid dynamic models, reduced order models and state observer design are used. The unstable combustion processes studied were shown to exhibit a rich frequency spectrum, and the corresponding gain and phase were favourably compared to experiments. An observer was designed using artificial neural network techniques, and its application to non linear systems evidenced the low error estimation of systems states.

KEYWORDS

Combustion, acoustic, instabilities, CFD, machine learning, state observers